

Determination of Hotspot Location and Power Cable Temperatures from Spare Duct
Temperatures in an Underground Installation

by

Aman Sharma

A Thesis Presented in Partial Fulfillment
of the Requirements for the Degree
Master of Science

Approved November 2017 by the
Graduate Supervisory Committee:

Daniel J. Tylavsky, Chair

Keith Holbert

Jinagchao Qin

ARIZONA STATE UNIVERSITY

December 2017

ABSTRACT

In this work a comparison has been made between the predictions from the models using both the present theory for the underground cable temperature prediction and the CYMCAP application and the field measurements to determine which, if any, models are capable of predicting the temperature and hotspot locations in an installation where the power cable is not embedded with the optical fibers and, therefore, where the cable temperatures must be inferred from the temperature measurements made in nearby spare ducts. The temperature measurements were collected from the underground 69 kV cable at the Brandow-Pickrell installation, which is a part of Salt River Project's power sub-transmission system. The model development and the results are explained in detail. Results from the model developed have been compared and the factors affecting the cable temperature are highlighted.

Once the models were developed, it was observed that the earth surface temperature above the installation, solar radiation and other external factors such as underlying water lines, drain pipes, etc. play a key role in heating up or cooling down the power cables. It was also determined that the hotspot location in the power cable in the main duct was the same as the hotspot location in the spare duct inside the same installation.

It was also observed that the CYMCAP model had its limitations when the earth surface temperature variations were modeled in the software as the software only allows the earth's ambient temperature to be modeled as a constant; further, results from the MATLAB model were more in line with the present theory of underground power cable temperature

prediction. However, simulation results from both the MATLAB and CYMCAP model showed deviation from the measured data. It was also observed that the spare duct temperatures in this particular underground installation seemed to be affected by external factors such as solar radiation, underlying water lines, gas lines etc. which cannot be modeled in CYMCAP.

ACKNOWLEDGMENTS

I would like to first and foremost thank my advisor, Dr. Daniel J. Tylavsky, for his encouragement, guidance, and support on this research work. I appreciate that Salt River Project has given me an opportunity to conduct a research on their 69 kV underground systems. During the project, Jim Hunt, Bryce Priest and Travis Stowers at Salt River Project shared their useful experience with me. I really appreciate their guidance and support. I also would like to express my gratitude to Dr. Jiangchao Qin and Dr. Keith Holbert for their time and consideration in being members of my supervisory committee.

TABLE OF CONTENTS

	Page
LIST OF TABLES.....	viii
LIST OF FIGURES	ix
NOMENCLATURE	xv
CHAPTER	
1 INTRODUCTION	1
1.1 Background.....	1
1.2 Motivation.....	2
1.3 Research Goal and Project Scope	3
2 LITERATURE REVIEW	4
2.1 Underground Cable Components	4
2.1.1 Conductor	4
2.1.2 Semiconductor Screen on Conductor	5
2.1.3 XLPE Insulation	5
2.1.4 Insulation Screen	5
2.1.5 Metallic Screen	5
2.1.6 Sheath	6
2.2 Underground Cable Installations	7

CHAPTER	Page
2.3 Distributed Temperature Sensing System	8
2.3.1 Principle and Working of DTS Systems.....	9
2.3.2 Single Ended and Double Ended Measurement	10
2.3.3 Optical Fibers.....	12
2.4 Basic Principle for Temperature Prediction	12
2.5 Power Cable Ladder Model	15
2.5.1 Calculation of Thermal Resistances and Capacitances.....	16
2.6 Soil Ladder Model	18
3 BRANDOW PICKRELL EXISTING INTALLATION	21
3.1 Overview.....	21
3.2 Duct bank Configurations.....	22
3.3 DTS INSTALLATION.....	25
3.3.1 Fiber-Optic Cable Installation and Splicing	26
4 DTS COMMISSIONING AND PRELIMINARY RESULTS.....	28
4.1 Fiber Scheme	28
4.2 Charon3 Software	29
4.3 Measurement Phase Selection	32
4.4 Preliminary Results.....	33

CHAPTER	Page
5 HOTSPOT LOCATION	41
5.1 Hotspot Detection and Seasonal Shift in Hotspot Location	41
6 MODELS FOR TEMPERATURE PREDICTION	49
6.1 The CYMCAP Model.....	50
6.1.1 Constant Earth’s Surface Temperature (CEST) Model for CYMCAP	51
6.1.2 Observations	55
6.1.3 Time Varying Earth’s Surface Temperature (TVEST) Model for CYMCAP.....	57
6.1.4 Modeling Earth Surface Temperature in CYMCAP.....	58
6.1.5 Simulation and Results	62
6.2 MATLAB model	67
6.2.1 Development of Ladder Network for the Cable	67
6.2.2 Soil Thermal Model.....	71
6.2.3 CEST Model for MATLAB and its Validation	73
6.2.4 TVEST Model for MATLAB.....	76
6.3 Results.....	79
6.3.1 Simulation Results for Case A.....	84
6.3.2 Simulation Results for Case B.....	88

CHAPTER	Page
7 CONCLUSION AND FUTURE WORK	98
7.1 Hotspot Location	98
7.2 Earth's Ambient and Surface Temperatures	100
7.3 Spare Duct Temperatures	101
7.4 Future Work.....	102
REFERENCES.....	104

LIST OF TABLES

Table	Page
4-1 Power Cable Fiber Length Measurement from Pt. A and Pt. B	36
4-2 Fiber Length Measurement in the Spare Duct from Pt. A to Pt. B.....	36
5-1 Monthly Hotspot Temperatures in Different Fibers in the Installation	48
6-1 Comparison Between TVEST Model Simulation Results and Measured Data	65
6-2 Cable Data for Ladder Network.	68
6-3 Values of Thermal Resistances and Capacitances for the Soil Model for Case A.....	72
6-4 Values of Thermal Resistances and Capacitances for the Soil Model for Case B	72
6-5 Legend for the MATLAB Simulation Models	74
6-6 Comparison of CEST Model Results in MATLAB and the Measured Data	75
6-7 Comparison of Temperatures of Power Cable for Measured and Simulated Data	93
6-8 Comparison of the Spare Duct Temperatures for Measured and Simulated Data.....	94
6-9 Comparison of the Phase Shifts of the Power Cable and Spare Duct for the Measured and Simulated Data	94

LIST OF FIGURES

Figure	Page
2-1 Cable Lateral and Cross Section.....	4
2-2 Diagram of the Cable Wound with the Fiber Optic.....	6
2-3 Underground Cables in Vertical Arrangement.....	8
2-4 Underground Cables in Horizontal Arrangement.....	8
2-5 Working of Distributed Temperature Sensing System.....	10
2-6 Cross-Section of the Buried Cable and Isothermal Surfaces from Heat Flow	13
2-7 Ladder Circuit for a Cable Showing Each Layer as RC Circuit.....	17
2-8 Soil Ladder Model for a Buried Cable	19
3-1 Overhead View of Brandow-Pickrell Underground Installation.....	21
3-2 Splice Box on Riser Pole P30.....	22
3-3 Sections with Different Duct Bank Configurations.....	23
3-4 Vertical Duct Bank Arrangement for Manhole and Riser Section.....	24
3-5 Vertical Duct Bank Arrangement for Installation	24
3-6 Horizontal Duct Bank Arrangement for Installation	24
3-7 Reinforced Trench Section of the Installation	25
3-8 Fiber Length Marking.....	26
4-1 Schematic Diagram for the Brandow-Pickrell Fiber Optic Arrangement	28

Figure	Page
4-2 Quick Start Application Showing the Scanned Lengths of the Fibers	30
4-3 Loop Configuration Setting of the DTS	31
4-4 Measurement Parameter Setting for the DTS.....	31
4-5 Backscatter Plot for the Fiber in the Power Cable in the Main Duct	32
4-6 Section Layout with the Length Markings Along the Installation	34
4-7 Measured Temperature Plot for the Fiber in the Main Duct from Pt. A to Pt. B	37
4-8 Measured Temperature Plot for the Fibers in the Spare Duct. Red Curve is for the Dual-Ended Measurement and Black Curve is for the Single-Ended Measurement.....	37
4-9 Hotspot Location for Power Cable Fiber and Spare Duct Fiber on February 03, 2017	39
4-10 Temperature Variation for Fibers in Main and Spare duct on February 03, 2017 ...	40
5-1 Hotspot Location on the Fiber in the Power Cable in the Main Duct (Fiber 1) and the Fiber in the Spare Duct (Fiber 3) in January 2017.....	42
5-2 Hotspot Location on the Fiber in the Power Cable in the Main Duct (Fiber 1) and the Fiber in the Spare Duct (Fiber 3) in February 2017.....	43
5-3 Hotspot Location on the Fiber in the Power Cable in the Main Duct (Fiber 1) and the Fiber in the Spare Duct (Fiber 3) in March 2017.....	43
5-4 Hotspot Location on the Fiber in the Power Cable in the Main Duct (Fiber 1) and the Fiber in the Spare Duct (Fiber 3) in April 2017.....	44

Figure	Page
5-5 Hotspot Location on the Fiber in the Power Cable in the Main Duct (Fiber 1) and the Fiber in the Spare Duct (Fiber 3) in May 2017.....	44
5-6 Hotspot Location on the Fiber in the Power Cable in the Main Duct (Fiber 1) and the Fiber in the Spare Duct (Fiber 3) in June 2017.....	45
5-7 Hotspot Location on the Fiber in the Power Cable in the Main Duct (Fiber 1) and the Fiber in the Spare Duct (Fiber 3) in July 2017	45
5-8 Hotspot Locations on Sectional Layout of the Brandow-Pickrell Installation.....	46
6-1 CYMCAP Models for the Horizontal, Vertical and Reinforced Section Configuration	51
6-2 Simplified Configurations for the Horizontal, Vertical and Reinforced Sections of the Duct Bank	52
6-3 Modified CYMCAP Model for the Duct Bank Configurations	53
6-4 Power Cable Load as Modeled in CYMCAP.....	54
6-5 Simulation Results for the CYMCAP CEST Model	56
6-6 Measured Data for a Seven-day Period from February 08 - 14, 2017.....	57
6-7 CYMCAP Model with the Heat Source	58
6-8 Setup for the Earth's Ambient Temperature and Native Soil Resistivity	59
6-9 Heat Source Modeling Parameters in CYMCAP	60

Figure	Page
6-10 Temperature Samples for Various times During the Day at the Hotspot Location on March 10, 2017	61
6-11 Temperature Plot for the Earth’s Surface Temperature at the Hotspot Location on March 10, 2017	61
6-12 Current Magnitude in the Power Cable in the Main Duct from March 08-14, 2017	62
6-13 Simulation Results for the Temperatures in the Power Cable and Spare Cable with the Earth’s Surface Temperature Modeled as a Heat Source	63
6-14 Measured Temperature for the Main Power Cable and Spare Duct from March 08- 14, 2017.....	64
6-15 CYMCAP Model with the Spare Cable at a Distance of 1 Foot from the Earth’s Surface Modeled as a Heat Source.	66
6-16 Reduced Two-Loop Ladder Circuit for Power Cable	68
6-17 MATLAB Simulink Ladder Model for the Power Cable in the Underground Installation.....	73
6-18 Simulation Results for the CEST Model in MATLAB Simulink	75
6-19 Heat Dissipation Through Conduction into the Earth	76
6-20 MATLAB Simulink TVEST Model for Case A	78
6-21 MATLAB Simulink TVEST Model for Case B.....	79
6-22 Measured Earth's Surface Temperature Data Plots for March 08, 2017	80

Figure	Page
6-23 Measured Earth's Surface Temperature Data Plots for March 10, 2017	81
6-24 Measured Earth's Surface Temperature Data for June 04, 2017	81
6-25 Measured Earth's Surface Temperature Data for June 20, 2017	82
6-26 Conductor Load Current on March 10, 2017	82
6-27 Conductor Load Current on March 10, 2017	83
6-28 Conductor Load Current on June 04, 2017.....	83
6-29 Conductor Load Current on June 20, 2017.....	84
6-30 Simulation Results for the MATLAB Model for Case A for March 08, 2017.....	85
6-31 Simulation Results for the MATLAB Model for Case A for March 10, 2017.....	85
6-32 Simulation Results for the MATLAB Model for Case A for June 04, 2017.....	86
6-33 Simulation Results for the MATLAB Model for Case A for June 20, 2017.....	86
6-34 Plots for Measured Temperature in the Power Cable and the Spare Duct for March 08, March 10, 2017	87
6-35 Plots for Measured Temperature in the Power Cable and the Spare Duct for June 04 and June 20, 2017	88
6-36 Simulation Results for MATLAB Model for Case B for March 08 and March 10, 2017.....	89
6-37 Simulation Results for MATLAB Model for Case B for June 04 and June 20, 2017	90

Figure	Page
6-38 Plots for Measured Temperature in the Power Cable and the Spare Duct for March 08 and March 10, 2017	91
6-39 Plots for Measured Temperature in the Power Cable and the Spare Duct for June 04 and June 20, 2017	92
7-1 Plot for Hotspot Location in the Power Cable for the Months of Feb - June 2017	99

NOMENCLATURE

C_1	Thermal capacitance of conductor
C_2	Thermal capacitance of insulation
C_3	Thermal capacitance of sheath
C_4	Thermal capacitance of jacket and external covering
D_1	Internal diameter
D_2	External diameter
D	Conductor diameter
I	Load in the conductor
K	Boltzmann Constant
L	Length of lay
L_f	Length of fiber for one complete wound
L	Length of the conductor
N	Total number of layers
Q_A	Combined thermal capacitance in a reduced two loop RC circuit
Q_B	Combined thermal capacitance of armor and sheath in a reduced two loop RC circuit

T	Temperature
T_A	Thermal resistance of conductor in reduced two loop RC circuit
T_B	Combined thermal resistance of insulation and armor in reduced two loop RC circuit
T_{amb}	Earth's ambient temperature
T_1	Thermal resistance of conductor
T_2	Thermal resistance of insulation
T_3	Thermal resistance of armor and sheath
T_4	Soil thermal resistance
W_c	I ² R losses in conductor per unit length
W_s	Dielectric losses per unit length
Z	Distance along the cable
b_i	Layer boundary
c	Volumetric specific heat capacity
c_{cu}	Volumetric specific heat capacity of copper
c_i	Volumetric specific heat capacity of insulation
c_{soil}	Volumetric specific heat capacity of soil

d	Distance from conductor
d'	Distance from image of conductor
d_m	Model depth
h	Depth of conductor below earth's surface
i	Layer number
k	Distance of point on isothermal surface from conductor
p	Van Worner's coefficient
th	Thickness of soil layer
r_c	Radius of conductor
r_{ext}	External radius
r_i	Radius of jacket
r_{int}	Internal radius
r_s	Radius of sheath
r_j	Radius of jacket
$\Delta\alpha$	Differential attenuation
Γ	Distribution of quantum states

\hbar	Planck's Constant
Ω	Angular Frequency
ρ	Thermal resistivity
ρ_{soil}	Thermal resistivity of soil
Γ	Exponential distribution factor
λ_l	Insulation loss factor

1 INTRODUCTION

1.1 Background

There are two types of transmission lines used for the electrical energy transmission: underground cables and overhead lines. Both have their own advantages and disadvantages. However, whenever we consider aesthetic designs and protection of transmission lines from the critical weather conditions, the underground cables are always preferred over the overhead transmission lines.

In addition to these benefits, the underground cables can carry emergency power loads as they are typically loaded below their rated loads, reduce fault probability, they are less susceptible to the impact of weather and are desirable for areas with dense population and areas which are subject to future development.

The main disadvantages of the underground cables are the difficulty of locating faults, the cost of repairs and the installation cost. Many faults in the underground lines occur due to the damage in the insulation of the power cables due to overheating. Therefore, the power cables are rated with their current carrying capacity, or ampacity. The current carrying capacity of the underground cables is limited by its thermal rating since high currents over a long interval of time can cause faults in the underground installed cable due to overheating and damaging the cable dielectric insulation.

The current carrying capacity, or the ampacity of a cable refers to the maximum current a conductor can carry before it damages the cable insulation. It is also considered as the

steady-state current rating of the cable. The ampacity of the cable depends on its insulation type, electrical resistance, current frequency, cable orientation, burial depth, cable's ability to dissipate heat and the ambient temperature of the soil surrounding the cable.

1.2 Motivation

The underground cables are often de-rated and are operated below their steady-state ratings. The cables are under-utilized most of the time because of the de-rating. This is due to the fact, that the underground cables get hotter at certain locations than at others, and the hotspot (whose location may change with season) is typically used to determine the conductor ampacity. These hotspots are caused by ineffective heat dissipation from the cable in that location. These are the locations we need to identify and the factors affecting the hotspot location need to be highlighted.

The hotspot location depends on a range of factors such as soil thermal conductivity, electric power lines crossing from other circuits, depth of the conductor and closeness to the riser poles and other such structures. To identify the hotspot location, cable temperature measurements along the entire installation are necessary. The cable temperature measurements are made using the fiber-optic cable embedded in the cable jacket. However, there are some installations where this fiber-optic cable is not present, which makes measuring the temperatures difficult. This project focuses on developing models to predict the temperature and the hotspot location on the power cable based on the spare duct temperature measurements.

1.3 Research Goal and Project Scope

The Salt River Project (SRP) power and water utility company currently operates sixteen 69 kV underground transmission lines. Not all the lines have fiber optics embedded in the cable, a fiber which can be used to detect the temperature along the length of the cable using the Distributed Temperature Sensing (DTS) controller. This project focuses on measuring the temperature in the spare duct using a fiber-optic cable installed for that purpose and then predicting the hotspot location on the power cable in an adjacent duct, based on the spare-duct temperature measurements. This project also studies whether a power cable temperature prediction model can be developed based on the spare duct temperature measurements. This is done by installing the fiber-optic cables in a spare duct and using the DTS controller to record the real-time temperature measurements from the spare duct. Real time temperature measurements of the power cable in the same installation are also recorded since the cable in the main duct has an embedded fiber optic which is connected to the DTS controller. This data will then be used to validate both a CYMCAP and MATLAB-based models for predicting the temperature of the cable as a function of the ambient temperature and the current in the cable. The validated models will help in predicting the temperature and the hotspot location of the underground power cables at the locations where SRP does not have existing conductors with the embedded fiber-optic cables. More accurate cable ratings have the potential to offer improved system reliability since faults due to the overheating of the cable can be prevented and by fully utilizing the potential of the installed underground systems, the effective capacity of the system is expanded.

2 LITERATURE REVIEW

2.1 Underground cable components

Since the underground cables are buried, there is a need to insulate the conductor from ground. While the insulation is needed to protect the cable from line-to-ground faults, the insulating material should not resist the heat dissipation from the conductor as it might damage the cable insulation itself. Underground cables are made of either aluminum or copper conductor core, semiconductor screen insulation, XLPE insulation layer, insulation screen, metallic screen, binder and sheath. Figure 2-1 shows the lateral section and cross section of the cable.

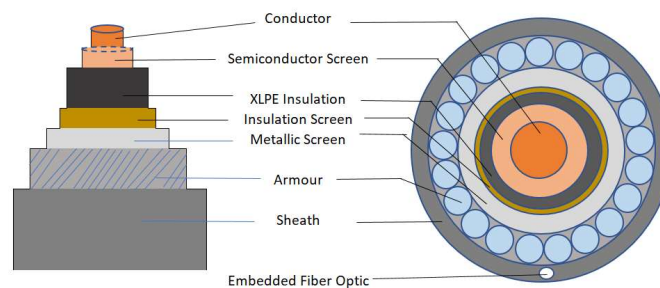


Figure 2-1 Cable lateral and cross section

2.1.1 Conductor

The conductor is placed at the center of the cable. It's made of aluminum or copper depending on the thickness of the cable. Also, there are two designs for a conductor: compact round stranded and segmental “Milliken” stranded. We are here concerned with the 1500 MCM Nexans cable which has a copper conductor in the center which is compact round stranded.

2.1.2 Semiconductor screen on conductor

There is a smooth ultrathin semi-conductor XLPE above the conductors to avoid the concentration of electric fields.

2.1.3 XLPE insulation

To provide the insulation to the conductor working at high voltage from the screen at earth potential, the insulation surrounds the conductor screen. A high-density cross-linked polyethylene polymer is most commonly used for this purpose. It is rated for a continuous conductor current of 90 °C and an emergency current rating of up to 140 °C.

2.1.4 Insulation Screen

The insulation screen provides a uniform electric field distribution, relieves the surge voltage by providing a uniform cable capacitance and provides a low impedance path for the line charging current.

2.1.5 Metallic Screen

The main function of the metallic screen is to nullify the electric field outside the cable, it acts as the second electrode of the capacitor formed by the cable. The metallic screen is connected to the earth at one point along the cable. It also acts as a radial barrier to the humidity from penetrating the cable. This screen also prevents the circulation of the current induced by the magnetic fields from other cables in the vicinity.

The Nexans cable under study also has an optical fiber in one stainless steel tube in the screen and a neutral wire layer. The fibers are wound around the conductor in a helical structure and the length of the fiber around the conductor is known as length of lay. The

scaling factor is the ratio of the length of the fiber to the length of the conductor. The relationship between the length of lay (l), conductor diameter (D), length of the fiber for one complete winding (L_f) and the length of the cable (L) covered by one complete winding of fiber is given below in (2-1). Figure 2-2 shows the diagram of the cable wound with the embedded fiber optic.

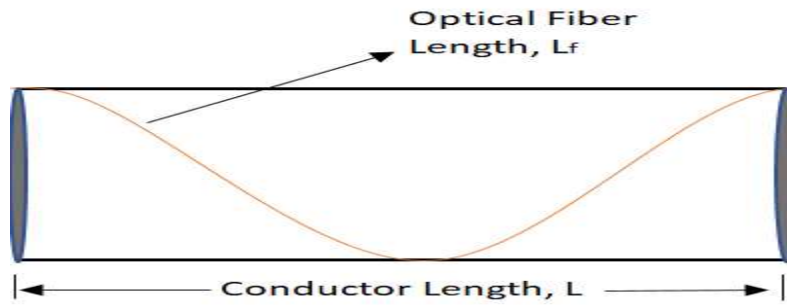


Figure 2-2 Diagram of the cable wound with the fiber optic

$$\frac{L_f}{L} = \frac{\sqrt{l^2 + \pi^2 D^2}}{l} = 1.163 \quad (2-1)$$

The value for this ratio (Scaling Factor) is provided by the manufacturer, Nexans cables.

2.1.6 Sheath

The sheath insulates the metal screen from the ground and protects the metal components of the screen from humidity and corrosion. The sheath should also withstand the mechanical stress. Poly-vinyl chloride (PVC) is mostly used for this purpose for its fire-retardant properties.

2.2 Underground Cable Installations

Duct bank design and configuration like burial depth, geometry and conductor spacing also influence the ampacity of the underground installed cables. The cables are enclosed in the PVC conduits placed inside concrete duct banks. The backfill material is poured over the duct bank instead of native soil as the native soil dries out after some time and is not able to effectively absorb and dissipate the heat from the cable which damages the cable insulation, resulting in the premature failure of the cables. The backfill used has reduced thermal resistance and helps in the proper heat dissipation from the conductor. The different duct configurations for the underground cables at SRP are (roughly) horizontal and vertical arrangements. Three-phase double-circuit lines are mostly placed in the vertical configuration with two spare ducts at the top. The lines can also be placed in the horizontal configurations if there are depth limitations. For example, these limitations can arise from the underlying drain pipes, gas line, water line, other power lines, etc. at the place of installation. The duct configurations for both the vertical and horizontal arrangement are shown in Figure 2-3 and Figure 2-4 respectively.

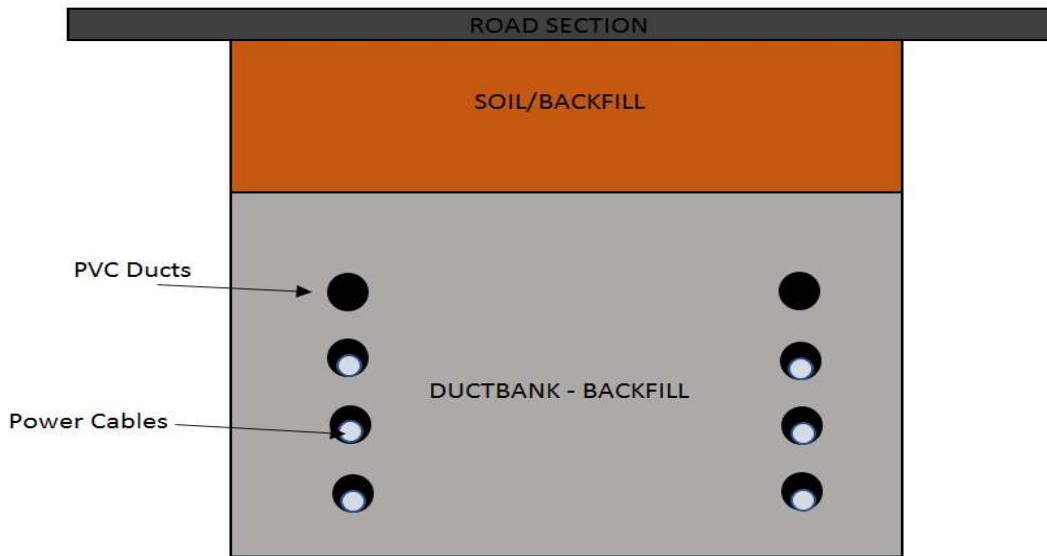


Figure 2-3 Underground cables in vertical arrangement

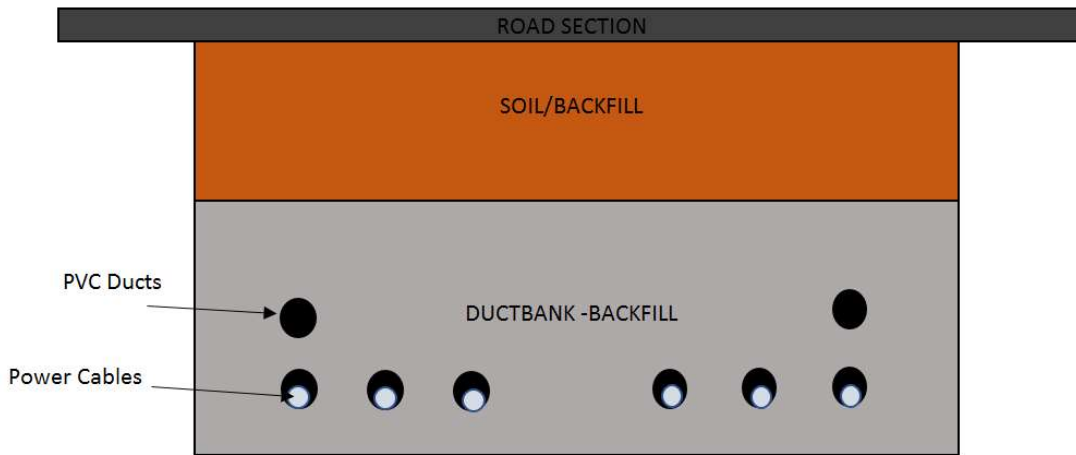


Figure 2-4 Underground cables in horizontal arrangement

2.3 Distributed Temperature Sensing System

The temperature of the optical fiber at any point in the duct along its length is measured using the distributed temperature sensing (DTS) systems. These systems are optoelectronic devices which use fiber optic as sensors. Raman scattering is the inelastic scattering of a photon by molecules which are excited to the higher vibrational or rotational energy

levels and this principle is used in the system to determine the temperature of the fiber at a spatial interval of 1 m with accuracy to within ± 1 °C at a resolution of 0.01 °C. The output of this system provides a temperature profile along the cable which in turn helps in determining the hotspot location.

2.3.1 Principle and Working of DTS systems

Optical fibers are made from the doped quartz glass. Quartz glass is a form of silicon dioxide (SiO₂) with amorphous solid structure. Increase in the temperature of the conductor induces lattice oscillations within the solid. When light falls onto these thermally excited molecular oscillations, an interaction occurs between the light particles (photons) and the electrons of the molecule [2]. The back scattered light consists of three components; Rayleigh scattering, Stokes scattering and anti-Stokes scattering. Stokes and anti-Stokes are components of the Raman scattering and these are used for the temperature calculations. The light intensity of the anti-Stokes band is dependent on the temperature and the ratio of Stokes and anti-Stokes light intensities is used to determine the local temperature. Equation (2-2) provides the local temperature calculation using the Stokes and anti-Stokes ratio [3].

$$T(z, t) = \frac{\gamma}{\ln\left(\frac{P_S(z,t)}{P_{aS}(z,t)}\right) + C(t) - \int_0^z \Delta\alpha(z') dz'} \quad (2-2)$$

where T is the absolute temperature (K) and z is the distance along the cable with $z = 0$ at the DTS instrument. The numerator γ (K) depends on the distribution of quantum states, $\gamma = \hbar\Omega/k$,

with \hbar being Planck's constant, Ω is the difference in the frequency between the backscattered Stokes radiation and the incoming laser pulse, and k is the Boltzmann's constant. The ratio $\left(\frac{P_S(z,t)}{P_{AS}(z,t)}\right)$ is the measured ratio between the power of the Stokes (S) and anti-Stokes (AS) backscatter reaching the instrument. The integral in the denominator represents the product of the length and the differential attenuation of the Stokes and anti-Stokes radiation caused by the differences in the absorption coefficients for both the Stokes radiation caused by the differences in the absorption coefficients for both the frequencies. The term $C(t)$ accounts for the differences in effective detector sensitivities with respect to the Stokes and anti-Stokes photons, which may vary in time [3]. Figure 2-5 shows the basic workings of a distributed temperature sensing system.

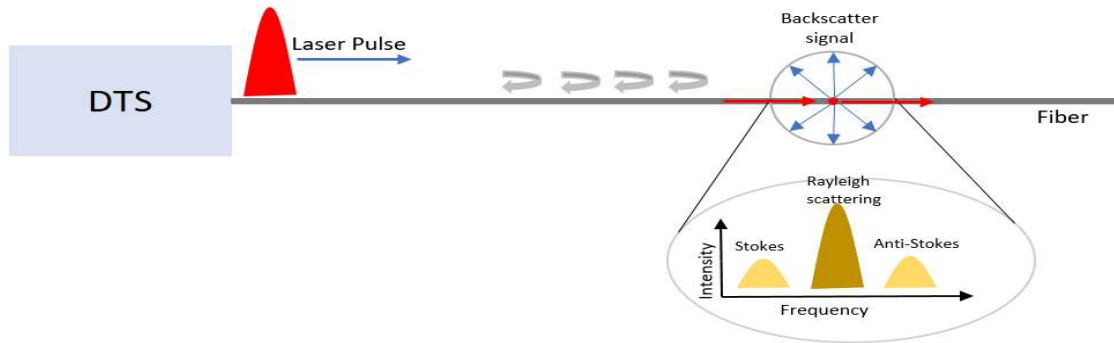


Figure 2-5 Working of distributed temperature sensing system

2.3.2 Single Ended and Double Ended Measurement

The DTS system provides two options of measurements: single-ended and dual-ended measurements. With the single-ended measurement, laser pulses are injected and monitored only from one end of the fiber and the backscatter data are used to calculate the temperature. After the Raman scattering event, the scattered light travels back from the

point of scatter to the instrument's photon detectors at $z = 0$. Over this length of the fiber, both the anti-Stokes and Stokes signals are also attenuated [4]. To improve the accuracy of the data obtained through the Stokes and anti-Stokes intensities, (2-2) must be adjusted to allow for the single-ended measurement.

$$T(z, t) = \frac{\gamma}{\ln\left(\frac{P_S(z,t)}{P_{aS}(z,t)}\right) + C - \Delta\alpha z} \quad (2-3)$$

Similarly, for the dual-ended measurements, the pulses are injected and monitored from both ends of the fiber, alternating after each measurement interval. The main motivation for the dual-ended measurements is that it allows the DTS to remove the noise data that a single-ended measurement would erroneously interpret as temperature valid data. In (2-2), the term $\Delta\alpha(z)$ represents the differential attenuation of the Stokes and anti-Stokes backscatter along the cable. The temperature is measured from both ends of a fiber in the dual-ended measurement. Equations (2-4) and (2-5) represent the measured temperature of a single point on the fiber, of length L , from two different ends of the fiber. This point is at a distance of z units from one end and at $L-z$ units from the other end of the fiber.

$$T(z) = \frac{\gamma}{\ln\left(\frac{P_S(z,t)}{P_{aS}(z,t)}\right) + C - \int_0^z \Delta\alpha(z') dz'} \quad (2-4)$$

$$T(L - z) = \frac{\gamma}{\ln\left(\frac{P_S(z,t)}{P_{aS}(z,t)}\right) + C - \int_z^{L-z} \Delta\alpha(z') dz'} \quad (2-5)$$

Since $T(z)$ should be equal to $T(L - z)$, as they represent the temperature of the same point on the fiber, by equating (2-4) and (2-5) we obtain a value for the differential

attenuation at each step of Δz , as provided by (2-6). This value of differential attenuation is used by the DTS to calibrate the temperature data during dual-ended measurements.

$$\int_z^{z+\Delta z} \Delta\alpha(z')dz' = \frac{\ln\left(\frac{P_S(z+\Delta z)}{P_{aS}(z+\Delta z)}\right)_{\Rightarrow} - \ln\left(\frac{P_S(z)}{P_{aS}(z)}\right)_{\Rightarrow} + \ln\left(\frac{P_S(z)}{P_{aS}(z)}\right)_{\Leftarrow} - \ln\left(\frac{P_S(z+\Delta z)}{P_{aS}(z+\Delta z)}\right)_{\Leftarrow}}{2} \quad (2-6)$$

2.3.3 Optical Fibers

Optical fibers are selected based on their application, cladding and diameter. There are basically two types of fibers that allow for the different light propagation modes. A ‘single-mode’ fiber is very small in diameter, about 8-10 microns, and allows only one mode of light to travel at an instant. Multi-mode (MM) fibers are 50-100 microns in diameter and allow many light pulses of different propagation modes to travel through the core simultaneously. The fiber used in this distributed temperature sensing system is a multi-mode fiber with a diameter of 50/125-micron with a range of 20 km, where 50-micron is the inner diameter of the fiber cladding and 125-micron is the outer diameter of the fiber cladding. There are 2 fibers (1 fiber loop) for each cable in the circuit and two fiber loops are laid into the spare duct.

2.4 Basic principle for temperature prediction

In 1949, in a paper, [7], written by J. H. Neher, conditions for the heat flow from the power cables were idealized by assuming the thermal resistivity of the surrounding soil to be constant. This helped in applying the superposition theorem. Superposition theorem states that, the temperature existing at any point in the general heat field becomes equal to the sum of the temperature changes produced at that point by each of the respective heat fields operating as if by themselves [7]. It was also assumed that the earth was initially at a

constant ambient temperature throughout and the heat can be dissipated constantly at the earth air boundary, so there is no temperature rise at the earth's surface, i.e., the earth's surface is modeled as an isothermal boundary.

Figure 2-6 shows the buried power cable at point O at a depth of h (m) from the earth's surface. Point E represents the origin and it lies at the earth's surface. To find the temperature at a point P, which is at a depth y (m) from the earth's surface and at a horizontal distance of x (m) from the line joining EO, we need to assume that the conductor radiates Q_c watts per unit meter and is buried in an infinite medium of constant thermal resistivity, ρ ($^{\circ}\text{C}\cdot\text{m}/\text{W}$). The steady state temperature, T , at any radius r , as a function of the heat flow is given by the differential equation in (2-7).

$$\frac{dT}{dr} = -\frac{Q_c \rho}{2\pi r} \quad (2-7)$$

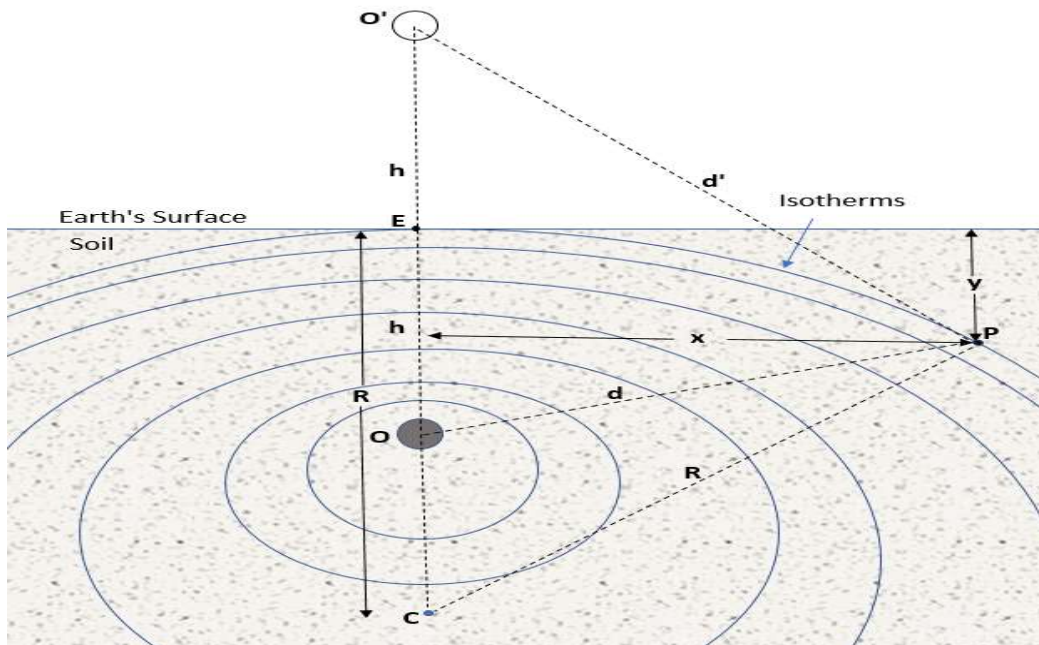


Figure 2-6 Cross-section of the buried cable and isothermal surfaces from heat flow

The total temperature rise above the earth's constant ambient temperature is calculated by integrating (2-7) from $r = \infty$ to $r = d$, where d is the distance from the conductor, to yield ΔT , (see (2-8)) which is the rise of the temperature, at point P, above the ambient temperature.

$$\Delta T = - \int_{\infty}^d \frac{Q_c \rho}{2\pi r} dr \quad (2-8)$$

Similarly assume that there is another conductor at height h above the earth's surface, absorbing Q_c watts per meter. The total temperature rise at point P will be

$$\Delta T = - \int_{\infty}^d \frac{Q_c \rho}{2\pi r} dr + \int_{\infty}^{d'} \frac{Q_c \rho}{2\pi r} dr \quad (2-9)$$

$$\Delta T = \frac{Q_c \rho}{2\pi} \ln \frac{d'}{d} \quad (2-10)$$

The temperature rise obtained is in °C. From Figure 2-6, we can write d and d' in terms of h , x and y .

$$d'^2 = (h + y)^2 + x^2; \quad d^2 = (h - y)^2 + x^2 \quad (2-11)$$

If we represent d'/d as k , (2-11) can be modified to:

$$\left\{ y - h \left(\frac{k^2 + 1}{k^2 - 1} \right) \right\}^2 + x^2 = 4h^2 \left(\frac{k}{k^2 - 1} \right)^2 \quad (2-12)$$

Equation (2-12) represents the equation of a circle, which is also the locus of isothermal points around the conductor at O, with radius R , where $R = 2h \left(\frac{k}{k^2 - 1} \right)$. The center of this

circle, C, lies directly below the conductor. This means that for various values of the temperature rise, ΔT , the locus of the isothermal points is a family of eccentric cylinders, marked as 'isotherms' in Figure 2-6, about point O if ΔT is positive and about O' if ΔT is negative. The distances of point E, in Figure 2-6, from the power cable and its image are equal, therefore ΔT is zero at that location. A plane passing through E represents the locus of isothermal points with no temperature rise due to the heat dissipation from the conductor. The isothermal circles in Figure 2-6 increase in diameter as the value of d'/d increases and they merge into a plane passing through E and this plane perpendicularly bisects the line OO'. If this plane is kept at a constant temperature ($\Delta T = 0$), then (2-10) represents the temperature rise at any point P due to the heat generated by the conductor at point O [7].

From (2-12), it can be concluded that the temperatures at all the points on the circle defined by (2-12) will be equal. The center of that circle will lie somewhere below the conductor. This principle will be used to develop the models in MATLAB and CYMCAP.

2.5 Power Cable Ladder model

The equation of heat conduction in soil is given by (2-13)

$$\frac{\partial}{\partial x} \left(\frac{1}{\rho} \frac{\partial T}{\partial x} \right) + \frac{\partial}{\partial y} \left(\frac{1}{\rho} \frac{\partial T}{\partial y} \right) + W_{int} = c \frac{\partial T}{\partial t} \quad (2-13)$$

where ρ = thermal resistivity, °C-m/W

W_{int} = heat generated from the heat source buried in soil

$\frac{\partial T}{\partial x}$ = temperature gradient in x direction

c = volumetric thermal capacity of soil, J/m³-°C

The solution to the above equation can be found by applying various boundary conditions, due to different soil layers surrounding the heat source, from the conductor to the surface. A challenge in finding the temperature distribution using the above equation occurs when different layers of the soil have different thermal properties. However, an analytical solution can be obtained by treating the power cable as a line source in a homogenous soil while assuming that the earth's surface is an isotherm.

There is much similarity between the heat flow and the current flow in a medium. Fourier's law for the heat transfer resembles the equation for the Ohm's law. Similarity between the two, can be seen by using the lumped parameter method to solve the differential equation for the current flow due to the potential difference between any two points. The method involves dividing the material into several volumes each with its own thermal resistance and capacitance [8]. The thermal resistances restrict the heat flow and the thermal capacitances act as heat absorbing units. Calculation of these thermal resistances and capacitances is explained in the following section.

2.5.1 Calculation of Thermal Resistances and Capacitances

Dielectric losses and iron losses play a key role in heating of the cable. The heat dissipation from the cable occurs through the cable insulation and surrounding soil. The ability of a material to resist the heat flow is called its thermal resistance. For any cylindrical pipe with inner radius r_1 , outer radius r_2 and a thermal resistivity of ρ , the thermal resistance per unit length is defined as:

$$T = \frac{\rho}{2 * \pi} * \ln \frac{r_2}{r_1} \quad (2-14)$$

Next the thermal capacitance to be used in our model must be derived. The temperature distribution within a cable is dependent on the time and can be solved by using the lumped capacitance method [8]. The insulation and surrounding soil act as the thermal capacitance and absorb/store the heat from the conductor. The cable insulation and surrounding soil are divided into small volumes and a thermal capacitance is determined for each of these divisions. This theory was developed by Van Wormer [8] in 1955. It states that the thermal capacitance, Q , for a coaxial configuration with the internal and external diameters, D_1 and D_2 , respectively, is given by,

$$Q = \frac{\pi}{4} * (D_2^2 - D_1^2) * c \quad (2-15)$$

where c is the volumetric heat capacity of the material.

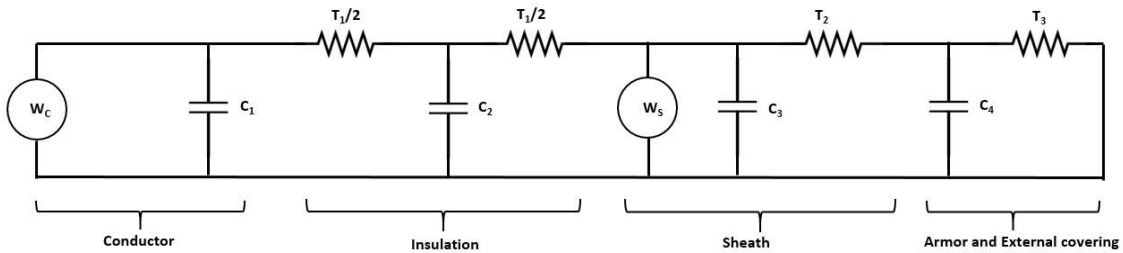


Figure 2-7 Ladder circuit for a cable showing each layer as RC circuit

Using these formulae to calculate the thermal resistance and capacitance, a ladder circuit can be developed for a power cable as shown in Figure 2-7 [8]. In Figure 2-7, W_C and W_S represent the heat generated in the conductor and the cable dielectric respectively. Although the dielectric loss is distributed across the cable insulation, the correct

temperature rise is obtained by considering that all of the dielectric loss occurs at the midpoint of the thermal resistance between the conductor and sheath [8]. The thermal resistance and capacitance for the insulation, sheath and armor are denoted by T_1 , T_2 and T_3 and C_2 , C_3 and C_4 respectively. The thermal capacitance of the conductor is denoted by C_1 . This ladder circuit may be further reduced to a two-loop network to simplify the calculations [8]. This two-loop network will be used to develop the MATLAB models shown in the Chapter 6.

2.6 Soil Ladder Model

The techniques contained in [9] can be used to determine the value of soil thermal resistances. This was used as a basis for determining the soil thermal resistances for our model. As explained through Figure 2-6, a heat generating (loaded) buried power cable will form cylindrical isothermal surfaces around it. The centers of these isothermal surfaces are located directly below the power cable. Once the center of the isothermal surface passing through the point of interest is located, the soil can be divided into many concentric isothermal surfaces with (possibly) increasing radii leading up to the point where we wish to determine the temperature.

Figure 2-8 shows our power cable and the soil surrounding it, which is divided into a few layers. The ‘cable’ icon in Figure 2-8 represents the ladder network for the power cable, as shown in Figure 2-7. Each layer of the soil is assigned its own thermal resistance and capacitance.

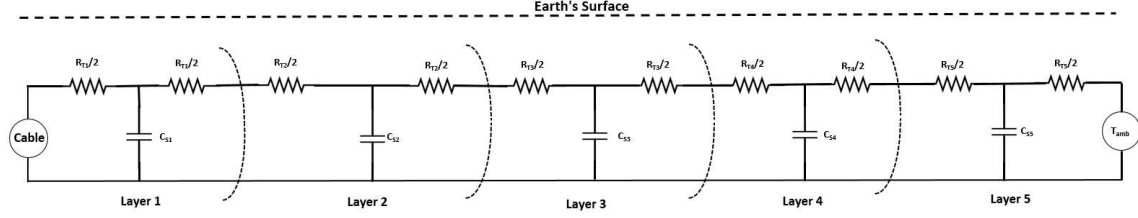


Figure 2-8 Soil ladder model for a buried cable

All the layers represent different concentric circles leading up to a point where the earth reaches its constant ambient temperature, T_{amb} both at the earth's surface and at remote earth. The thermal resistances and capacitances can be calculated by using the following formulae [9],

$$R = \frac{\rho_{soil}}{2\pi} \left(1 + \frac{th}{r_{int}} \right) \quad (2-16)$$

$$C = \pi(r_{ext}^2 - r_{int}^2) \cdot C_{soil} \quad (2-17)$$

where ρ_{soil} is the thermal resistance of the surrounding soil, th is the thickness of the layer, r_{int} and r_{ext} are the internal and external radii of a layer, and C_{soil} is the volumetric heat capacity of the soil.

The resistances between the two consecutive capacitors, shown in Figure 2-8, are added together in series to form a single thermal resistance which is given by the formula as given by (2-18), where i is the layer number, and N is the total number of layers.

$$\begin{aligned} R_{s0} &= 0.5R_{T1} \\ R_{si} &= 0.5(R_{Ti} + R_{Ti+1}) \\ R_{sN} &= 0.5R_{TN} \end{aligned} \quad (2-18)$$

It was also observed that, greater the number of layers, more accurate was the solution. Also with the number of layers between three and six, the accuracy of about 0.5 °C can be obtained by this method [9].

To distribute the layers, exponential discretization of the soil is proposed as follows [9],

$$b_i = r_{cable} + (d_m - r_{cable}) \cdot \frac{e^{\gamma \cdot i} - 1}{e^{\gamma \cdot N} - 1} \quad (2-19)$$

where b_i are the radial positions of the layer borders, r_{cable} is the radius of the power cable, d_m is the depth of the model or the distance to the center of isotherm from the earth's surface, and γ is the argument of the exponential distribution given in [9] (and should be a positive number.)

The depth of the model can be determined by using the following formula.

$$d_m = h + \sqrt{h^2 - r_{cable}^2} \quad (2-20)$$

This process is used to divide the surrounding soil into multiple layers and then compute the thermal resistance and thermal capacitance values. All the calculations are shown in Chapter 6.

3 BRANDOW PICKRELL EXISTING INTALLATION

3.1 Overview

The Brandow – Pickrell 69 kV transmission line consists of two overhead sections and one underground section which together connect the SRP owned substations Brandow and Pickrell. The underground section connects the overhead conductors which terminate at SRP riser poles P24 and P30 located at the N-E and S-E corners, respectively, of Rio Salado and Priest Dr. in Tempe AZ. Figure 3-1 shows an overhead view of the underground path of the Brandow to Pickrell underground line.



Figure 3-1 Overhead view of Brandow-Pickrell underground installation

The underground circuit consists of six (two per phase) 1500 MCM high voltage cables manufactured by the Nexans of Germany. Each cable contains two 50/125-micron multimode (MM) optical fibers. When the installation was constructed in 2003, the optical fibers of the

Nexans cables were spliced at the riser pole insulators to six strands, riser grade, 62.5/125-micron MM optical fibers manufactured by Corning Optical. The Corning cables were brought down the riser poles to the termination boxes approximately ten feet from the riser pole's base. Figure 3-2 shows the fiber splice box on the riser pole P30. Also, one of the spare ducts has two loops of the fiber-optic cable installed in it. Each fiber optic has six strands of 50/125-micron MM optical fibers.



Figure 3-2 Splice box on riser pole P30

3.2 Duct bank Configurations

Various duct bank configurations are used in this installation. These configurations were selected based on the limitations of space and other factors such as the underground power line crossing, water pipe, etc. There are four different duct-bank configurations in this installation. The vertical configuration, horizontal configuration, vertical configuration at manholes and risers and a modified configuration for the reinforced section. Figure 3-3 shows various sections of the installation with different duct bank configurations.

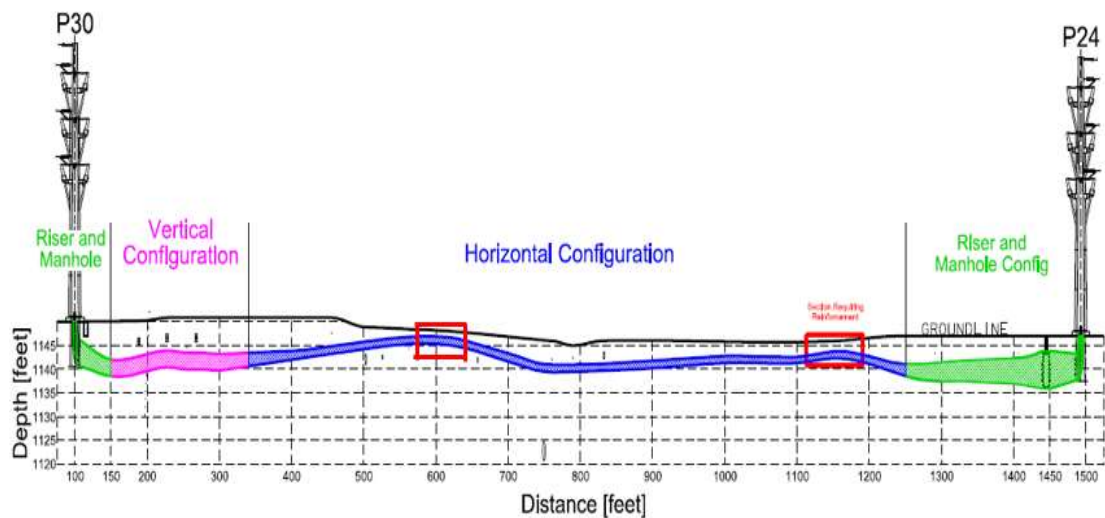


Figure 3-3 Sections with different duct bank configurations

These duct banks consist of the conductors, PVC conduits, backfill material and native soil. The PVC conduits were laid in the duct and the trench was packed with an encasing material which is a 1.5 sack (cement content should not be less than 141 pounds per cubic yard) of controlled low strength material. The controlled low strength material, also known as flowable fill, is a fluid concrete mix. The low strength material generally consists of washed gravel and sand slurry, with cement and is used as a backfill. This part was then packed on top with the backfill material of a lower thermal resistance. The different sections with their duct configurations are shown in figures (Figure 3-4 to Figure 3-6) below.

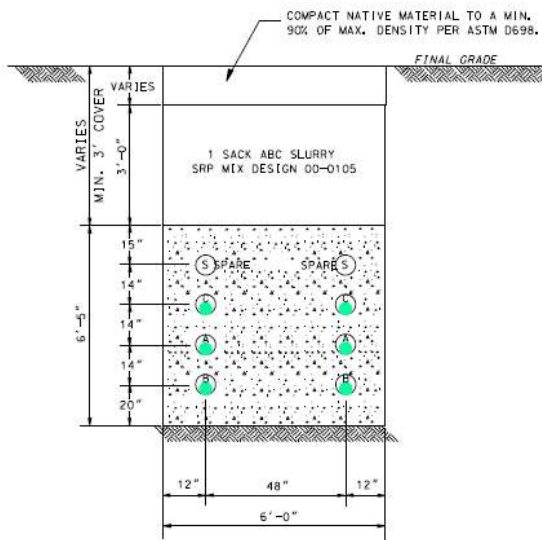


Figure 3-4 Vertical duct bank arrangement for manhole and riser section

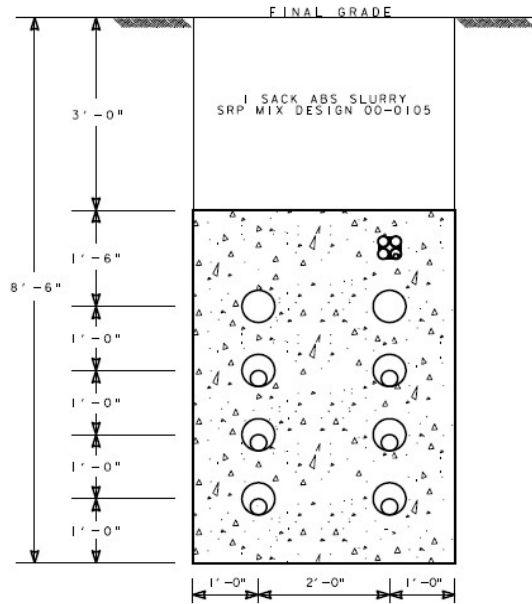


Figure 3-5 Vertical duct bank arrangement for installation

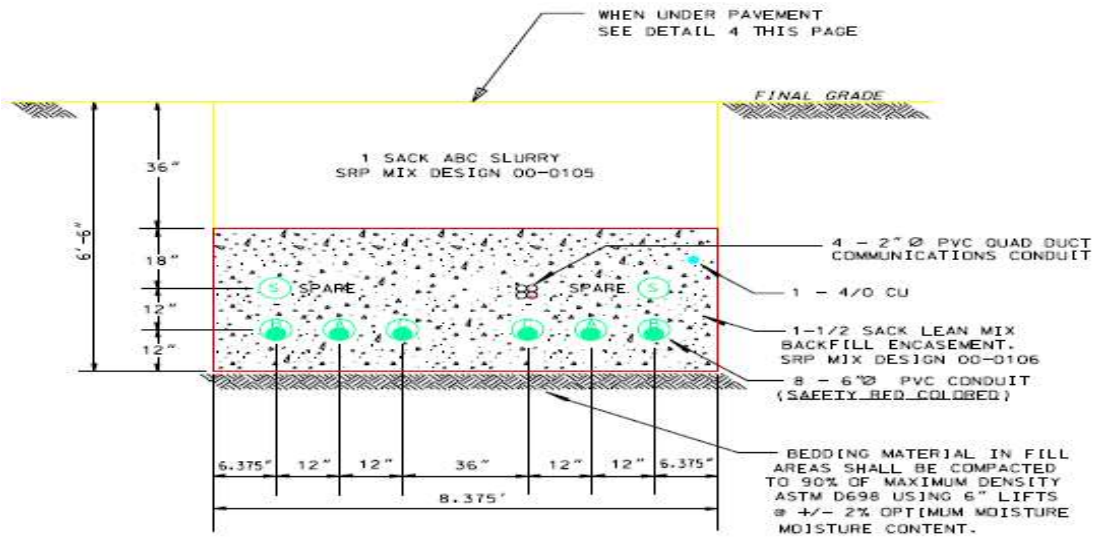
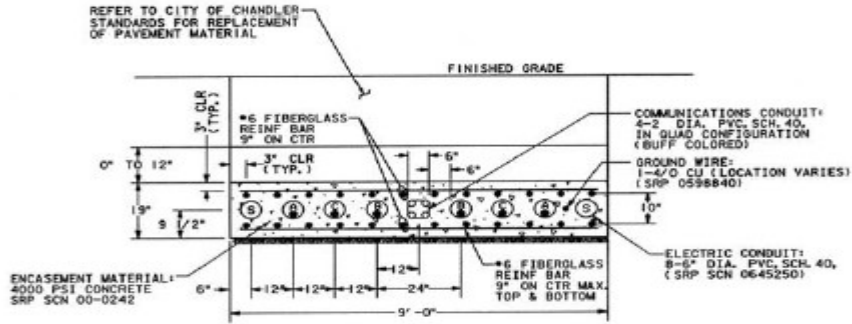


Figure 3-6 Horizontal duct bank arrangement for installation



Ⓣ TYPICAL FLAT TRENCH SECTION

Figure 3-7 Reinforced trench section of the installation

Figure 3-3 shows two areas marked with the red squares, these sections of the cable installation are very close to the road surface due to some underlying communication fiber and water lines. In order to provide extra strength to the trench section at these points, the encasement material used was a structurally reinforced concrete and no thermal backfill was used between the asphalt and duct bank. Figure 3-7 shows the original design for the section with additional reinforcement.

3.3 DTS Installation

This section describes the physical installation of the OTS3 model of the DTS with six ports, which was used for making the measurements in this work and replaces the existing OTS2 model with two ports, which was used in a previous study conducted by Travis Stowers [5]. To understand the interpretation of the results section (provided in later chapters) it is not necessary to read this chapter.

The model OTS2, DTS that existed in the enclosure at the beginning of this project was replaced with a new DTS, model OTS3, as the old DTS had only 2 ports, which were

insufficient for the measurements that needed to be performed. The new DTS has six ports which can be used to measure the temperatures simultaneously from different fibers. The DTS was connected to the fibers from the spare duct and the fibers from the power cable using E2000 connectors. The fiber installation is explained in the next section.

3.3.1 Fiber-Optic Cable Installation and Splicing

A fiber installation was required to collect the temperature data of the installation through the DTS. Due to feasibility issues, the crew elected not to install the new fibers in the duct with the power cable since the fiber blasting through the sealing foam could have damaged the cable. The fiber-optic cable was laid into the spare duct using a cable pulling technique. Once the fiber was installed, it was required to be connected with the DTS. A riser molding cover was used to bring the fiber from the base of the riser pole to the junction box. Once the fibers were brought to the DTS enclosure, two E2000 connectors were spliced to each of the fibers. The fibers come marked with the length markings every few meters as shown in Figure 3-8.



Figure 3-8 Fiber length marking

These length markings can be used to measure the length of the fiber by taking the difference of the length markings between any two points on the fiber. The length of the fiber from the DTS enclosure to the man-hole is calculated by taking the difference between the values of the two length markings on the fiber in the manhole and on the same fiber at the DTS. Pictures of the length marking were taken during the installation using a high-resolution camera.

4 DTS COMMISSIONING AND PRELIMINARY RESULTS

The OTS3 DTS was installed in the enclosure occupied by the previous model OTS2 DTS, approximately 3 feet east of the P24 pole. The cable fibers were connected to channel 1 and channel 2 of the DTS with E2000 connectors. For the fibers in the spare duct, two fibers were connected to channel 3 and channel 4 and the other two to channel 5 and channel 6, respectively. The DTS was configured when the fibers were connected for the first time. The configuration details are explained in the following sections.

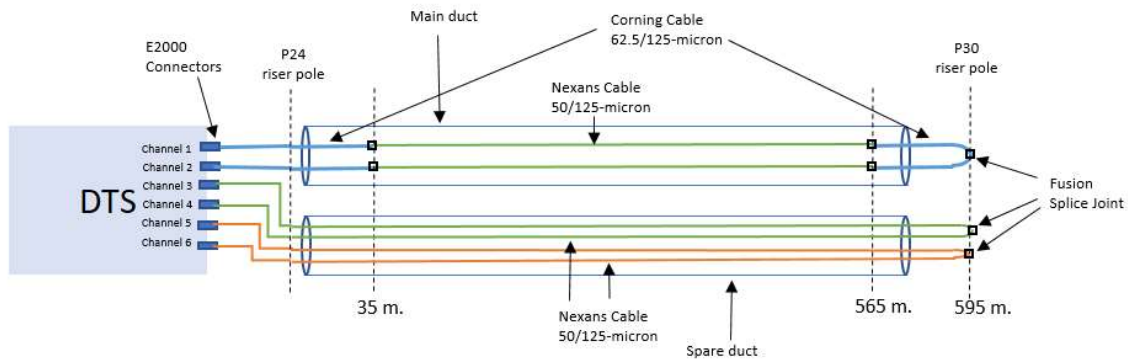


Figure 4-1 Schematic diagram for the Brandow-Pickrell fiber optic arrangement

4.1 Fiber Scheme

It should be noted that the channel 1 and channel 2 are connected to different ends of a single fiber loop. This fiber loop is embedded in the power cable, which is installed in the duct (from here on referred to as the main duct), and consists of the Corning fiber-optic cable (blue) of 62.5/125-micron diameter which is spliced with the Nexans fiber-optic cable (green) of 50/125-micron diameter. The fibers are spliced together at one end to form a continuous fiber loop. Channel 3 and 4 are connected to the two fibers which are spliced together at P30 pole to form a fiber loop in the spare duct. Similarly, channel 5 and 6 are

connected to the two fibers, which are spliced together at P30 pole to form the second fiber loop, installed in the spare duct as shown in Figure 4-1. Splicing of the ends of the fibers are necessary to form the fiber loops for the dual-ended measurements. These fibers are 62.5/125-micron diameter Nexans fiber-optic cables. One of the fibers (shown in orange in Figure 4-1) in the spare duct will be used for the single-ended measurement. These configurations are made using a software application, Charon3, by Lios Technology.

4.2 Charon3 Software

The DTS was configured using the configuration application, Charon3®, by Lios Technology. Charon3 software acts as a digital user interface for the DTS. The software was installed on a laptop and was connected to the DTS's controller using a USB connector cable. Once the controller is detected by the Charon3 software, a QuickStart application (as shown in Figure 4-2) starts automatically. The QuickStart application from the installed software checks for the controller connection with the software. It displays an interface which allows the user to control the DTS controller via the laptop and provides an option to scan all the fibers. The lengths of all the fibers are the outputs of QuickStart's scanning operation. All the fibers are scanned repeatedly until the length of fiber measured from one end in the fiber loop is found to be equal to the fiber length measured from the other end in the same fiber loop. Figure 4-2 shows the scanned lengths of the fiber connected to each channel.

Scanning operation provides us the length of the fibers connected to each channel as detected by the Charon3 software through the DTS. These lengths are measured by firing a laser pulse in each of the channels one at a time. The measured length of the fiber loop

which is connected to the channel 1 and 2 includes the length of both, the Corning cable of 62.5/125-micron diameter and the Nexans cable of 50/125-micron diameter. To find the correct length of the conductor, we need to subtract the length of the Corning cable installed from the DTS to the riser and apply the scaling factor to the length of the Nexans fiber. Also, the scanned lengths from the channel 3 to channel 6 provide the length of the fibers in the spare duct.

Channel	Length / m	Status	Last Commissioning
4384			
1	1190.5	OK	12/30/2016 2:17 PM
2	1190.5	OK	12/30/2016 2:16 PM
3	947.5	OK	12/30/2016 3:05 PM
4	947.5	OK	12/30/2016 3:04 PM
5	947.5	OK	1/9/2017 1:58 PM
6	946.5	OK	1/9/2017 1:59 PM

Figure 4-2 Quick Start application showing the scanned lengths of the fibers

Once all the fibers were scanned, the measurement controller input to the DTS (through the Charon3 software) was set to measure temperatures from one channel for two minutes at 1 m spatial intervals along a single fiber length and then move on to monitor the next channel.

Using this protocol, it took a total of twelve minutes to monitor all the channels. Finally, the loop configuration settings (see Figure 4-3) were also set-up in the DTS using the Charon3 software for the DTS controller to identify the channels connected to the different ends of the same fiber loop. It was necessary to tell the controller which measurements

were dual-ended measurements, i.e., which measurements corresponded to the fiber loops. All configuration settings are shown in Figure 4-3 and Figure 4-4.

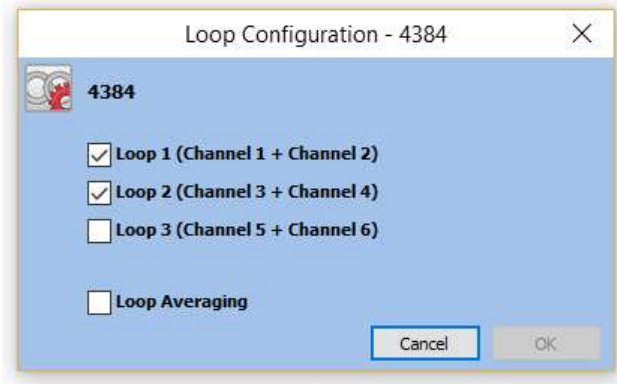


Figure 4-3 Loop configuration setting of the DTS

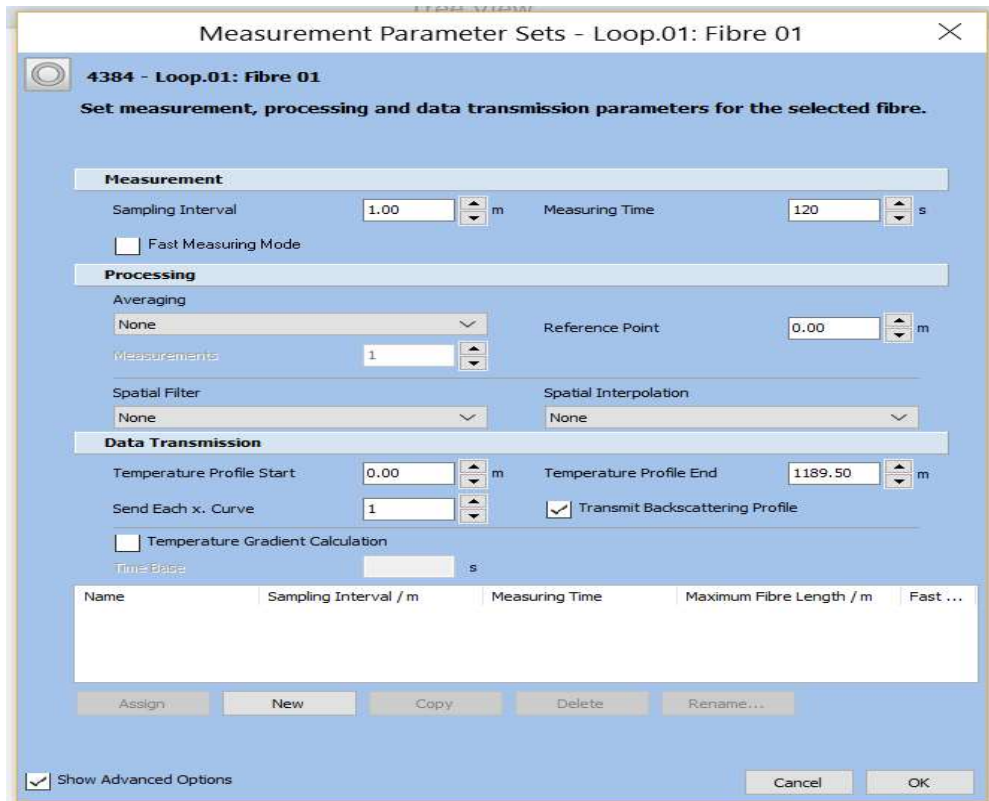


Figure 4-4 Measurement parameter setting for the DTS

‘Measurement Parameter Sets’ as shown in Figure 4-4 allows one to modify the parameters like sampling interval, measuring time, starting and ending points for the temperature measurement, backscatter data and averaging measurements.

4.3 Measurement Phase Selection

The A phase on the south side of the installation (SA) of the circuit lies between B and C phases in the installation and therefore it was selected for the measurement assuming that it will have the highest temperature rise among all the phases.

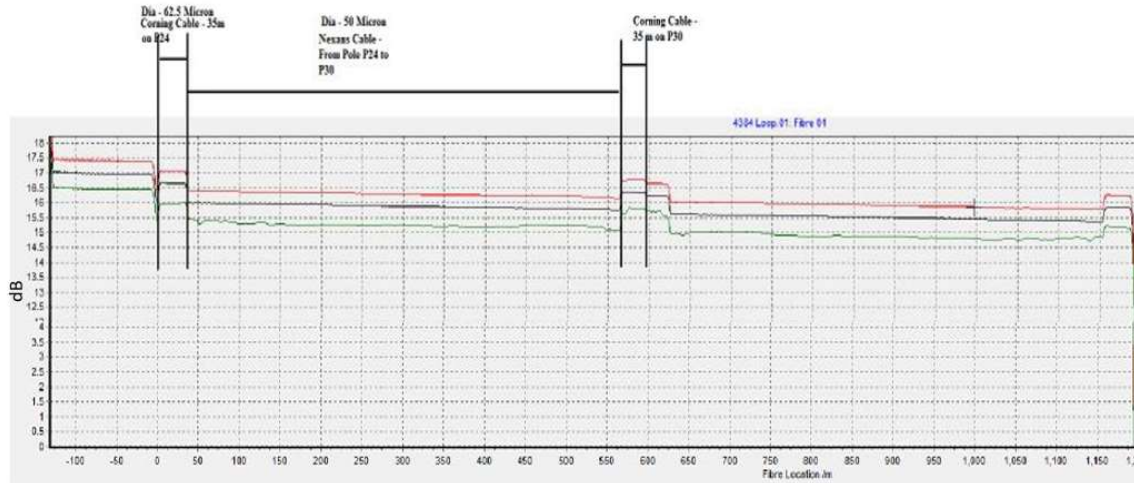


Figure 4-5 Backscatter plot for the fiber in the power cable in the main duct

Figure 4-5 provides the backscatter data for the fiber loop connected to the channels 1 and 2, which can be used to determine the lengths of the fiber and location of the splice joints on the fiber. From the experiment conducted in Travis Stower’s project [5], it was observed that the fiber with a larger diameter had a higher intensity of backscatter signal. Since the Corning cable has a larger diameter than the Nexans cable, the backscatter signal intensity

in the Corning cable should be higher than in the Nexans cable. The following paragraph explains the steps involved in measuring the cable length from the backscatter data.

As can be seen in Figure 4-5, the signal starts from 0 m, which indicates the location of the DTS equipment. The intensity of the backscatter signal changes with the diameter of the fiber. The plot shown in Figure 4-5 represents the complete fiber loop from the DTS to the splice box at the P30 pole and back to the DTS. Therefore, the splicing joint at P30 occurs at the midway point of the total fiber loop length. The higher intensity signals up to 35 m represents the backscatter from the Corning cable of 62.5-micron diameter and from 35 m to 565 m is the backscatter signal from the Nexans cables of 50-micron and from 565 m to 595 m is again the Corning cable with the larger diameter. The signal beyond the 595 m point is the return leg of the loop. Since the Nexans cable are wound around the conductor, we need to apply the scaling factor to determine the length of the conductor.

The scaling factor for this installed cable was provided by the cable manufacturer and was 1.163. Since the fiber length was known from the backscatter plot, the length of the conductor in the underground installation was calculated using the following:

$$\text{Length of the conductor} = (565-35)/1.163 = 455.717 \text{ m} = 1495 \text{ feet}$$

4.4 Preliminary results

The data received from the DTS were analyzed and plotted. It was observed that the data points on the fiber in the main duct and fiber in the spare duct were not aligned because the fiber in the power cable was wound around the conductor and hence, it was longer than the fiber in the spare duct for the same duct length. Since the DTS controller was taking the

temperature measurements at 1 m. intervals along the fiber length, the number of data points collected were more for the fiber in the power cable in the main duct than for the fiber in the spare duct. To align the data points for both of the fiber measurements, the section lengths from pt. A to pt. B were calculated and are shown in Figure 4-6. This section was selected because both the fibers were running parallel to each other in this section; unlike the fibers on the poles where fiber from the spare duct goes to a splice box and is then rerouted to the DTS; whereas the fiber embedded in the main power cable runs along the power cable to the insulators on top of the riser poles.

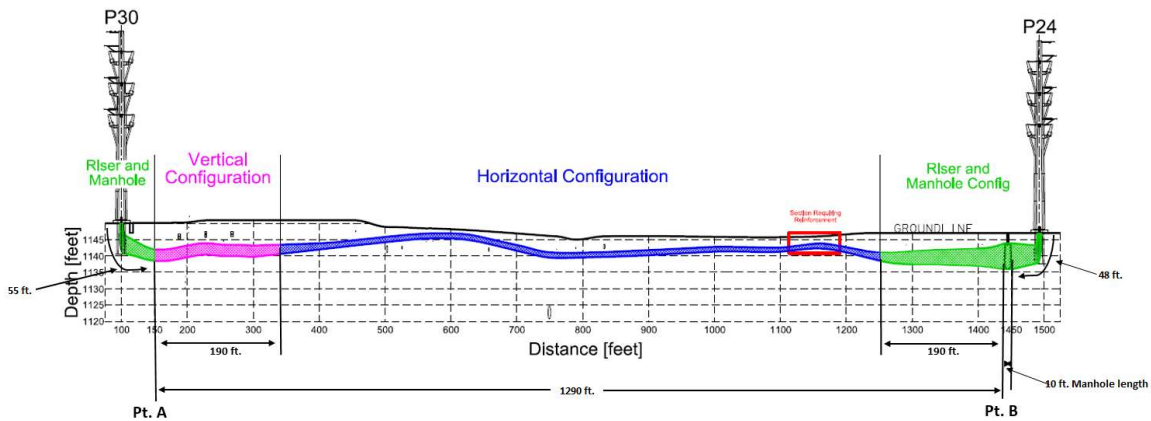


Figure 4-6 Section layout with the length markings along the installation

Length measurements were made to locate the corresponding starting pt. A and end pt. B on the fiber temperature data measurements. Since, the Nexans fiber in the main power cable is spliced with the Corning fiber at one of the riser pole insulators, the length markings on the fiber could not be used to determine the length of the embedded fiber from the DTS to the manhole; therefore, as-built drawings were used to determine the height from the base of the riser pole to the riser pole insulator with the fiber splicing joint. Since, some portion of the Nexans fiber was installed along the riser pole we were able to

determine the length of the fiber using the as-built drawings of the riser pole. Next the length of the fiber from pt. A to the pole base was calculated using the length markings on the spare duct fiber. The power cable also follows the same route from the pt. A to the riser pole base, therefore its length was also assumed to be equal to the length of the spare fiber for that section of the installation. To calculate the length of the fiber embedded in the power cable from pt. A to pt. B in Figure 4-6, the sum of the length of the power cable along the riser pole P24, the length of the power cable from the base of the riser pole P30 to the splicing box, the length of the power cable from the pt. A to the riser pole P30 base and the length of the power cable from the pt. B to the riser pole P24 base was scaled using the scaling factor, as provided in (2-1), and subtracted from the total length of the Nexans fiber cable (obtained from the backscatter plot). To determine the length of the spare fiber, the sum of the length of the fiber from the manhole to the DTS and the length of the fiber from the pt. A to the splice box on the riser pole P30 is subtracted from the total length of the spare fiber from the DTS near P24 to the splice box on the riser pole P24. The measured and calculated lengths are shown in Table 4-1 for the power cable fiber in the main duct and Table 4-2 for the fibers in the spare duct. These lengths are shown in Figure 4-6.

Table 4-1 Power cable fiber length measurement from pt. A and pt. B

For Fiber 1 (Power cable in Main duct)	Units ft.(m)	Data Source
Length of Corning Cable of 62.5-micron dia. from splicing joint on P24 to DTS	114.83 (35)	Backscatter plot
Length of Corning Cable of 62.5-micron dia. from splicing joint on P20 to midpoint of fiber measurement	98.43 (30)	Backscatter plot
Riser Poles Height (up to splicing joint of Nexans and Corning cable)	46 (14.02)	AutoCAD Official UG Drawing
Distance from Splice joint on P24 to Manhole	94 (28.65)	Length markings on the fiber
Manhole Length	10 (3.048)	As-built drawings
Scaling Factor for wound fiber	1.16299	Provided by cable manufacturer
Total Length of measured Nexans fiber	1738.85 (530)	Backscatter plot
Scaled length of measured Nexans fiber	1495.15 (455.72)	
Scaled Length of fiber from Pt A to Pt B	1290.15 (393.24)	

Table 4-2 Fiber length measurement in the spare duct from pt. A to pt. B

For Fiber 3 and Fiber 5 (Spare Duct)	Units ft.(m)	Data Source
Length of spare fiber	1555.12 (474)	Backscatter plot
Fiber length from Manhole (pt. B) to DTS	134.51 (41)	Measured at Site (length marking on fiber)
Fiber length from pt. A to splice box in P30 pole	130.46 (39.76)	AutoCAD official UG Drawing + Site measurement
Fiber length in spare duct from pt. A to pt. B	1290.14 (393.23)	

Once the data points, corresponding to the pt. A and B, were located in the temperature measurement data for all of the fibers, that is, the fibers in the main duct and those in the

spare duct, the measured temperature data for an instant, for all the fibers were plotted for the length from pt. A to pt. B as shown in Figure 4-7 and Figure 4-8.

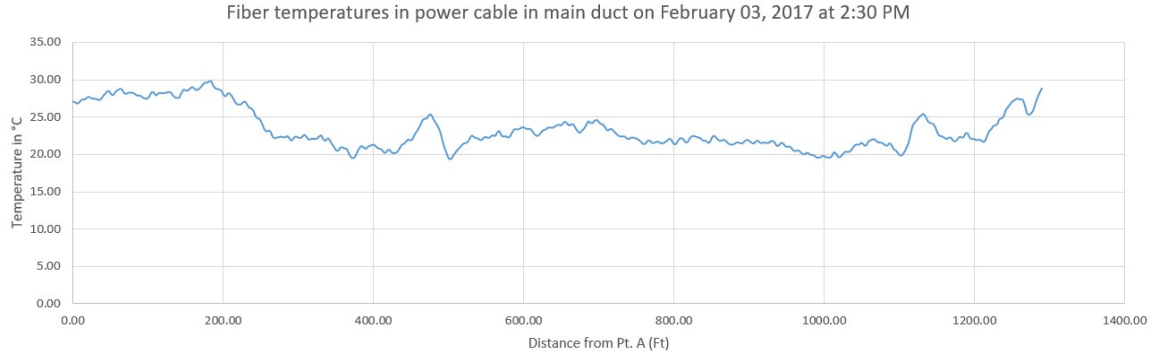


Figure 4-7 Measured temperature plot for the fiber in the main duct from pt. A to pt. B

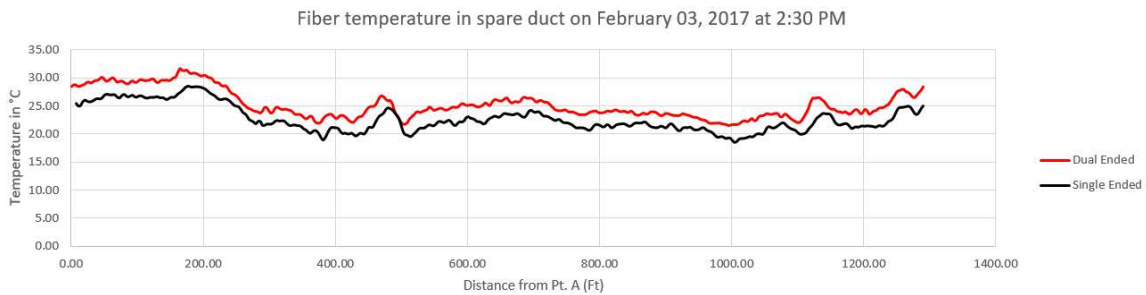


Figure 4-8 Measured temperature plot for the fibers in the spare duct. Red curve is for the dual-ended measurement and black curve is for the single-ended measurement

Figure 4-7 and Figure 4-8 show that the temperatures in all of the fibers, that is, the fiber in the main duct and the fibers in the spare duct, peaked at approximately 173 ft. from pt. A. This location is the hotspot for that instant of the measured data. It was also observed that the temperatures in the fiber with the single-ended measurement were approximately 4 °C lower than the temperatures in the fiber with the dual-ended measurement. Since, the measured data from the dual-ended measurements are more accurate (due to reduced noise in the signal) than those from the single-ended measurements, data from the dual-ended measurement in the spare duct were used to determine the hotspot location. A MATLAB

program was also written to detect the hotspot location between pt. A and pt. B for the measured data interval for all the fibers. The fiber embedded in the power cable is referred to as 'Fiber 1' and the fiber in the spare duct is referred to as 'Fiber 3' as they were connected to the channel 1 and channel 3, respectively, of the DTS. The temperature measurement data collected on February 03, 2017 at 02:30 pm were used to determine the hotspot location on the fiber in the main duct and the fiber in the spare duct on that day and plotted in Figure 4-9. The x-axis in Figure 4-9 shows the distances of hotspot locations from the pt. A and the y-axis shows the percentage of the number of samples where the hotspot occurred at the x location in the installation. The hotspot locations for the initial data measurements were observed to occur at approximately between 173 ft. and 176 ft. from the pt. A in the main duct for the conductor and at (approximately) between 171 ft. and 175 ft. from the pt. A for the spare duct fiber, as shown in Figure 4-9. These locations approximately coincide with the deepest section of the installation between pt. A and pt. B. Since heat dissipation is slower from the deeper sections of the installations due to the greater earth thermal resistance, the cable is expected to get hotter in the deeper section. It is also important to note that these measurements were taken in the winter season, when the earth's surface temperatures are low.

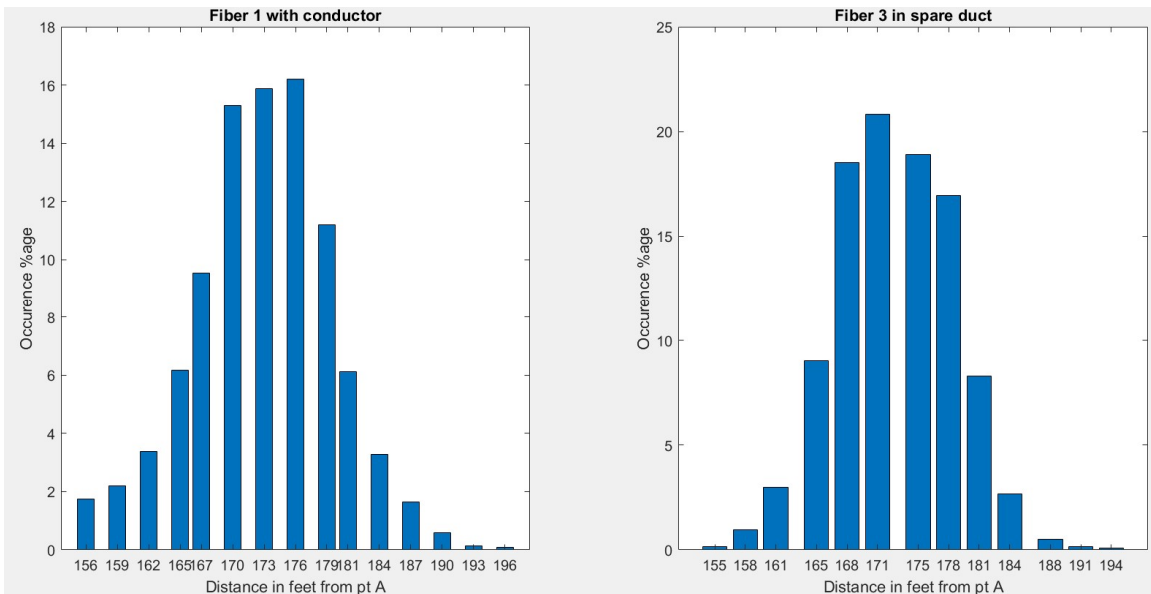


Figure 4-9 Hotspot location for power cable fiber and spare duct fiber on February 03, 2017

Once the hotspot, which lies in the part of the installation with the vertical duct bank configuration in Figure 4-6, was located for February 03, 2017, the next step was to determine the peak temperatures for the day in the main and spare ducts. The measured temperature data for both the main duct fiber and the spare duct fiber were plotted as a function of time for the hotspot location. Before the temperature measurements were made, it was expected that the spare duct would be cooler than the duct with the conductor, because there was no current carrying conductor or any other heat source in the spare duct. However, it was observed that the spare duct was hotter than the duct with the main conductor for some part of the day as shown in Figure 4-10.

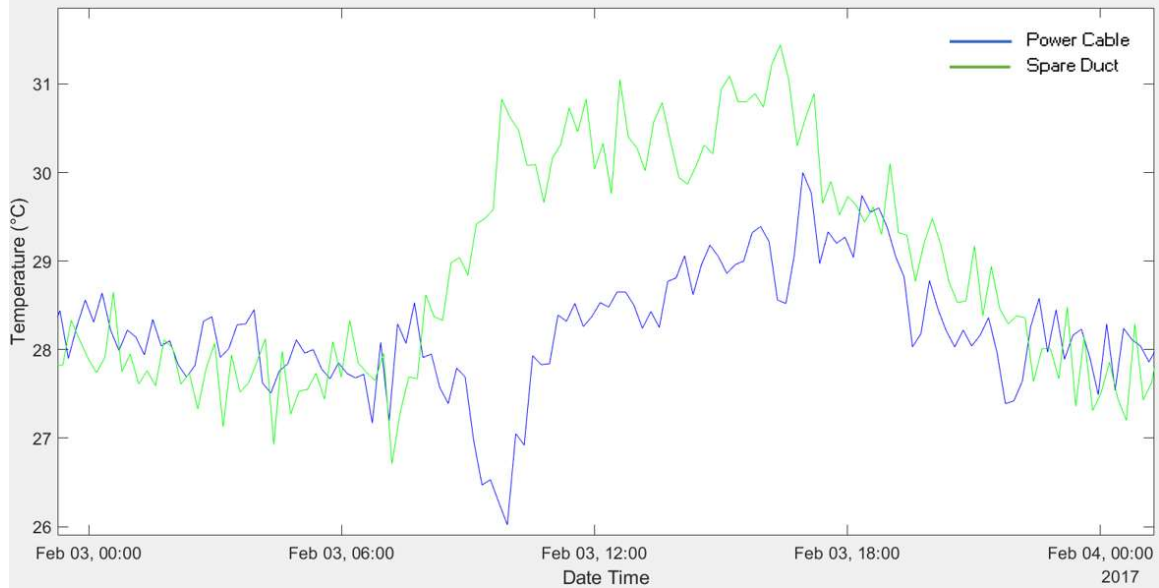


Figure 4-10 Temperature variation for fibers in main and spare duct on February 03, 2017

There were many factors that could have influenced the temperatures in the main and spare ducts in the underground installation such as other existing power lines, drain pipes, gas lines and various other factors. However, after studying the duct temperature data taken over several days, it was observed that the spare duct temperatures increased disproportionately after the sunrise and decreased gradually by evening, eventually dropping below the conductor temperature.

A theory was developed based on these observations that since the spare ducts in the underground installation were closer to the earth's surface, the higher temperature in the spare duct was attributed to the earth's heating due to the solar radiation. To verify this theory, models were developed in MATLAB and CYMCAP. The models and their results are explained in Chapter 6.

5 HOTSPOT LOCATION

5.1 Hotspot detection and seasonal shift in hotspot location

The hotspot is the location in the installed power cable which experiences the maximum thermal stress. These locations can be identified by continuously monitoring the temperature of the cable along the entire length of the installation.

Cable temperature increase are exacerbated by the occurrence of the high thermal resistance of the soil, installation depth and high thermal resistivity of the insulation of the cable. Hotspots can limit the current carrying capacity of the cable. Techniques such as use of thermal backfill, flowing thermal backfill and circulating fluid in the ducts are used to prevent the overheating of the cable and thereby preventing occurrence of the hotspots in the installation.

For this project, we have installed the fiber optics in the 69kV Brandow-Pickrell underground installation as explained in section 2.2. Real-time temperature data for the fiber embedded in the power cable and the fiber installed in the spare duct were being recorded by the DTS. A MATLAB program was written to process the data to find the hotspot in the installation for each time the measurements were recorded in the DTS.

The temperature data for the power cable in the main duct have been recorded since 2015, and are currently being recorded as of the writing of this report; however, the temperature data for the fiber in the spare duct have been (and are being) recorded since January 2017; therefore, we will be using the data from January 2017 to July 2017 to locate the hotspot in the underground installation and identify the causes for the hotspot. We will also

investigate if the hotspot location in the power cable in the main duct can be predicted from the hotspot location in the spare duct.

To determine the hotspot in the installation, we have segregated the measured temperature data by month and have located the hotspot for each month from January to July. Figure 5-1 - Figure 5-7 show the histograms of the hotspot locations for each month for both the fiber in the power cable and the fiber in the spare duct. It can be observed from the histograms that the probability is high for the hotspot location in the spare duct fiber to be nearly the same as the hotspot location for the fiber in the main duct for each month, with a maximum deviation of 5 ft.

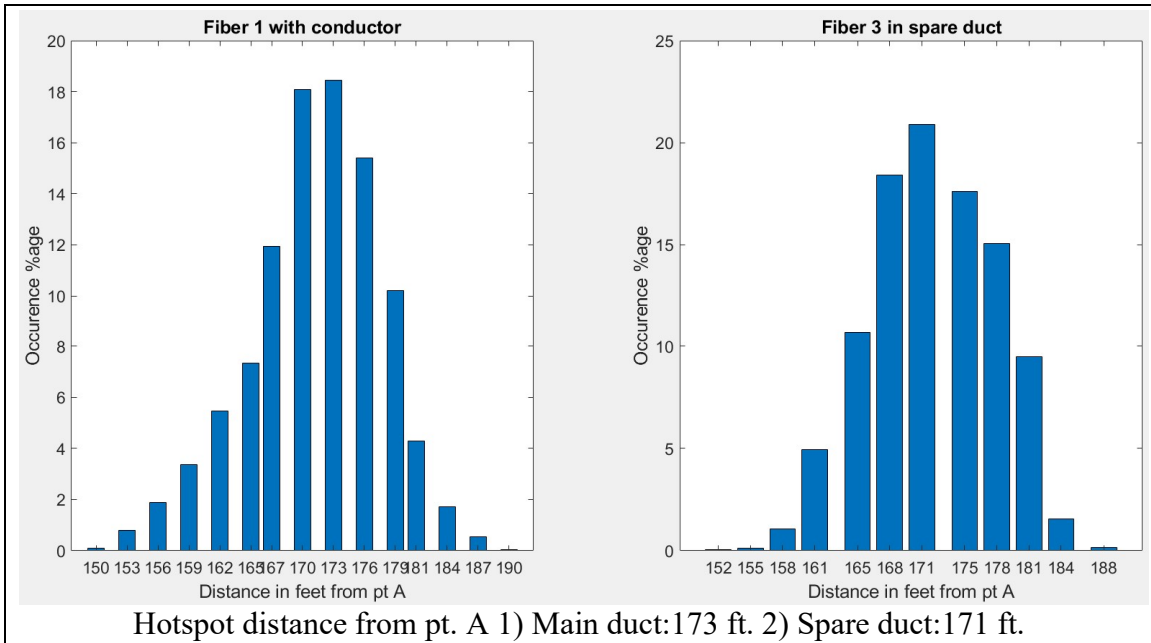


Figure 5-1 Hotspot location on the fiber in the power cable in the main duct (fiber 1) and the fiber in the spare duct (fiber 3) in January 2017

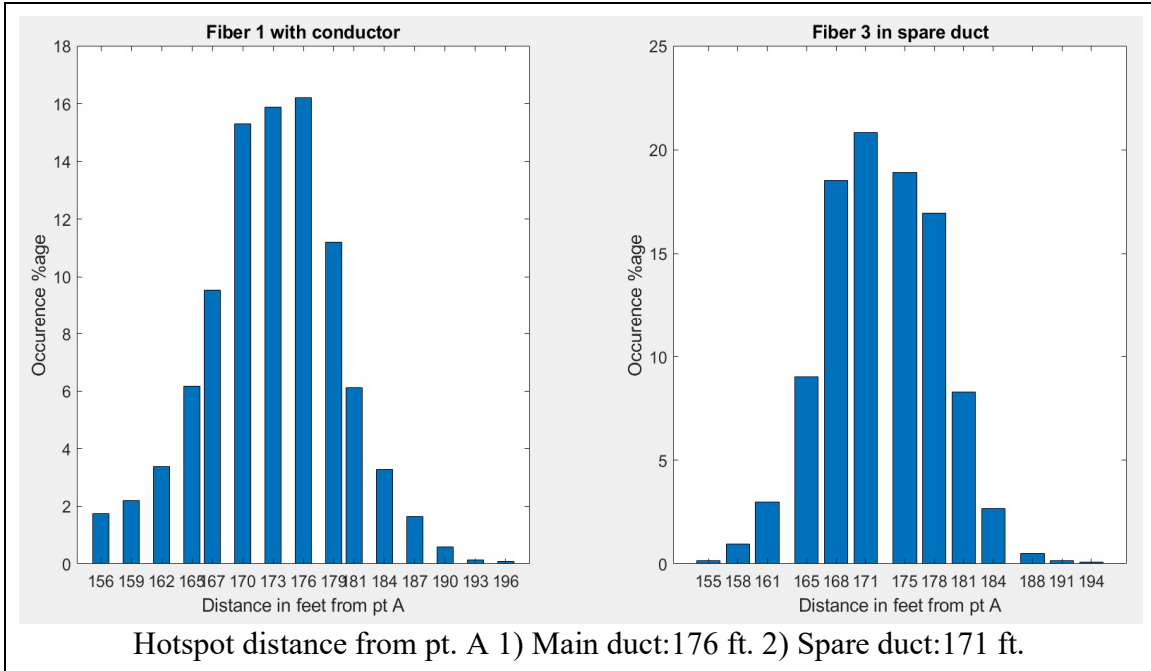


Figure 5-2 Hotspot location on the fiber in the power cable in the main duct (fiber 1) and the fiber in the spare duct (fiber 3) in February 2017

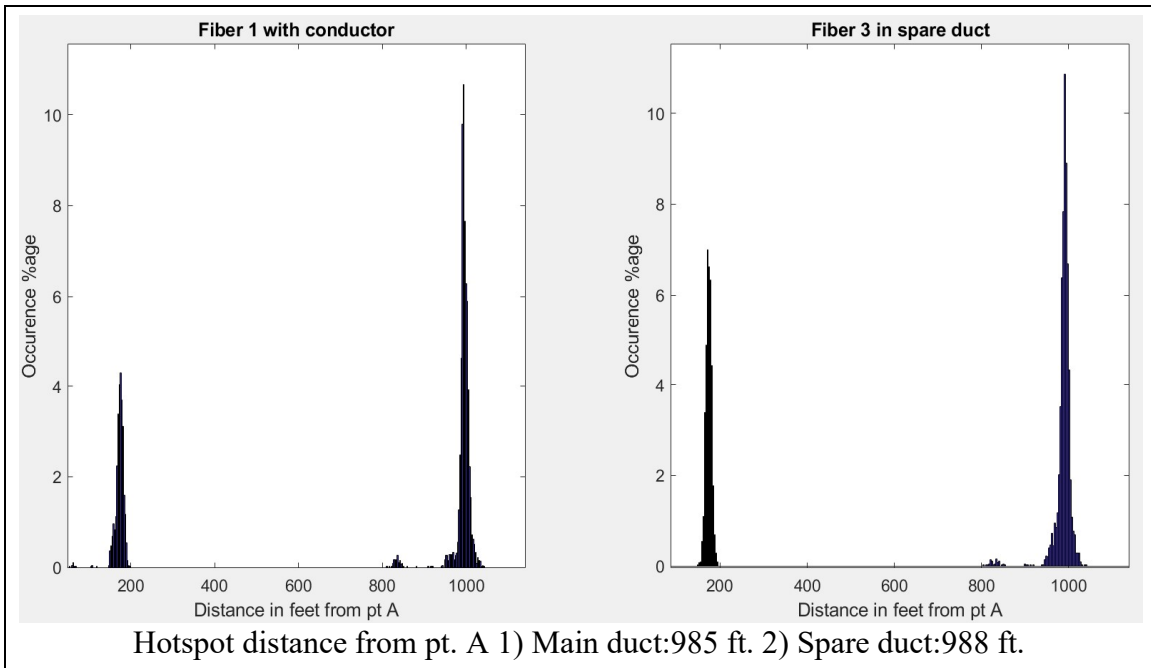


Figure 5-3 Hotspot location on the fiber in the power cable in the main duct (fiber 1) and the fiber in the spare duct (fiber 3) in March 2017

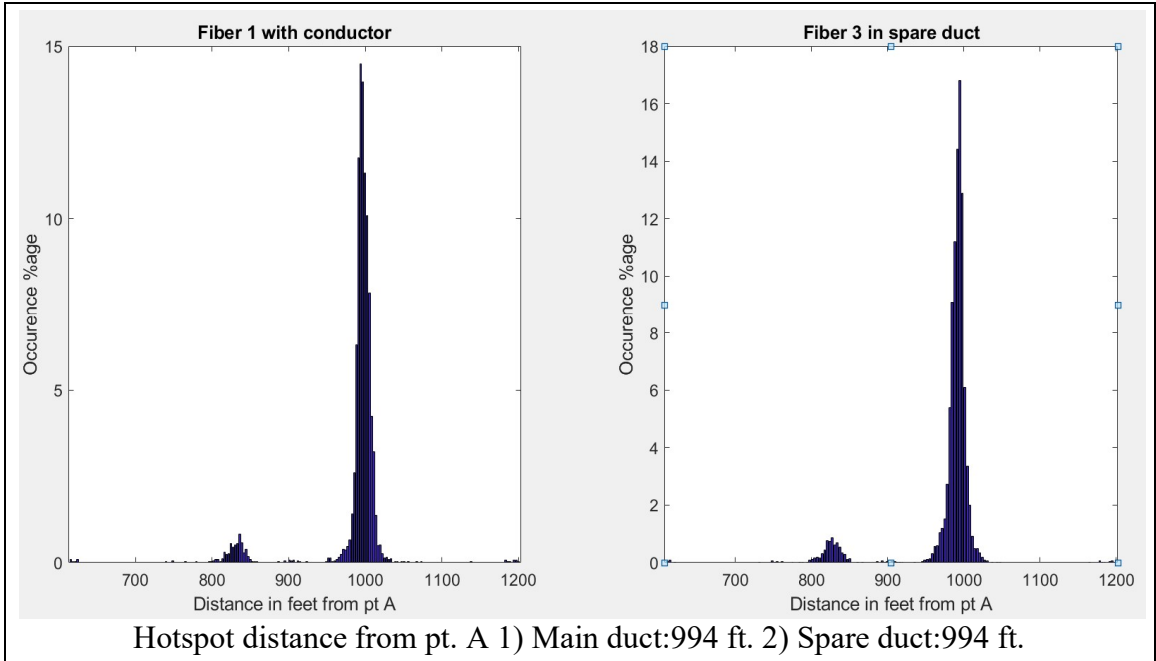


Figure 5-4 Hotspot location on the fiber in the power cable in the main duct (fiber 1) and the fiber in the spare duct (fiber 3) in April 2017

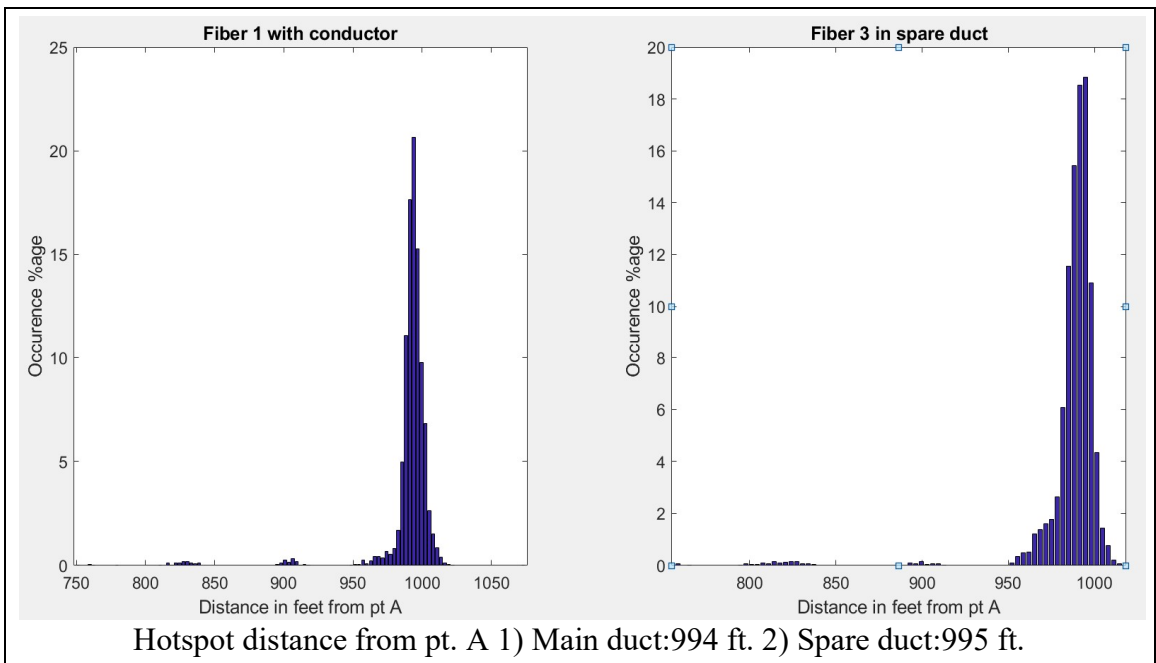


Figure 5-5 Hotspot location on the fiber in the power cable in the main duct (fiber 1) and the fiber in the spare duct (fiber 3) in May 2017

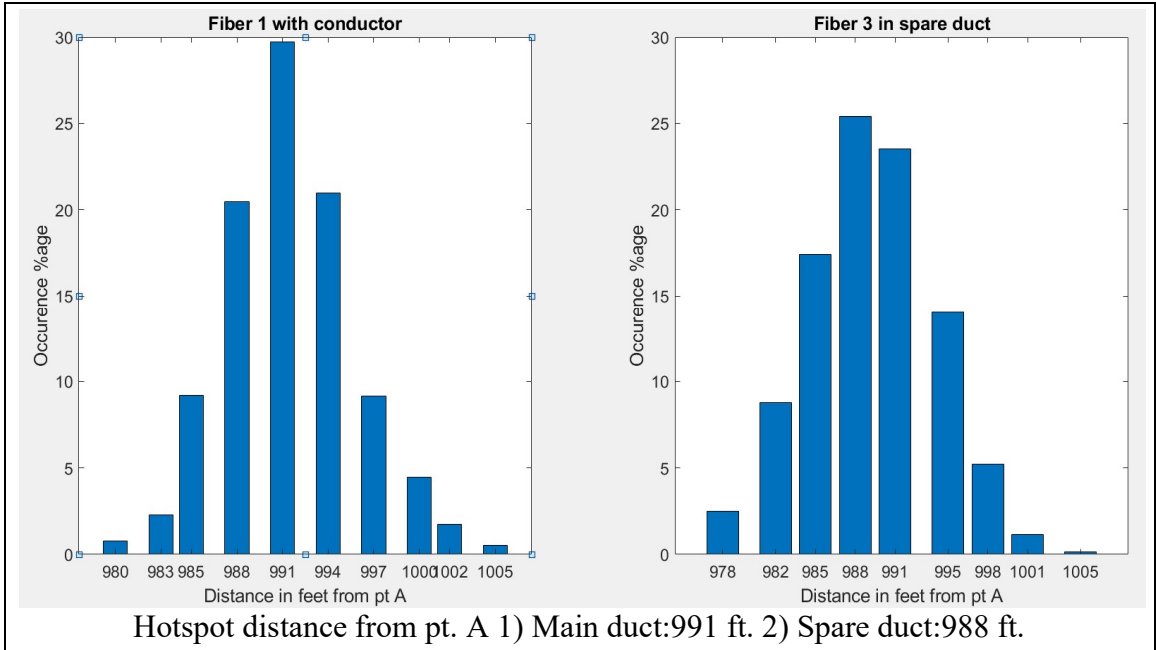


Figure 5-6 Hotspot location on the fiber in the power cable in the main duct (fiber 1) and the fiber in the spare duct (fiber 3) in June 2017

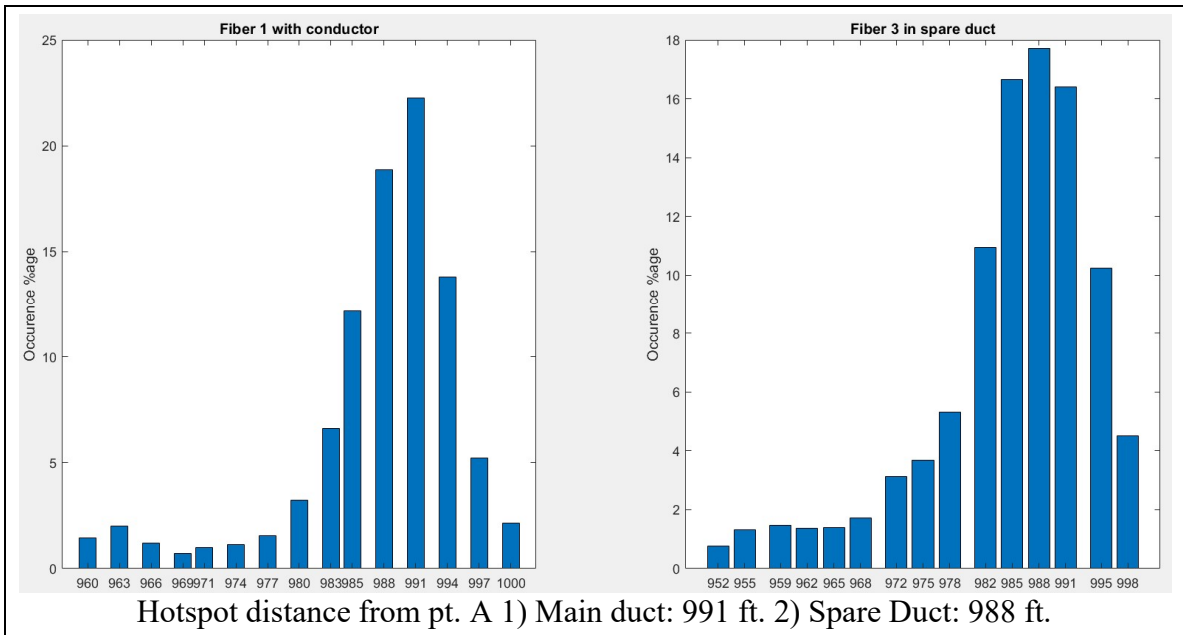


Figure 5-7 Hotspot location on the fiber in the power cable in the main duct (fiber 1) and the fiber in the spare duct (fiber 3) in July 2017

It should be noted that the hotspots for the months of January and February are at approximately 173 ft. from the pt. A. For the month of March, there were two spots which accounted for the majority of the highest measurements. These hotspots were located at approximately 173 ft. from the pt. A and at approximately 985 ft. from the pt. A. The number of hotspots occurring at 985 ft. from the pt. A were far more than at any other point in the installation in March. However, in April, the predominant hotspots were found at about 994 ft. from the pt. A, with a few hotspots at 835 ft. from the pt. A. By the month of July, all the hotspots were found at approximately 988 ft. from the pt. A.

It can be inferred from Figure 5-1 - Figure 5-7 that there are two major hotspots for this installation. The hotspot location changes from 173 ft. from the pt. A, during winter months, to 988 ft. from the pt. A, during summer months. A seasonal shift was observed for the hotspots in this installation. It is important to explore the reasons for this shift as this can help in determining, for a given installation, whether the physical location of the binding constraint on the ampacity calculation of the power cable will change with the season.

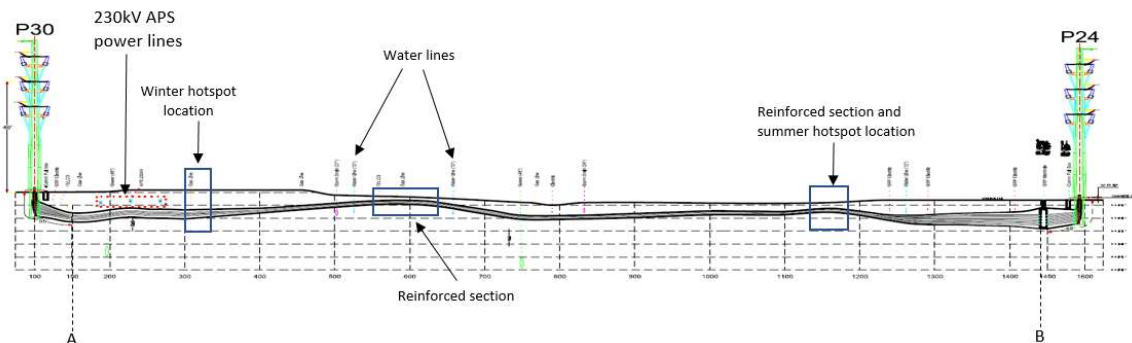


Figure 5-8 Hotspot locations on sectional layout of the Brandow-Pickrell installation

The winter hotspots were found at one of the deepest sections of the installation. This section is shown in Figure 5-8. This spot lies close to a 230kV underground APS power transmission line. Since these hotspots are near the deepest part of the installation, the thermal resistance offered by the soil is very high and heat dissipation is inefficient. The earth's thermal resistance also blocks the heat from reaching the earth's surface. This hotspot can be observed during the winter months of January, February and for a few days in March.

However, during the summer months, the hotspot observed was at one of the shallowest sections of the installation as shown in Figure 5-8. A hotspot occurs in this location because this part of the installation is very close to the earth's surface and lies at the reinforced section of the underground duct bank. This section is reinforced with steel bars and concrete to provide strength to the trench section as it lies beneath a road as shown in Figure 3-7. The thermal resistivity of the reinforced section is higher than the thermal resistivity of the backfill used elsewhere in this installation. However, being very close to the earth's surface is a double-edged sword. During winter, the lack of much overburden reduces the overall thermal resistance (of the reinforced section), which facilitates the heat dissipation from the power cable; during the summer, the shallow burial also lets the heat from road's surface to propagate into the conduit and increase the temperature of the power cables. As is well known, the road section, coated in places with tar, gets very hot on summer days, reaching temperatures (we have measured) of 160° F (70° C).

It was interesting to see that out of the two reinforced sections in the installation, as marked by blue squares in Figure 5-8, the hotspots were observed in only one of those sections.

This is because the section closer to the pt. A, which is also under the tarred road, is between two water lines which keep it cooler than any other part of the installation.

However, just knowing the hotspot location is not enough, we should also be aware of the minimum and maximum temperatures at the hotspot locations. These temperatures will be used to validate the models developed in Chapter 6. Table 5-1 below shows the minimum and maximum temperatures during each month at the hotspot locations. In the following chapter, we have tried to develop the models to predict the temperatures in the power cable in the main duct based on the temperatures in the spare duct.

Table 5-1 Monthly hotspot temperatures in different fibers in the installation

Month	Hotspot location (dist. from pt. A) (ft.)	Hotspot temperatures of fiber in power cable in main duct (Fiber 1) (°C)		Hotspot temperatures of fiber in spare duct (Fiber 3) (°C)	
		Minimum	Maximum	Minimum	Maximum
January	173	26.30	30.87	27.50	37.39
February	170	24.89	30.30	25.76	35.79
March	985	24.69	30.28	25.90	34.10
April	994	28.63	38.89	28.45	39.55
May	994	35.05	45.60	32.09	42.79
June	988	42.45	52.01	37.97	51.56
July	991	47.94	53.94	43.92	53.76

6 MODELS FOR TEMPERATURE PREDICTION

To model the temperatures of the power cable in the main duct, CYMCAP and MATLAB were used. Travis Stowers worked on the steady-state models in CYMCAP in an earlier project [5]. He showed that we need to adjust the earth's surface temperatures (ambient temperature) in CYMCAP to replicate the measured data. However, when there is a large variation in the earth's surface temperature within a 24-hour period, we must consider the earth's surface temperature time variation in our model if we hope to duplicate the measured data with the simulated results. Thus, to duplicate the thermal data measured in this project, we need to use the transient modeling capability of CYMCAP or develop a dynamic model and build a simulation using MATLAB model which accounts for the thermal behavior of the power cable and the soil. Another reason for using the transient analysis was to observe the time lag or phase shift between the peak load in the conductor and the peak temperatures in the power cable and the spare duct over a 24-hour period. These phase shifts were used as a metric to validate the simulation results from the measured data since these time lags or phase shifts (between the peak load current in the conductor and the peak temperature of the power cable jacket and between the peak temperatures of the power cable jacket and the spare duct), were also observed in the measured data over every 24-hour interval. The phase shifts will be calculated using the formula given by (6-1),

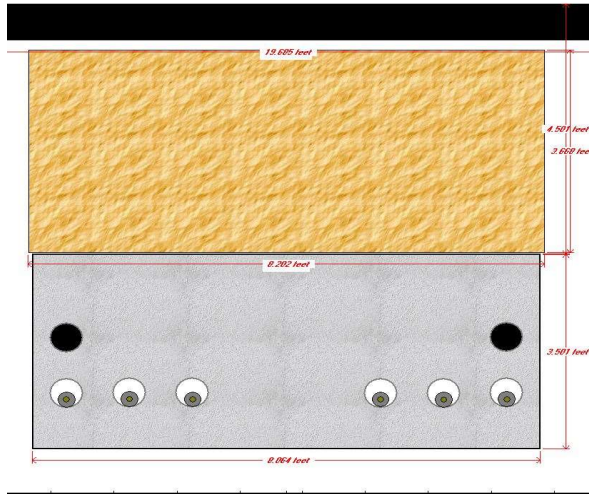
$$Phase\ shift = \frac{(Time_{Peak\ temperature} - Time_{Peak\ current})}{24} \times 360^\circ \quad (6-1)$$

Also note that the positive and negative phase shifts represent the lag and lead of the temperature peaks with respect to the peak load in the conductor, respectively. The other metric used is the maximum and minimum temperature of the power cable and the spare duct. These two metrics, that is the phase shift and temperature, will be used to validate all the models developed in this project.

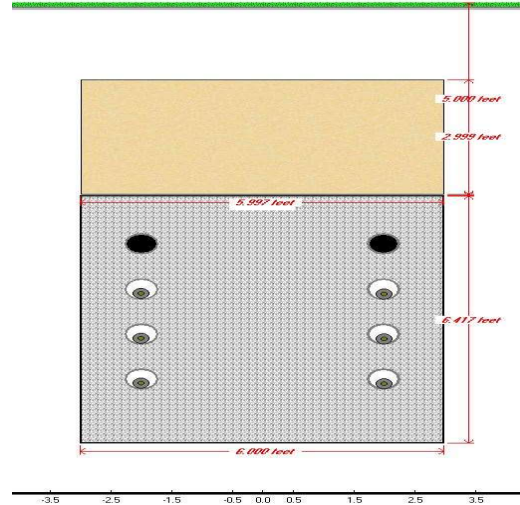
When developing simulations, two models were developed; one with the earth's surface temperature modeled as a constant and the other with a variable earth's surface temperature whose temperature profile matched the field measurements. Using the simplified model (constant earth's surface (ambient) temperature) for the installation, we developed several dynamic models (using CYMCAP and MATLAB) some of which included the capability of modeling the earth's surface temperature variation. Once the models were developed, their results and limitations were studied and validated using the measured data. The model development and simulation results are discussed next.

6.1 The CYMCAP model

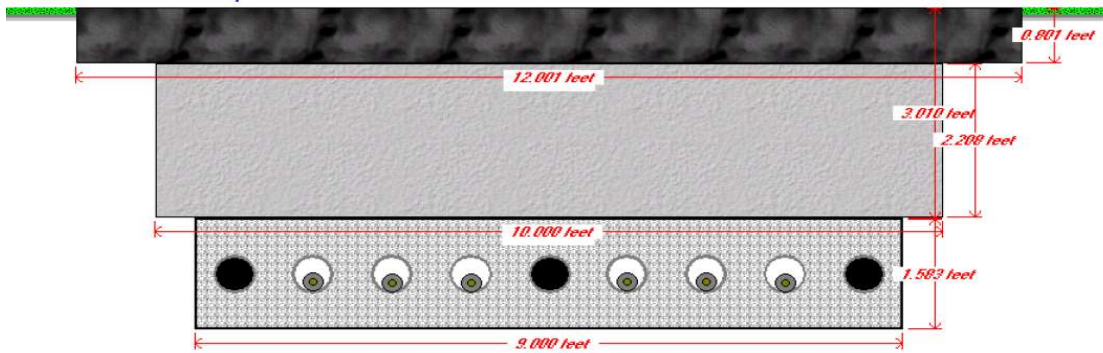
CYMCAP is a software application jointly developed by CYME International, Inc., Ontario Hydro (Hydro One) and McMaster University to study the cable ampacity and temperature-rise calculations for the power cables. For the underground installations, CYMCAP allows different duct bank geometry, power cable thermal models, cable current, heat sources in the installation and thermal models of various thermal backfills to be modeled. Figure 6-1 a-b and c show the CYMCAP models for the horizontal, vertical and reinforced section duct bank configurations encountered in this project.



a. Horizontal Configuration – CYMCAP model



b. Vertical Configuration – CYMCAP model



c. Reinforced section – CYMCAP model

Figure 6-1 CYMCAP models for the horizontal, vertical and reinforced section configuration

6.1.1 Constant Earth's Surface Temperature (CEST) model for CYMCAP

The CEST model is the simplified model developed to verify the MATLAB simulation without the earth's surface temperature variation. For this project, we are interested in predicting the temperatures in the main duct from the temperatures in the spare duct. The Brandow-Pickrell underground installation consists of the thermal backfill materials with the thermal resistivity ranging from 0.9 °C-m/W to 1.33 °C-m/W. Since the thermal

resistivity does not vary much along the installation, we have developed all the models with homogenous soil of thermal resistivity $1^{\circ}\text{C}\cdot\text{m}/\text{W}$.

It is understood that an object closer to the heat source will absorb more heat than if the same object is farther way from the heat source. Therefore, while modeling, we have only considered the conductor in the main duct which is closest to the spare duct since the conductor closest to the spare duct will have the most influence on the heating of the spare duct. The models shown in Figure 6-1 are simplified to Figure 6-2.

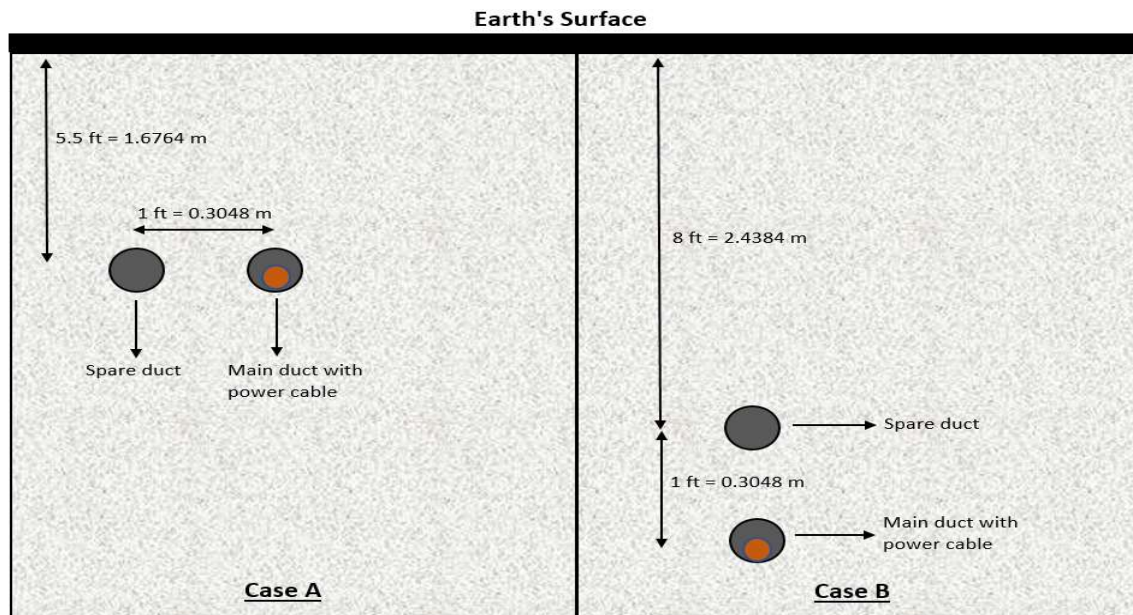


Figure 6-2 Simplified configurations for the horizontal, vertical and reinforced sections of the duct bank

Case A in Figure 6-2 represents the case for the reinforced section of the duct banks where spare duct is at the same depth as the power cable main duct whereas Case B represents the case for the sections of the duct bank with the horizontal and vertical configurations.

To simulate the temperatures of the spare duct, a power cable, with the same dimensions as the power cable in the main duct, was modeled in the spare duct. This was done to avoid the CYMCAP limitation, as CYMCAP cannot simulate the temperatures in an empty spare duct. CYMCAP models for Case A and Case B with a power cable in the spare duct is shown in Figure 6-3 a-b respectively.

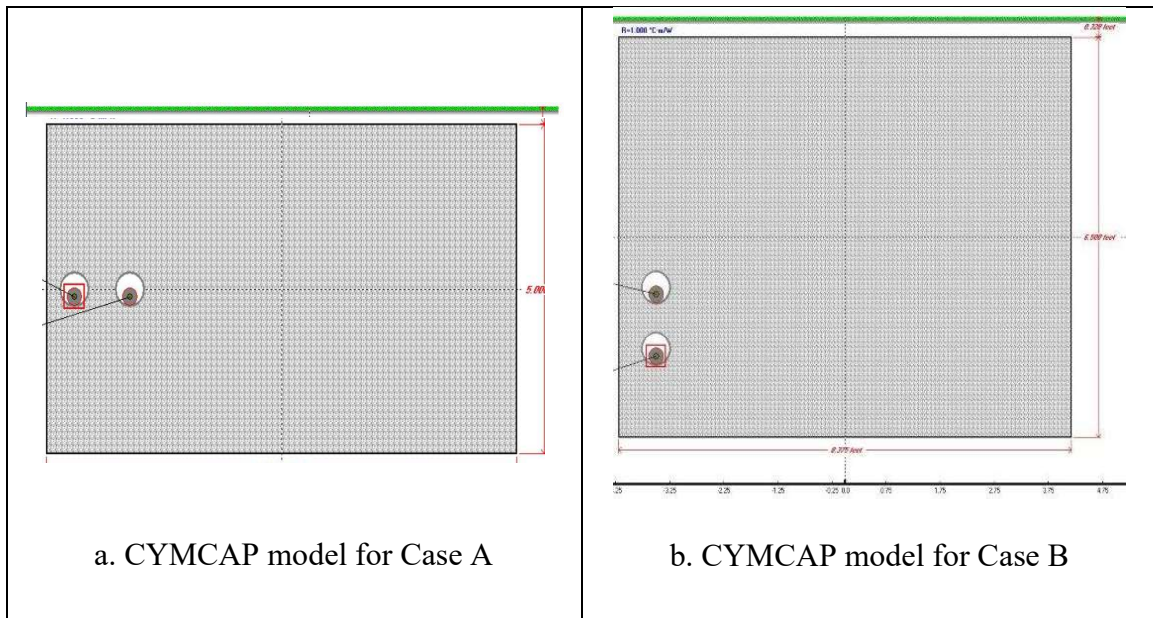


Figure 6-3 Modified CYMCAP model for the duct bank configurations

For the CEST model (constant earth's surface temperature at 20° C), the model was simulated for Case B, as most of the installation has a horizontal or vertical configuration. These models were built with the power cable in the main duct carrying measured power and with the same power cable in the spare duct but with this cable carrying one Ampere (A) of steady-state current flowing through it. Load in the conductor was modeled as shown in Figure 6-4.

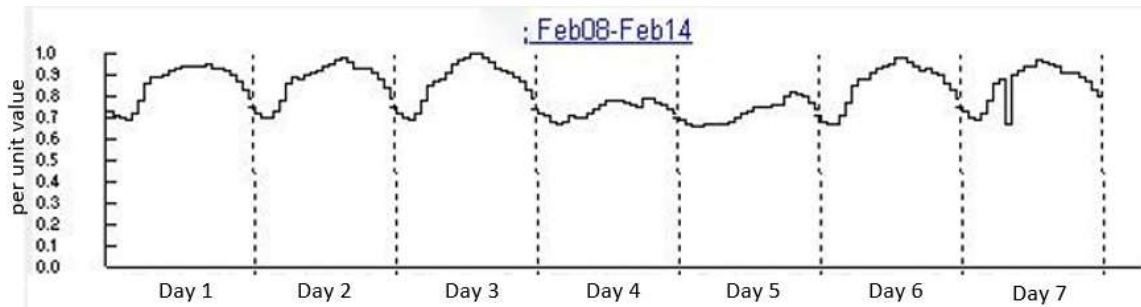


Figure 6-4 Power cable load as modeled in CYMCAP

Each portion in Figure 6-4 represents a 24-hour (one day) interval. Since, the CYMCAP only allows a maximum of seven days of input data for a simulation, the load current data for seven days obtained from the SRP's energy management system (EMS) were used as input for a seven-day CYMCAP simulation. From the EMS data, it was found that the conductor current varied between 245 A to 160 A for the seven-day interval used in the simulation. The load was modeled using the per-unit values in CYMCAP. The base value was taken as the maximum conductor current of 245 A. This base value is used for two things. First, this current is treated by the CYMCAP as the steady-state current for the conductor before the start of the simulation (time < 0) to initialize the conditions before the start of a transient analysis. Second, this current value was used as a base value to calculate the per unit values of the load current. The maximum load current was selected for the base value as CYMCAP does not allow per-unit value greater than one. The conductor current was modeled with the EMS load current data, which vaguely resembled a sinusoid (with a dc offset) with a time period of 24 hours and with the load current value varying from 160 A to 245 A. This load current peaked at approximately 3 PM every day for the period of simulation. To simulate the spare duct, the load in the spare-duct power cable was dropped to zero Amperes at the start of the simulation (for time ≥ 0) from 1 A (for time < 0), since

we were trying to replicate the Brandow-Pickrell installation where there is no power cable in the spare duct. Dropping the spare power cable load current to zero was important since it eliminated the additional heat generation from the power cable in the spare duct. The conductor load current and the constant earth's surface (ambient) temperature were used as inputs for the model. The base model was simulated for a seven-day period and the results were compared with the measured data.

6.1.2 Observations

Figure 6-5 and Figure 6-6 give the plots for the seven days of CYMCAP simulation and the measured data, respectively. Recall that we are using the phase shift and the temperature values as metrics for the validation of our model. Therefore, from Figure 6-5, it can be seen that the temperature in the power cable jacket varied between 21.1 °C to 21.9 °C and peaked at approximately 5:30 PM each day, which is 2.5 hours after the peak load in the conductor. There is a lag between the simulated peak power cable jacket temperature and the peak load in the conductor of about 37.5 degrees. Whereas in Figure 6-6, which gives the plot for the measured data, the temperature in the power cable jacket varied from 26.4 °C to 29.8 °C and peaked at approximately 3 PM every day, which corresponds to a lag of 0° from the peak conductor load.

The spare cable temperatures dropped from 20.7 °C to 20.6 °C and remained almost constant for the simulation time period of 168 hours (seven days) in the CYMCAP simulation. The spare cable was observed to be colder than the main power cable as the power cable was the only heat source in the simulated model. However, in the measured

data, the spare cable temperatures were higher than the power cable temperatures for some part of the day and varied from 26.8 °C - 35 °C and peaked at approximately 1:30 PM every day, 1.5 hours before the peak load or with a lead of 22.5°. Since major deviations were observed in the measured and simulated data, it was decided to model the earth's surface temperature variation in CYMCAP to try to replicate the measured data.

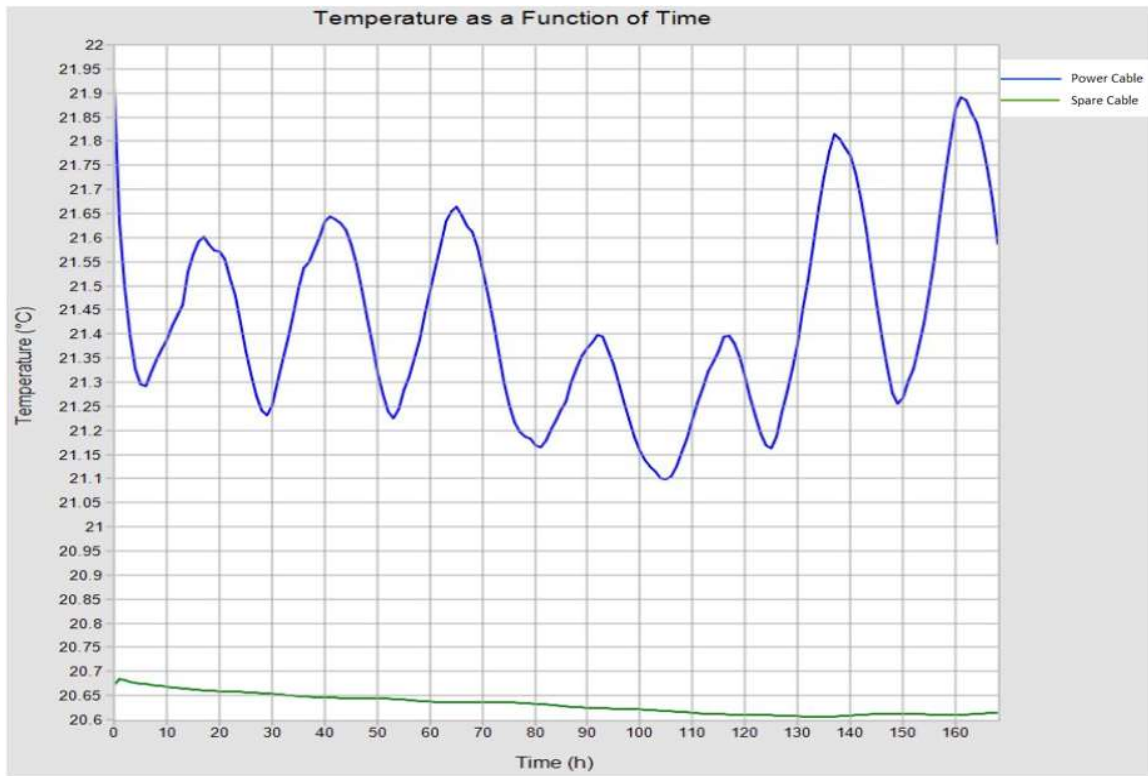


Figure 6-5 Simulation results for the CYMCAP CEST model

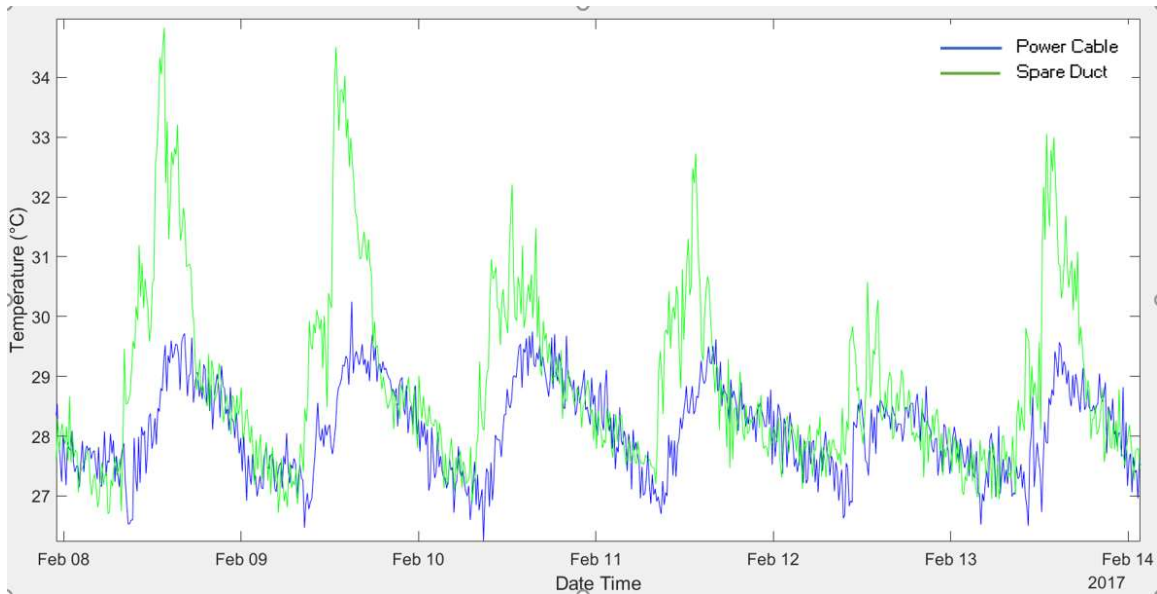


Figure 6-6 Measured data for a seven-day period from February 08 - 14, 2017

6.1.3 Time varying earth's surface temperature (TVEST) model for CYMCAP

Because the model predictions obtained from the CYMCAP model with a constant earth-surface temperature were unsatisfactory, we wanted to develop a CYMCAP model that accounts for the earth-surface temperature diurnal variation; however, CYMCAP does not have the capability of modeling a variable earth's surface temperature. To solve this problem, it was decided to model the earth's surface temperature variation on another point of the isothermal surface which passes very close to the earth's surface. (Recall from (2-12) that an isotherm exists that touches the earth's surface and at any point on this isotherm the temperature will be equal to the earth's surface temperature.) Since we could not model the heat source vertically above the power cable (and because we had to maintain the depth of the installation and keep the distance of the heat source from the power cable equal to the depth of the installation), it was proposed to rotate the duct bank model by 90° and place the heat source at a distance equal to the depth of the installation. This way, the depth

of the model was also kept equal to the depth of the installation. The temperature variations in the heat source were modeled using the earth's surface temperatures measured for a 'typical' day. These temperatures were then replicated for seven days (period of simulation), which were then used as input for the heat source temperature variations. The new model with the time varying surface-temperature heat source is shown in Figure 6-7. The red circle is the heat source, the cable closer to the heat source is the non-current carrying cable located in the spare conduit and the other cable is the main power cable. Ambient earth temperature was kept at 20 °C and the thermal resistivity of the homogenous soil remained 1 °C-m/W. Modeling of this heat source for the simulation is explained in Section 6.1.4.

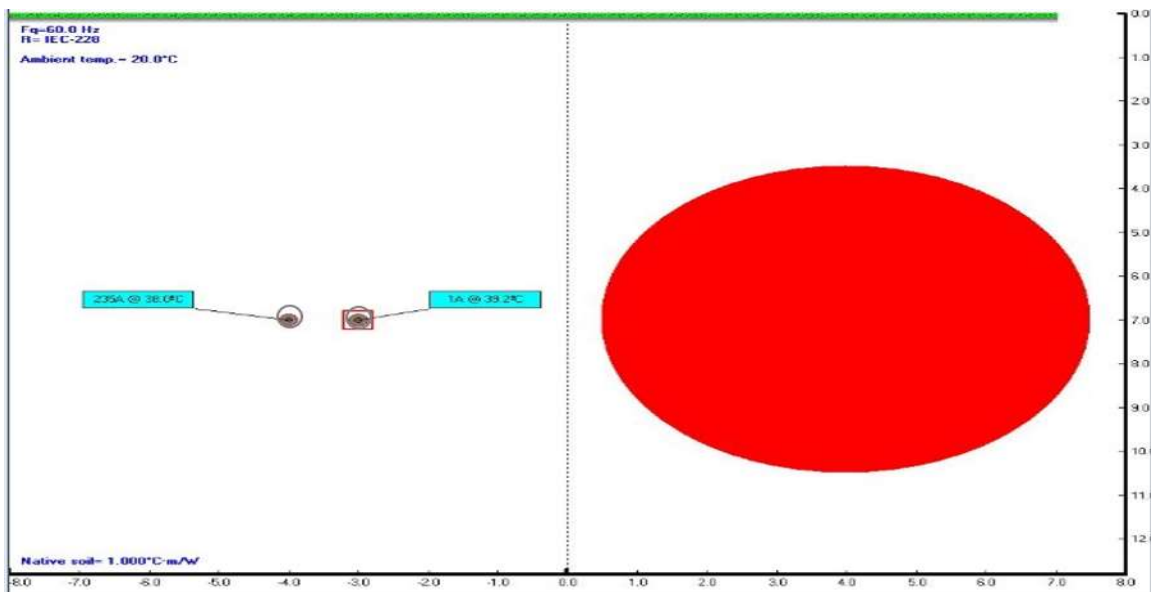


Figure 6-7 CYMCAP model with the heat source

6.1.4 Modeling earth's surface temperature in CYMCAP

CYMCAP treats the earth's surface as an isothermal surface and its temperature (ambient temperature) can be set as "Ambient Temperature" as shown in Figure 6-8. Ambient

temperature in Figure 6-8 represents the earth's temperature without heat from any underground sources.

General data	
Ambient Temperature, °C	20.0
Native soil thermal resistivity, °C-m/W	1.000

Layer name:	Layer caption:
Backfill	Soil

Backfill data	
Height, feet	8.120
Width, feet	15.499
X of horizontal centre of backfill, feet	0.000
Y of vertical centre of backfill, feet	4.059
Backfill thermal resistivity, °C-m/W	1.200
<input checked="" type="checkbox"/> Same as native soil resistivity	

Figure 6-8 Setup for the earth's ambient temperature and Native soil resistivity

As explained in Section 2.4, the isothermal surfaces for the buried conductor are in the shape of concentric cylinders around the power cable with increasing radii. Therefore, for an isothermal surface which touches the earth surface, the temperature at any point on the isothermal surface will be equal to the earth's surface. Using this concept, a heat source representing the earth surface can be placed anywhere on the circular cross-section of the isothermal surface that touches the earth's surface, to replicate the earth's surface temperature behavior. Therefore, a constant-temperature heat source was modeled in the duct bank at a distance from the conductor equal to the depth of the conductor installation from the earth's surface as shown in Figure 6-7. CYMCAP only allows a cylindrical heat source. The modeling parameters are set as shown in Figure 6-9. A large diameter (large

compared to the duct diameter) was selected for the heat source to model the flat earth's surface. The temperature setpoint for the heat source was the maximum temperature for the heat source surface. CYMCAP treats the setpoint temperature as the temperature of the heat source before the start of the simulation (at time < 0) to initialize the temperature of the heat source for the transient simulation. The measured earth's surface temperature data was used to model the heat source temperature variation after the start of the simulation (at time > 0). Since the per-unit values cannot be set to be greater than one per-unit in CYMCAP, the highest earth's surface temperature (measured) for the day, is chosen as the temperature setpoint value for the heat source to effectively model the earth's surface temperature throughout a day.

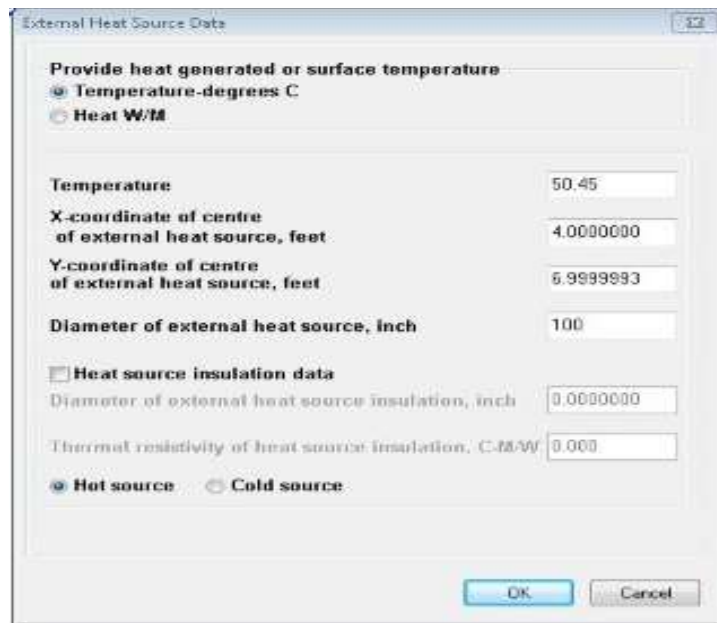


Figure 6-9 Heat source modeling parameters in CYMCAP

To model the temperature variation in this heat source, the earth's surface temperatures were measured using an infrared camera. The measurement samples were recorded every

few meters along the installation at two-hour intervals. The earth's surface temperature near the hotspot varied between 15 °C to 50 °C on March 10, 2017 and peaked at 2:20 PM in the afternoon. The measured temperature samples are shown in Figure 6-10 and these temperature samples were plotted using a curve fitting algorithm in the Microsoft Excel spreadsheet to generate a plot for the period of measurement as shown in Figure 6-11.

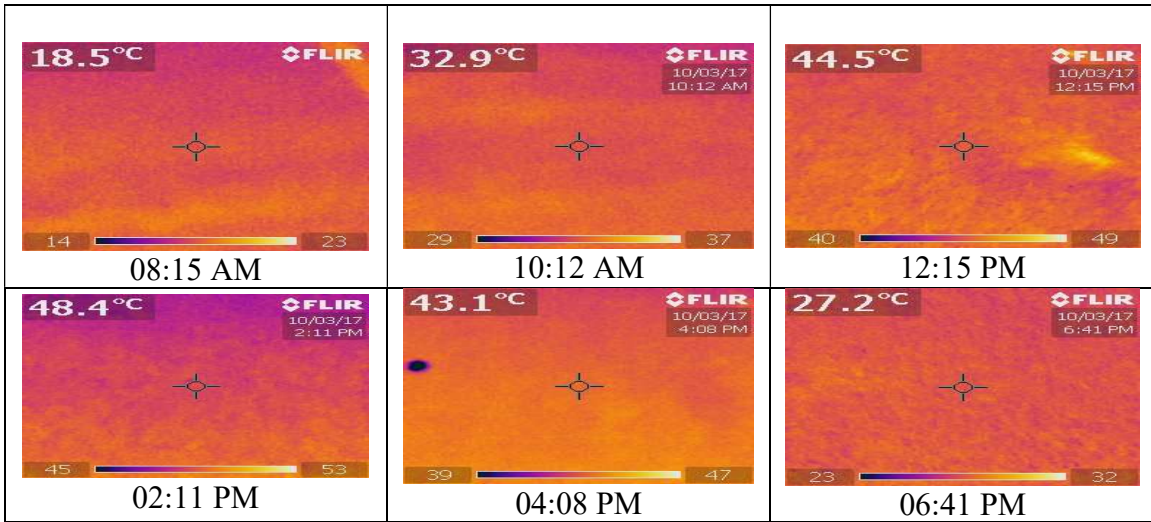


Figure 6-10 Temperature samples for various times of the day at the hotspot location on March 10, 2017

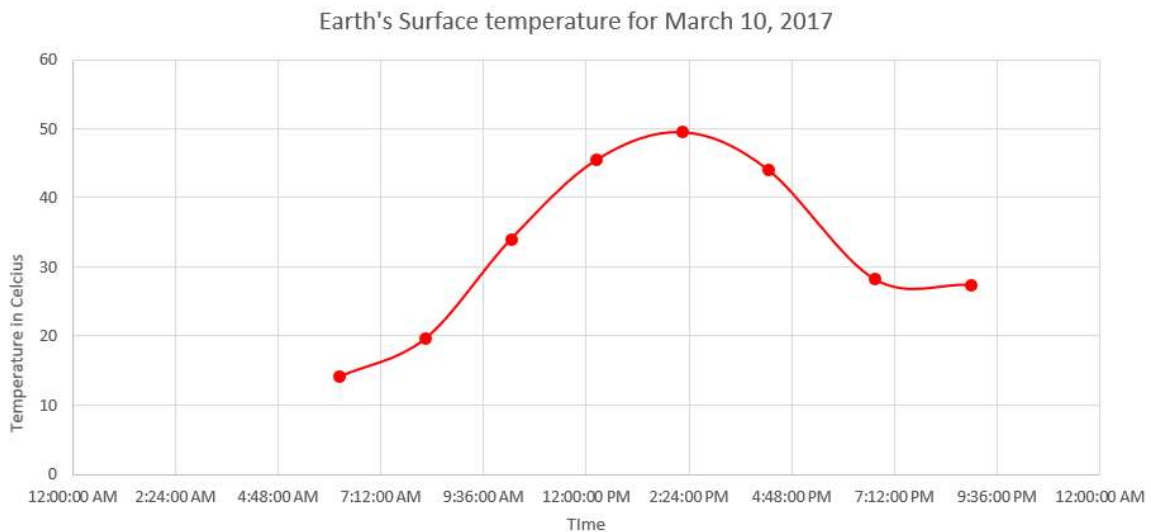


Figure 6-11 Temperature plot for the earth's surface temperature at the hotspot location on March 10, 2017

The temperature variations in the heat source were modeled using the measured earth's surface temperatures, as shown in Figure 6-10. This temperature was replicated for each day, for the seven days of the simulation period.

6.1.5 Simulation and Results

The load current in the main power cable was as shown in Figure 6-12 for March 08-14, 2017. The rms load current varied between 155 A and 287 A over the period of the simulation and peaked at approximately 3 PM every day. This load current vaguely resembled a sinusoid with a period of 24 hours. The current base value chosen for calculating the per unit values of the load current was 287 A (i.e., the maximum load current during the simulation interval). The load current data was taken from the Energy Management System (EMS) at SRP. CYMCAP has a maximum input load-data length of seven days for any simulation. Therefore, the maximum model simulation interval is limited to 168 hours as shown in Figure 6-12.

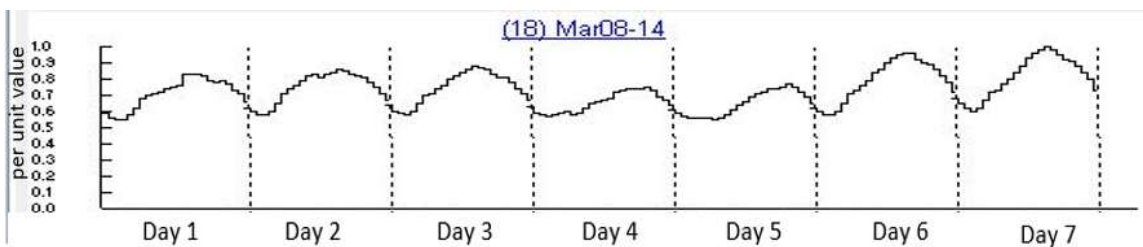


Figure 6-12 Current magnitude in the power cable in the main duct from March 08-14, 2017

The load current data and the temperature variations in the heat source were used as inputs to the model developed and the model was simulated for a seven-day period. The results from the model are shown below in Figure 6-13. The blue curve indicates the temperature

in the main power cable and the green curve indicates the temperature in the spare power cable.

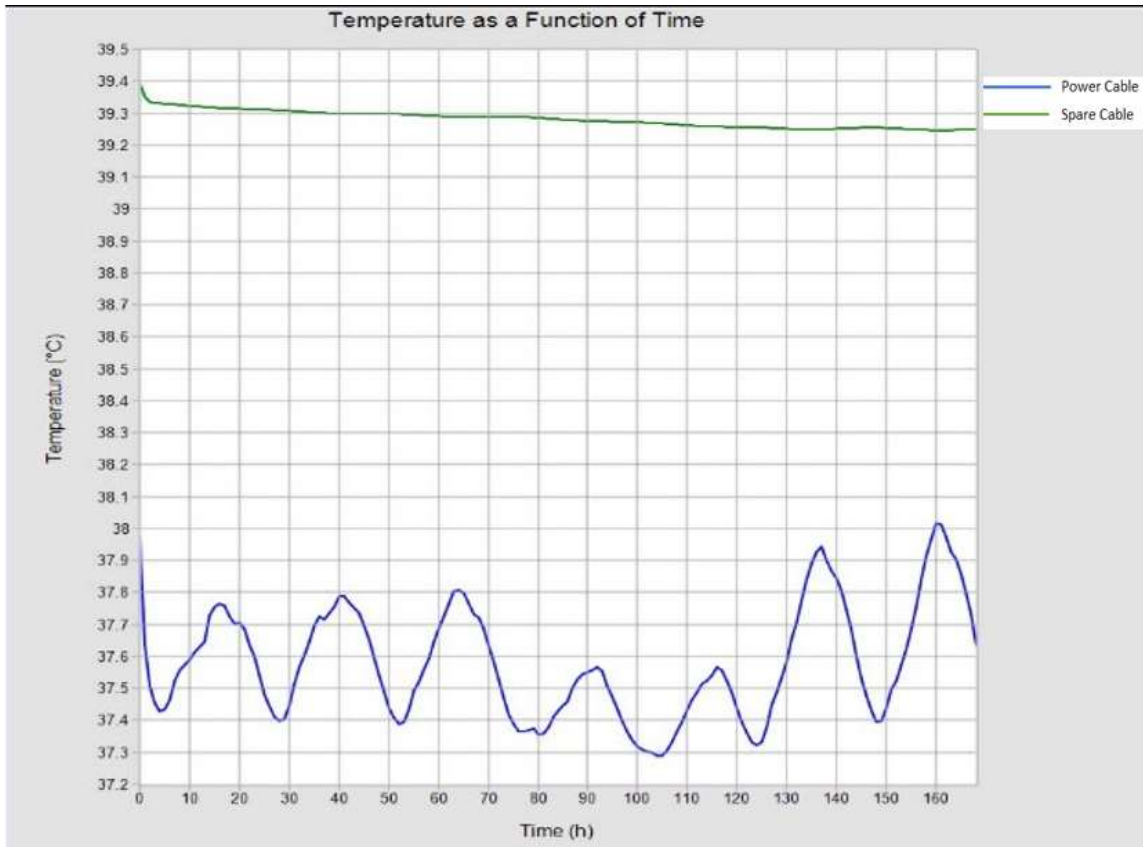


Figure 6-13 Simulation results for the temperatures in the power cable and spare cable with the earth's surface temperature modeled as a heat source

By introducing a time-varying heat source that matched the earth's surface temperature, we could see an increase in the temperature of both the spare duct and the main power cable for the entire simulation interval shown in Figure 6-13. This is what was expected from the model. However, it was also observed that, although the temperatures in the main power cable and the spare cable increased, the temperatures in the main and the spare power cable did not show any transient response due to the temperature variations in the heat

source (representing the earth's surface temperature) which was not acceptable as we could observe the transient response in the measured data.

The peak temperature in the power cable jacket was still lagging the peak load in the conductor by 3 hours or about 45° . This was not acceptable because there was almost no phase lag observed between the peak load current in the conductor and the peak temperature in the power cable in the measured data. Temperatures simulated for the spare power cable jacket were constant at 39.25°C after an initial drop. The initial temperature drop in the spare power cable was due to the change in the load current from 1 A to 0 A.

Figure 6-14 shows the measured temperature data for the period from March 08-14, 2017. The behavior of the measured main and the spare duct temperatures was entirely different from what was observed through the CYMCAP models. Simulation results are shown in Table 6-1.

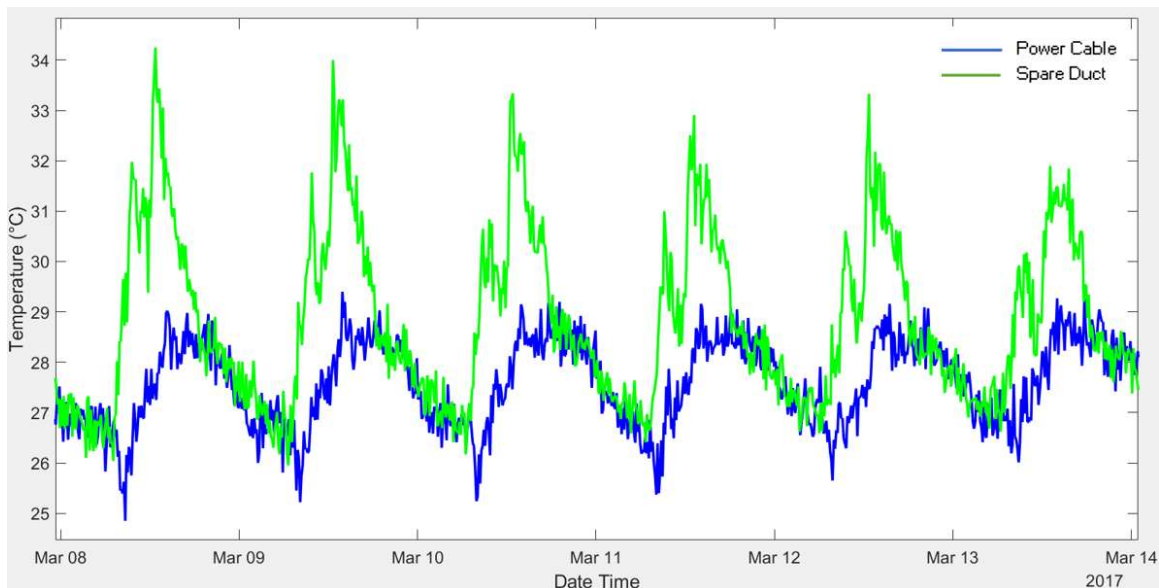


Figure 6-14 Measured temperature for the main power cable and spare duct from March 08-14, 2017

Table 6-1 Comparison between TVEST model simulation results and measured data

	Simulation results for TVEST model	Measured values
Power cable maximum temperature (°C)	38.1	29.3
Spare cable maximum temperature (°C)	39.3	34.3
Approximate time at which power cable temperature peaks	5:00 PM	3:00 PM
Approximate time at which spare cable temperature peaks	NA	12:45 PM

The deviation in the CYMCAP simulation results from the measured data was due in part because no transient effect of the temperature variations in the heat source was visible on the spare and the main power cable temperatures in CYMCAP. Since we were trying to replicate the measured data where a transient response due to the earth's surface temperature variations was observed, it was important to observe the effect of the heat source (modeling the earth's surface temperature) on the spare duct's temperature.

To observe the transient effects, it was proposed to move the spare power cable closer to the heat source, namely one foot from the heat source to see if a transient response could be observed in the CYMCAP model. Figure 6-15 shows the results for the CYMCAP simulation for this new geometry. The spare cable temperature is shown in 'blue' and the main power cable temperature is shown in 'green' in Figure 6-15. All of the other parameters such as the depth of the installation, the load current in the conductor and the resistivity of the soil were kept the same as in the earlier simulation.

As can be observed from the Figure 6-15, even after keeping the spare power cable at one foot from the heat source, the transient response observed for the spare power cable temperature did not match anything seen in the field measurements. There was a vague sinusoidal response, with a period of 24 hours, observed in the spare duct temperatures in the measured data in Figure 6-14, however this effect was not seen in the CYMCAP simulation results. Since we were not getting expected results from the introduction of the heat source in the CYMCAP model, the other case, Case A, was not simulated and thus, it was decided to proceed with the MATLAB model as explained in the following section.

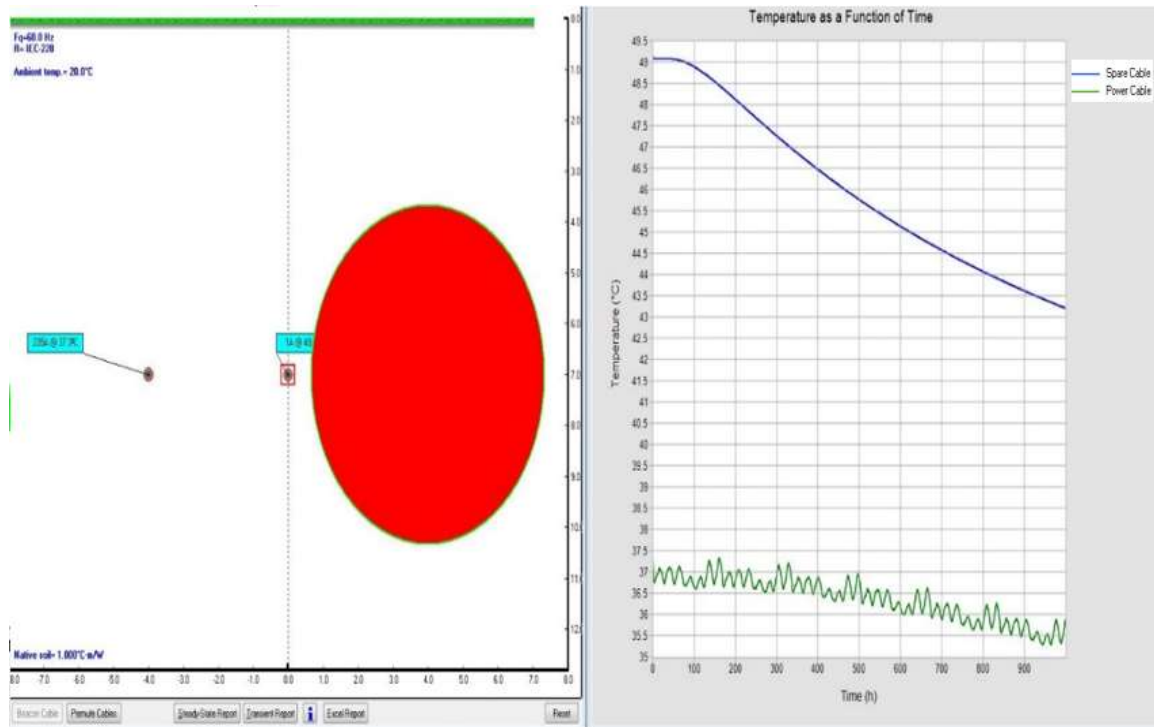


Figure 6-15 CYMCAP model with the spare cable at a distance of 1 foot from the earth's surface modeled as a heat source.

6.2 MATLAB model

The CYMCAP results showed a large deviation from the measured data and, since we were not able to model the earth's surface temperature accurately in CYMCAP, it was decided that we use other software to develop a model for the temperature predictions. Recall sections 2.4-2.6, in which it was shown how to develop an equivalent RC circuit thermal model for a buried power cable. Therefore, it was decided to use MATLAB Simulink to simulate the RC circuit for both the cases shown in Figure 6-2. With MATLAB, we could also include the earth's surface temperature variation into the RC circuit using superposition, which was an advantage since the heat source model developed in CYMCAP was not very effective in predicting the temperatures.

6.2.1 Development of Ladder Network for the Cable

Recall that in section 2.5, the theory which developed the RC-equivalent ladder network for representing the thermal response of a buried cable was presented. Figure 6-16 shows the two-loop ladder network of the conductor introduced by [8]. The current source on the left end represents the heat generated in the conductor with T_A and T_B as the thermal resistances of the layers between the conductor and the insulation screen and between the insulation screen and the jacket, respectively. Similarly, Q_A and Q_B are the combined thermal capacitances of various insulation layers of the power cable. The heat flows from the conductor into the soil and the temperature decreases as we move away from the power cable until the temperature reaches a (constant) earth's ambient temperature, represented by T_{amb} in Figure 6-16. The soil thermal resistance is denoted by T_4 . The heat generated in

the conductor is denoted by W_C and the dielectric losses in the power cable are represented by W_S . Equation (2-14) will be used to determine the power cable thermal resistances.

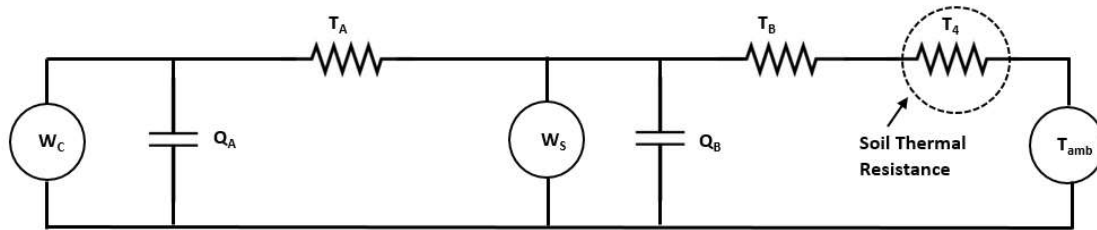


Figure 6-16 Reduced two-loop ladder circuit for power cable

Table 6-2 below shows the required data for calculating the thermal resistance and capacitance.

Table 6-2 Cable data for ladder network.

Quantity	Units	Values	Source
Radius of conductor (r_c)	m	0.0170	SRP cable drawings
Radius of insulation (r_i)	m	0.0365	SRP cable drawings
Radius of metallic sheath (r_s)	m	0.0398	SRP cable drawings
Radius of jacket (r_j)	m	0.0422	SRP cable drawings
Thermal resistivity of insulation screen (ρ_i)	$^{\circ}\text{C}\cdot\text{m}/\text{W}$	1.7596	[12]
Thermal resistivity of XLPE (ρ_j)	$^{\circ}\text{C}\cdot\text{m}/\text{W}$	4.6554	[12]
Volumetric heat capacity of Cu (c_{cu})	$\text{J}/\text{m}^3\cdot^{\circ}\text{C}$	3.45×10^6	[12]
Volumetric heat capacity of insulation (c_i)	$\text{J}/\text{m}^3\cdot^{\circ}\text{C}$	2×10^6	[12]
Insulation loss factor (λ_l)	%	9	[8]
Resistance of Cu (R)	Ω/m	1.85×10^{-5}	[13]

Thermal resistance, T_A , in the two-loop ladder circuit is equivalent to the thermal resistance between the insulation screen and the conductor and is given by (6-2),

$$T_A = \frac{\rho_i}{2\pi} \ln \frac{r_i}{r_c} = 0.214 \text{ }^\circ\text{C} - m/W \quad (6-2)$$

To calculate the value of Q_A , Van Wormer introduced a factor p which is used to reallocate the thermal capacitance of the outer cable layer to the inner layer for the ladder network [8],

$$Q_A = Q_C + pQ_i \quad (6-3)$$

where Q_C and Q_i represent the thermal capacitances of the conductor and insulation respectively.

$$Q_C = c_{cu} * \pi r_c^2 = 3131.96 \text{ J/m} - \text{ }^\circ\text{C} \quad (6-4)$$

$$Q_i = \pi(r_i^2 - r_c^2) * c_i = 6554.93 \text{ J/m} - \text{ }^\circ\text{C} \quad (6-5)$$

The Van Wormer coefficient is calculated using the following formula [8].

$$p = \frac{1}{2 \ln \frac{r_i}{r_c}} - \frac{1}{\left(\frac{r_i}{r_c}\right)^2 - 1} = 0.377 \quad (6-6)$$

Substituting the values of p , Q_C and Q_i into (6-7), we can calculate the value of Q_A .

$$Q_A = Q_C + pQ_i = 5603.16 \text{ J/m} - \text{ }^\circ\text{C} \quad (6-7)$$

Thermal resistance, T_B , is comprised of the thermal resistances of the sheath, armor, and external covering of the power cable and includes the insulation loss factor as given by

(6-8),

$$T_B = (1 + \lambda_1)T_3 \quad (6-8)$$

where T_3 is the thermal resistance between the insulation screen and sheath. Equation (2-14) can be used to calculate the value of T_3 .

$$T_3 = \frac{\rho_j}{2\pi} \ln \frac{r_i}{r_j} = 0.104 \text{ }^\circ\text{C} - \text{m/W} \quad (6-9)$$

$$T_B = (1 + \lambda_1)T_3 = 0.1134 \text{ }^\circ\text{C} - \text{m/W} \quad (6-10)$$

To calculate the value for Q_B , we need to include the thermal capacitance of the power cable jacket in the insulation using the Van Wormer coefficients. The formula for Q_B is,

$$Q_B = (1 - p)Q_i + \frac{Q_s + p'Q_j}{1 + \lambda_1} \quad (6-11)$$

where Q_s and Q_j are the thermal capacitances of the sheath and jacket, respectively, and p' and p are the Van Wormer coefficients given by (6-6) and (6-12).

$$p' = \frac{1}{2 \ln \frac{r_j}{r_i}} - \frac{1}{\left(\frac{r_j}{r_i}\right)^2 - 1} = 0.477 \quad (6-12)$$

$$Q_s = c_{cu} * \pi(r_s - r_c)^2 = 4.58 \text{ J/m} - \text{ }^\circ\text{C} \quad (6-13)$$

$$Q_j = c_j * \pi(r_j - r_s)^2 = 30.41 \text{ J/m} - \text{ }^\circ\text{C} \quad (6-14)$$

Substituting these values into (6-11), we get

$$Q_B = (1 - p)Q_i + \frac{Q_s + p'Q_j}{1 + \lambda_1} = 4101.23 \text{ J/m} - \text{ }^\circ\text{C} \quad (6-15)$$

Once the values of the thermal resistances and thermal capacitances of the power cable's layers were calculated it was important to calculate the thermal resistance and capacitance of the soil surrounding the power cable, T_4 , which also influences the heat flow from the underground power cable.

6.2.2 Soil Thermal Model

Once the parameters for cable equivalent RC thermal circuit were calculated, next step was to develop a RC thermal circuit for the soil model, as shown in section 2.6. The soil RC circuit was developed for both Case A and Case B of Figure 6-2. For modeling the power cable and spare duct for the Brandow-Pickrell installation, we have divided the soil into five layers for which the value of $\gamma = 1.32$ is used, as provided in the table in the reference paper [9]. The radius of the cable in our model is $r_{cable} = 0.042$ m. For Case A, the burial depth in our model is $h = 1.6764$ m and the model depth was calculated using (2-20), with $d_m = 3.352$ m. Once these values were determined, the values of b_i , th_i , r_{inti} , r_{exti} , R_{si} and C_{si} , for the Case A were calculated using the equations (2-14) - (2-19). These values are shown in Table 6-3 below. The soil thermal resistivity, ρ_{soil} , was taken as $1 \text{ }^\circ\text{C}\cdot\text{m}/\text{W}$ and the specific heat capacity of soil, C_{soil} , was taken as $1.44 \times 10^6 \text{ W}\cdot\text{s}/^\circ\text{C}\cdot\text{m}^3$ for the calculation.

Table 6-3 Values of thermal resistances and capacitances for the soil model for Case A

	Units	Layer number (<i>i</i>)					
		0	1	2	3	4	5
b_i	m	0.042	0.05437	0.100676	0.274019	0.922913	3.352
th_i	m		0.01237	0.046306	0.173343	0.648895	2.429087
r_{int}	m		0.042	0.05437	0.100676	0.274019	0.922913
r_{ext}	m		0.05437	0.100676	0.274019	0.922913	3.352
R_{Ti}	m-°C/W		0.0410858	0.098057	0.159365	0.193274	0.20528
R_{Si}	m-°C/W	0.0205429	0.0695716	0.128711	0.176319	0.199277	0.10264
C_{Si}	W-s/°C-m		5.39E+03	3.25E+04	2.94E+05	3.51E+06	4.70E+07

Similarly, for the Case B with burial depth, $h = 2.7432$ m, the model depth (d_m) was found to be 5.486 m and the values of b_i , th_i , r_{inti} , r_{exti} , R_{si} and C_{si} , were calculated and are shown in Table 6-4.

Table 6-4 Values of thermal resistances and capacitances for the soil model for Case B

	Units	Layer number (<i>i</i>)					
		0	1	2	3	4	5
b_i	m	0.042	0.0623453	0.138506	0.42361	1.490871	5.486078
th_i	m		0.0203453	0.076161	0.285103	1.067261	3.995208
r_{int}	m		0.042	0.062345	0.138506	0.42361	1.490871
r_{ext}	m		0.0623453	0.138506	0.42361	1.490871	5.486078
R_{Ti}	m-°C/W		0.0628711	0.127046	0.177924	0.200271	0.207362
R_{Si}	m-°C/W	0.0314355	0.0949584	0.152485	0.189097	0.203816	0.103681
C_{Si}	W-s/°C-m		9.60E+03	6.92E+04	7.25E+05	9.24E+06	1.26E+08

Once these values were determined, the ambient temperature of the soil was modeled as a constant 20 °C for the CEST model. The spare duct location on the ladder model was determined by measuring the thermal resistance of the soil at a distance equal to the distance of the spare duct from the power cable and locating that thermal resistance in the ladder model. The RC ladder network was developed and was modeled in MATLAB Simulink.

6.2.3 CEST model for MATLAB and its Validation

The CEST model for MATLAB was simulated for the Case B with no variation in the earth's surface temperature. Figure 6-17 shows the developed circuit in Simulink. Table 6-5 below provides the legend for all the symbols used in the MATLAB Simulink models throughout this chapter. The current source represents the heat generated by the conductor. These are the I^2R losses and dielectric losses in the conductor and depend on the amount of current flowing through it. Since the RC thermal network models for the soil layers had (and typically have) large time constants, it took a long time (463 days) for the model's spare-duct simulated temperature to stabilize. Since we did not have enough current data for the simulation period, the conductor current data was modeled as a sinusoid (since the load current from the EMS vaguely resembled a sinusoid) with a period of 24 hours and it varied from 160 A to 245 A. This load current was replicated for each day for the period of the simulation. This is the same load current which was modeled for the CEST model in CYMCAP. The conductor current was modeled such that it peaked at 3:00 PM every day (as was observed from the EMS data).

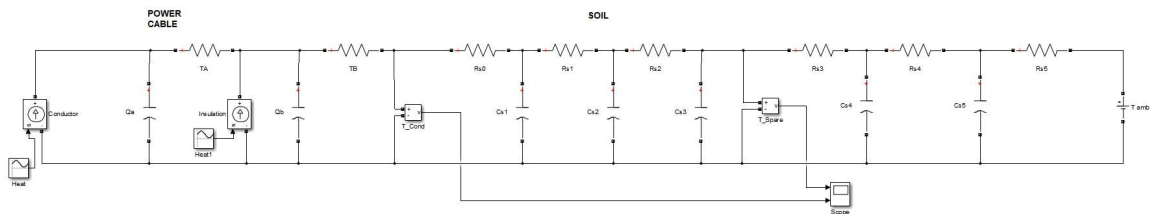

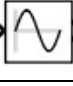


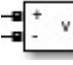





Figure 6-17 MATLAB Simulink ladder model for the power cable in the underground installation

Table 6-5 Legend for the MATLAB simulation models

Sl. No.	Symbol	Description
1.		Controlled current source – used to replicate heat generation from cable
2.		Sine wave – used as input for controlled current source and earth’s surface temperature input
3.		Resistor – used as thermal resistance
4.		Capacitor – used as thermal capacitance
5.		Voltmeter – used to measure temperature
6.		Scope – used to plot temperatures
7.		DC voltage source – used for constant earth’s ambient temperature
8.		MATLAB function – used to define function for calculating the effect of time varying earth’s surface temperature

Two ‘voltmeters’ were placed in the model to measure the voltage, which is an analog for the temperature in our model: one after the power cable jacket RC network and another at the location of the spare duct. The model was simulated for an interval of 4×10^7 seconds (463 days) of MATLAB simulation time. Once the model was simulated, the temperatures were plotted through the Simulink scope tool connected to the voltmeters. The result of the simulation can be seen in Figure 6-18 below.

A comparison of the power cable temperature and spare duct temperature from the MATLAB simulation data (Figure 6-18) with the measured data (Figure 6-6) was made to validate the CEST model. Comparative results are presented in the Table 6-6 below.

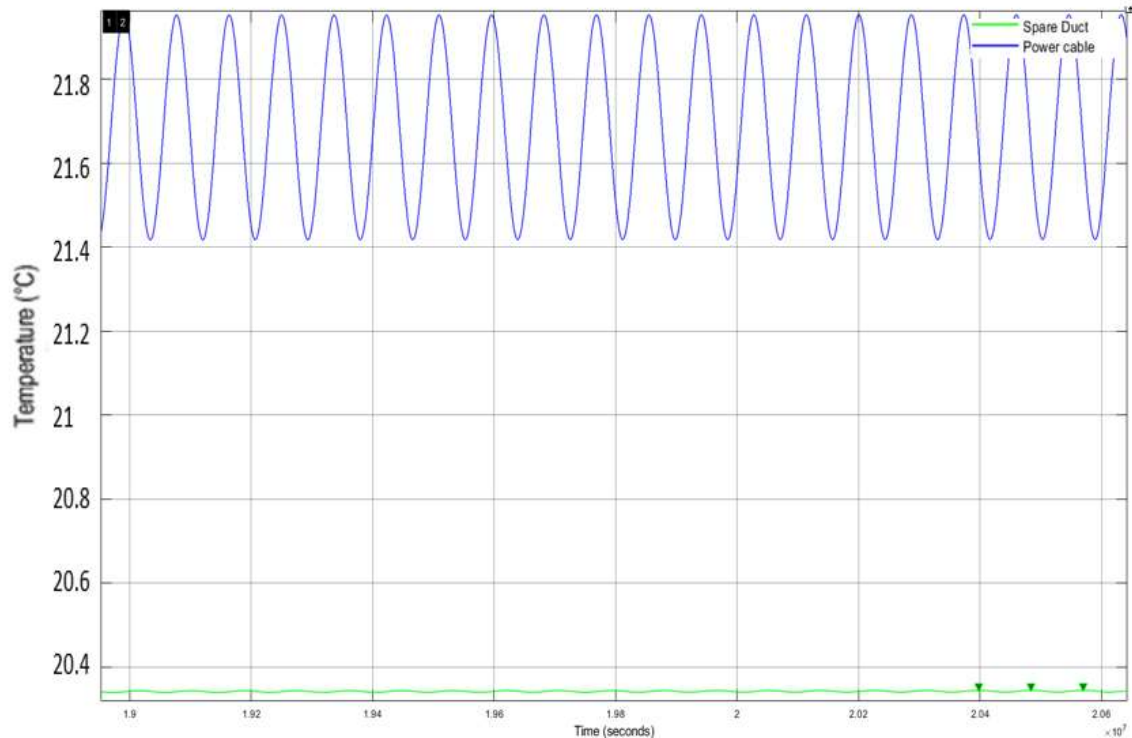


Figure 6-18 Simulation results for the CEST model in MATLAB Simulink

Table 6-6 Comparison of CEST model results in MATLAB and the measured data

	Measured data	MATLAB model results	CYMCAP results
Main power cable jacket temperature (°C)	26.4 – 29.8	21.4 – 21.9	21.1-21.9
Spare duct temperature (°C)	26.8 - 35.0	20.34 (constant)	20.6 (constant)
Time at which power cable temperature peaks	03:00 PM	05:30 PM	05:30 PM
Time at which spare cable temperature peaks	01:30 PM	N/A	N/A

The simulation results still showed some deviation from the measured data however the MATLAB simulation results were very close to what was observed in CYMCAP for the CEST model simulation. The next step was to include the effects of the earth's surface heating into the model.

6.2.4 TVEST model for MATLAB

Solar radiant heat propagation through the earth's surface into the ground is through conduction, as depicted in Figure 6-19. For a one-dimensional steady heat conduction through the earth's surface, Fourier's law of heat transfer was used,

$$Q = -kA \frac{dT}{dx} \quad (6-16)$$

where Q is the rate of heat flow through the earth's surface, k is the thermal conductivity and $\frac{dT}{dx}$ is the rate of change of the temperature with depth x from the earth's surface.

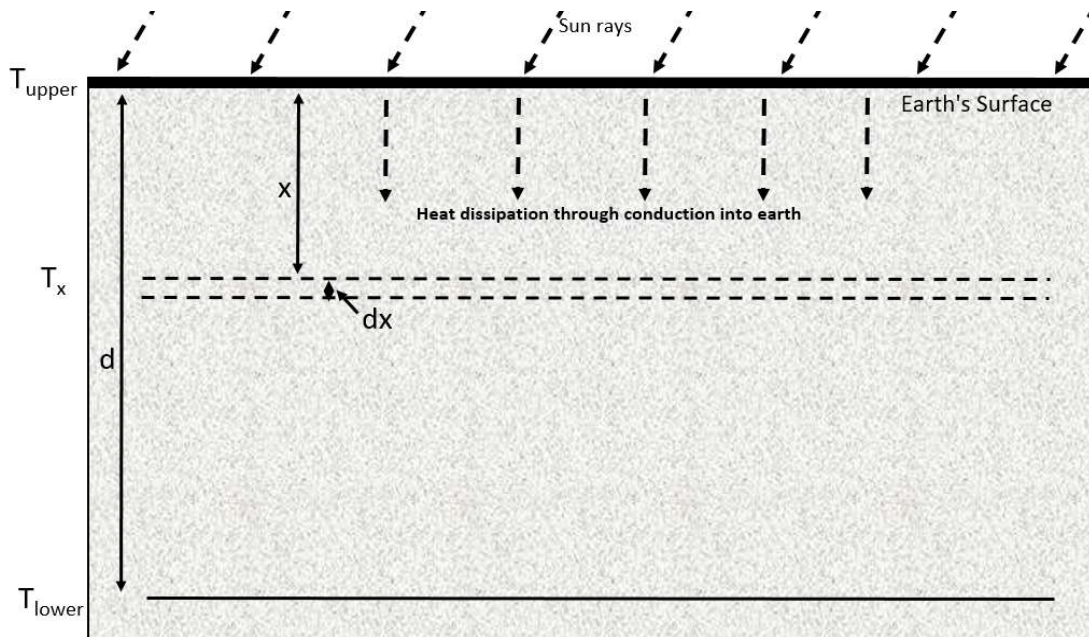


Figure 6-19 Heat dissipation through conduction into the earth

If there is no other heat source present, then the rate of the heat flow is constant. Therefore $\frac{dT}{dx}$ is constant. This means that, if we know the temperatures T_{upper} and T_{lower} , we can determine the temperature at a depth of x units from the earth's surface. For our models, the earth's surface temperature is T_{upper} , and T_{lower} is the constant earth's ambient temperature at a depth d from the earth's surface. We must determine the appropriate values of T_{lower} and d for our model if we want to use (6-16). It has been observed, through numerous field studies, that the temperature of the earth remains constant at a sufficient depth below the earth's surface [11]. Unfortunately, the values given in these studies did not produce any reliable results in our simulation. Since our goal was to reach an acceptable combination of d and T_{lower} so that we could get the simulation results as close to the measured data as possible, many different combinations for d and T_{lower} were tested in the model. After many iterations, the depth, d , and temperature, T_{lower} , were found to be 3 m and 15 °C (59 °F).

To determine the temperature T_x at any distance, x , below the earth's surface due to the earth's surface heating, we will use equation (6-17),

$$\frac{T_{upper} - T_x}{x} = \frac{T_{upper} - T_{lower}}{d} \tag{6-17}$$

$$T_x = \frac{(d - x)T_{upper} + x \cdot T_{lower}}{d}$$

Once the effect of the earth's heating was calculated at the depth of the spare duct and main power cable duct for both Case A and Case B, the superposition was used to determine the total temperatures in the duct. The temperature at any point inside the installation is the

sum of the temperatures due to the heat dissipation from the power cable and due to the heat transfer from the earth's surface heating. For the Case A, the spare duct and main power cable are at the same depth from the earth's surface, therefore the effect of the earth's surface heating is similar for both the spare duct and the main power cable. The effect from the earth's surface heating is added to the heating from the conductor to calculate the temperatures of both the power cable and spare duct. For the Case B, the spare duct and main power cable are at different depths, therefore the effect of earth's heating is calculated separately for each duct and then it is added to the temperature due to the conductor-generated heat to get the final temperature in the power cable and spare duct. The MATLAB Simulink model was modified to include the effects of the earth's surface heating as shown in Figure 6-20 for the Case A and Figure 6-21 for Case the B.

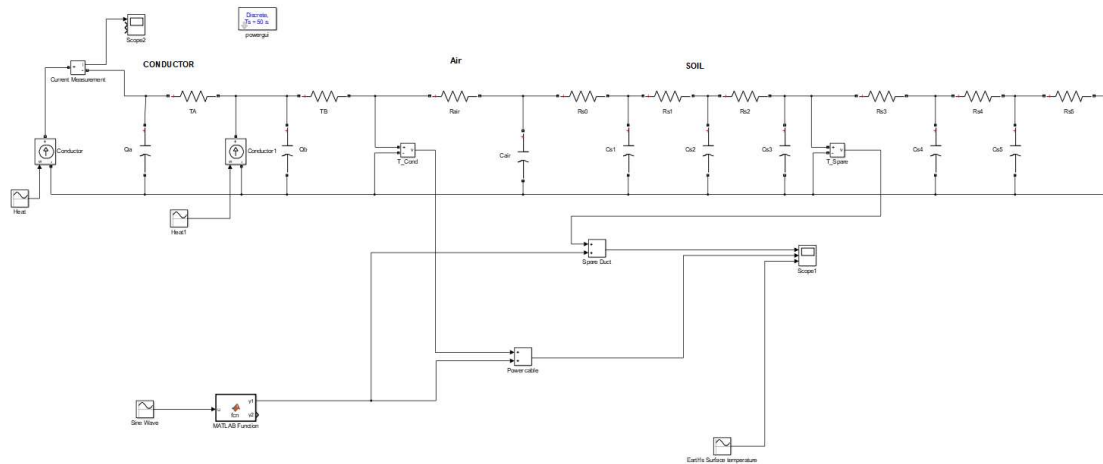


Figure 6-20 MATLAB Simulink TVEST model for Case A

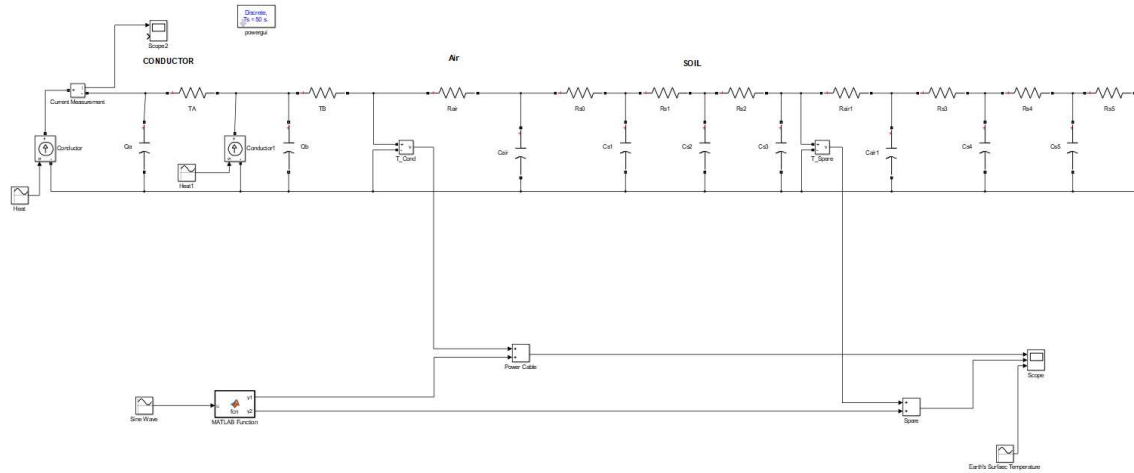


Figure 6-21 MATLAB Simulink TVEST model for Case B

6.3 Results

Recall Table 5-1, where it was shown that the hotspot temperatures in the spare duct and the main power cable are significantly higher during the summer season, that is, for the months of May, June and July. Since these months with the highest hotspot temperatures are of most interest (and will provide the binding constraint if any thermal constraint is binding), simulations were performed using the MATLAB model for the data measured from these months. The model was simulated for two cases as shown in Figure 6-2. In Case A, Figure 6-20, the spare duct lies at the same depth as the power cable duct. The effect of the earth's surface heating is the same for both the spare duct and the main power cable duct. In Case B, Figure 6-21, the spare duct lies directly above the power cable duct and is closer to the earth's surface. The earth's heating therefore has a greater effect on the spare duct than the main power cable duct. The earth's surface temperatures were measured on March 08, March 10, June 04 and June 20, 2017 and these measured values were used as inputs to the models when the simulations were conducted for similar days.

Figure 6-22, Figure 6-23, Figure 6-24 and Figure 6-25 show the earth's surface temperature variations as measured on March 08, March 10, June 04 and June 20, 2017, respectively. These plots were developed using the measured data (indicated by red dots on the plots in Figure 6-22 - Figure 6-25) and the Microsoft Excel spreadsheet's curve fitting algorithm. The days, the earth's surface temperatures were measured, were selected based on availability of SRP's IR gun and weather conditions on those days. The earth's surface temperature data for June 20, 2017 was important as it was one of the hottest days of summer and the load on the power cables doubled that day due to the extreme heat in Tempe. The measured temperature profiles were used to calculate the effect of the earth's surface heating at the depth of the spare duct and the main power cable duct.

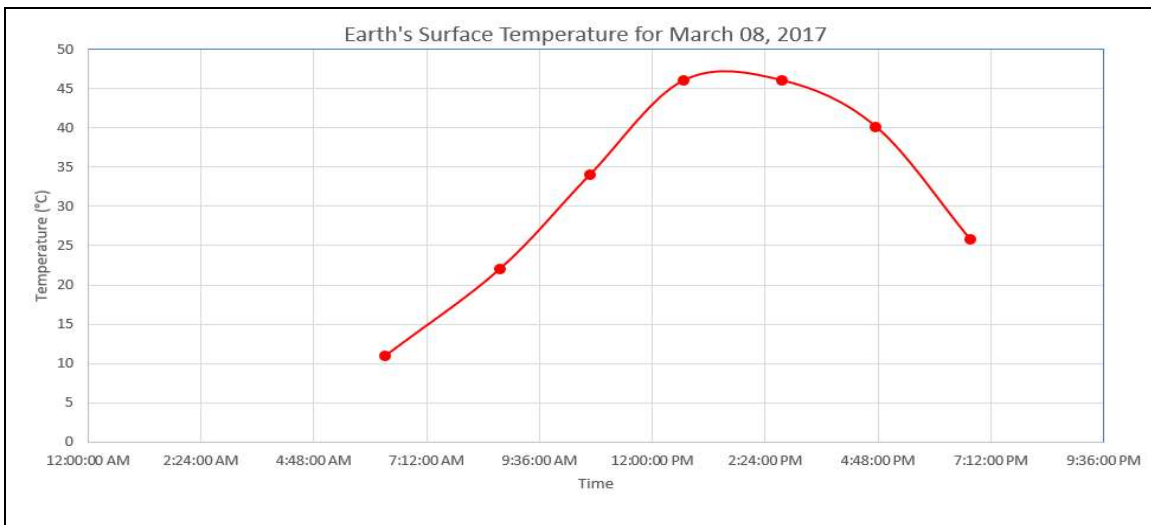


Figure 6-22 Measured earth's surface temperature data plots for March 08, 2017

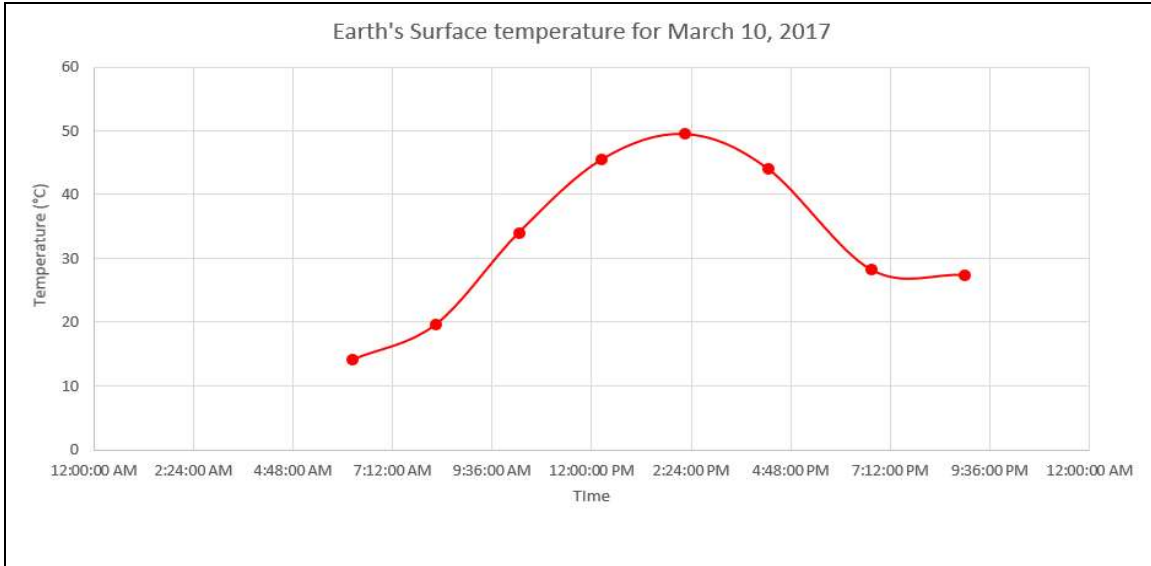


Figure 6-23 Measured earth's surface temperature data plots for March 10, 2017

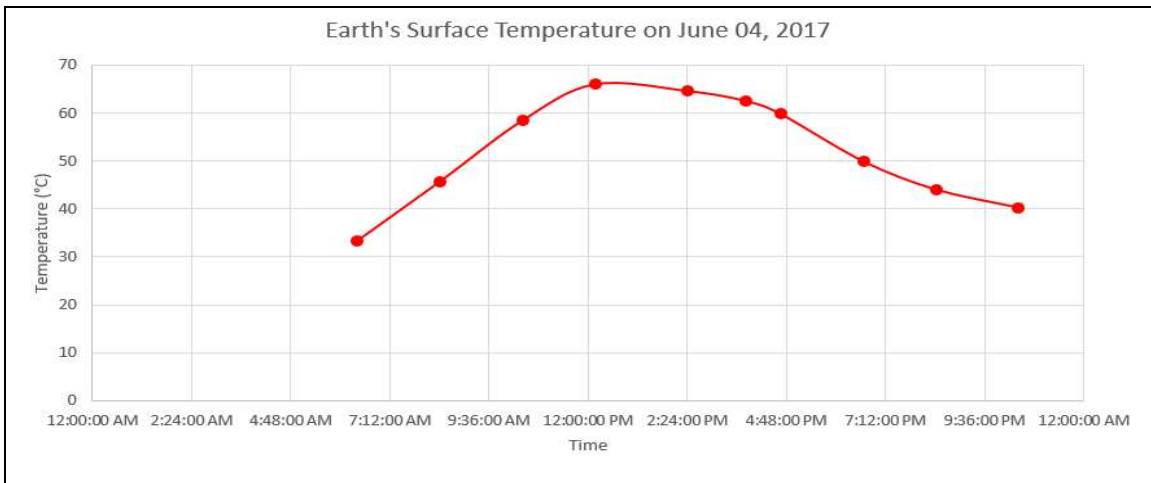


Figure 6-24 Measured Earth's Surface temperature data for June 04, 2017

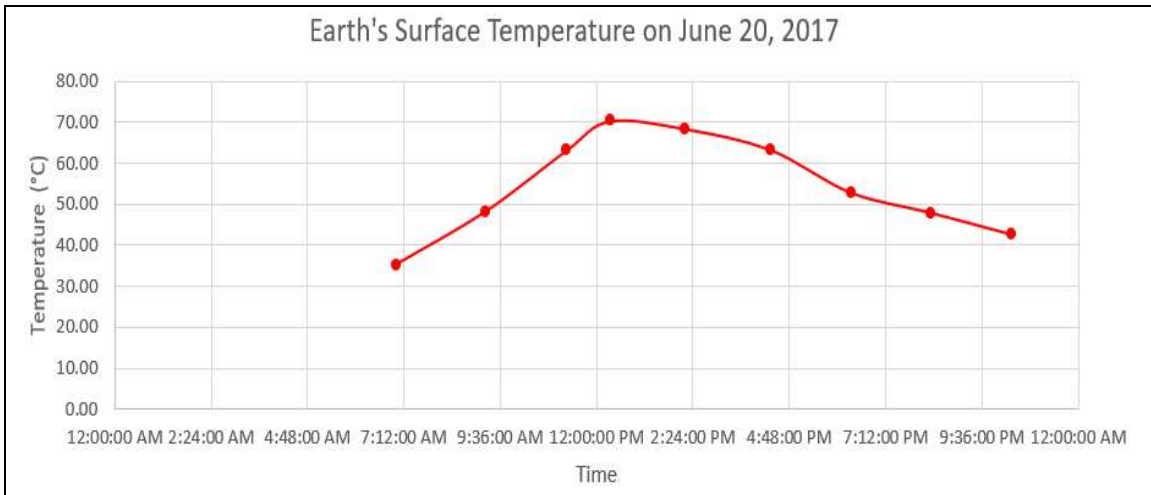


Figure 6-25 Measured Earth's Surface temperature data for June 20, 2017

Figure 6-26 - Figure 6-29 show the load current in the power cable on March 08, March 10, June 04 and June 20, 2017. These current values were downloaded from the energy management system at SRP.

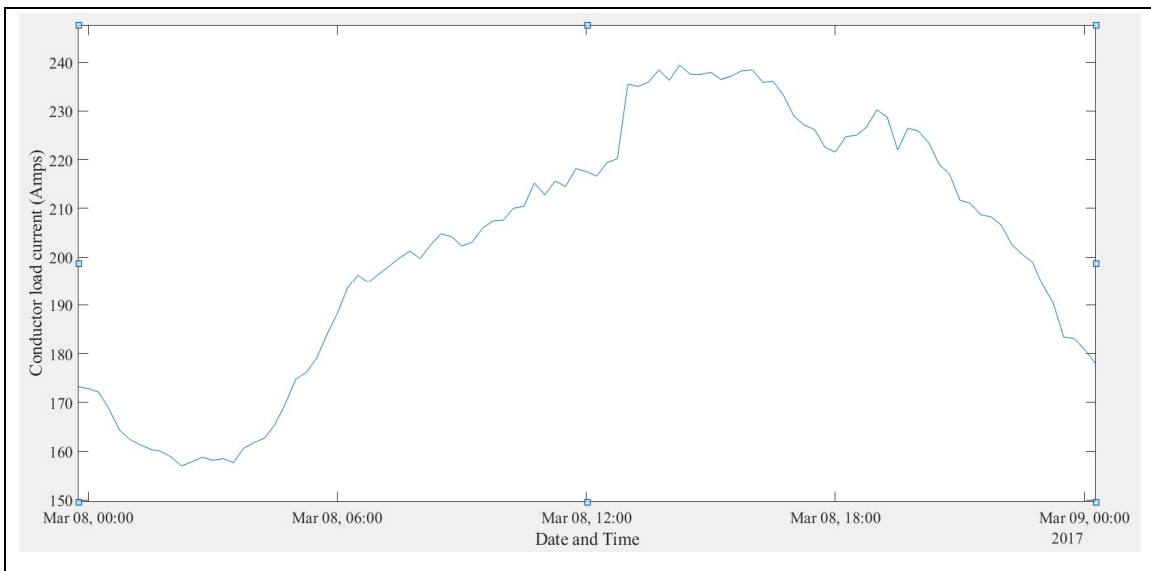


Figure 6-26 Conductor load current on March 08, 2017

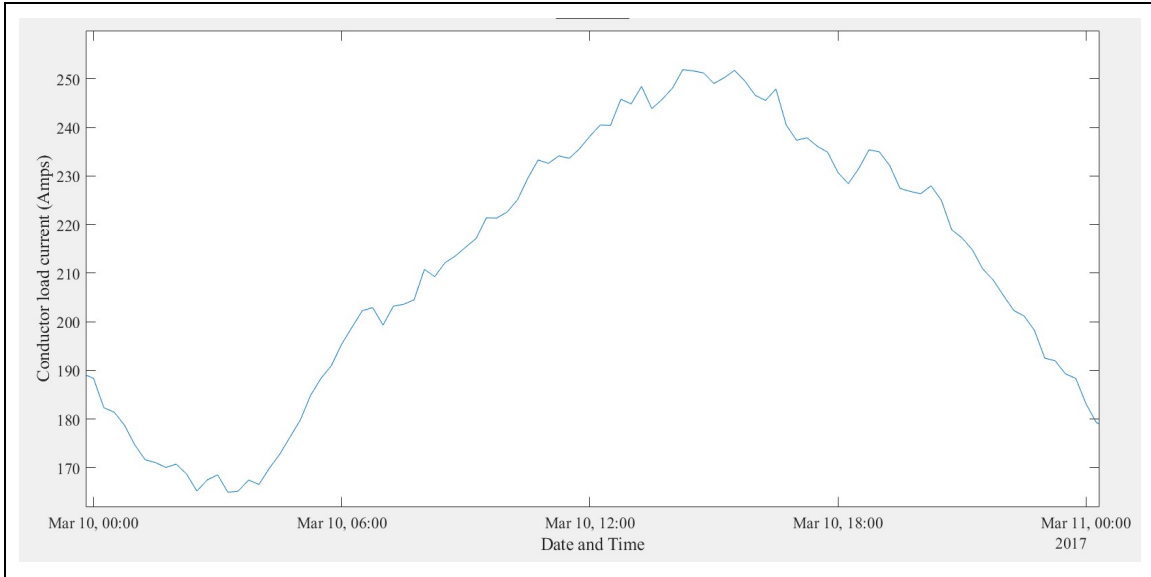


Figure 6-27 Conductor load current on March 10, 2017

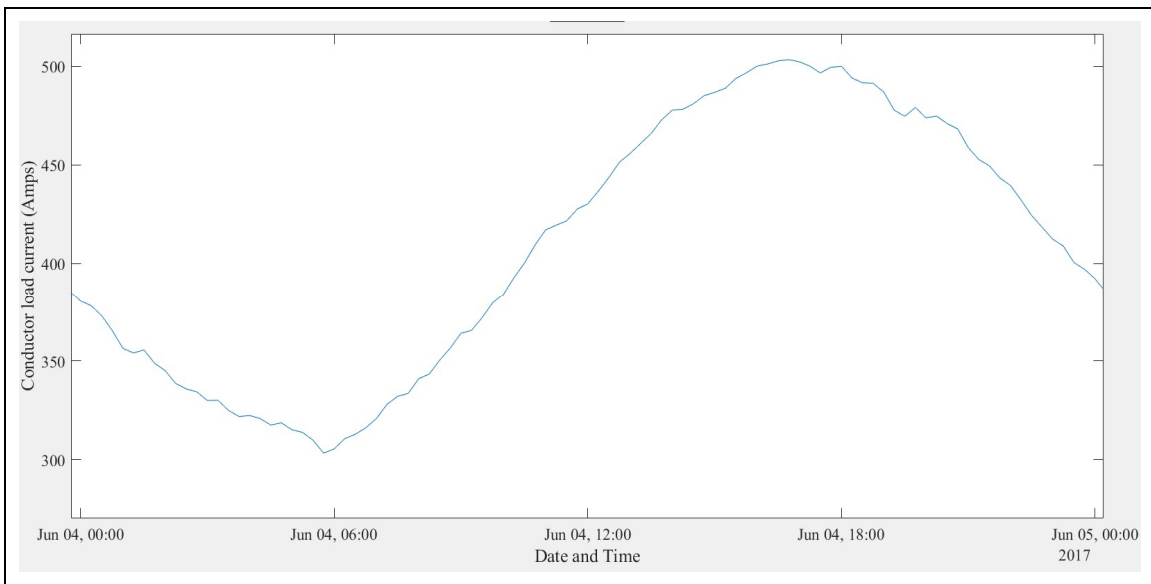


Figure 6-28 Conductor load current on June 04, 2017

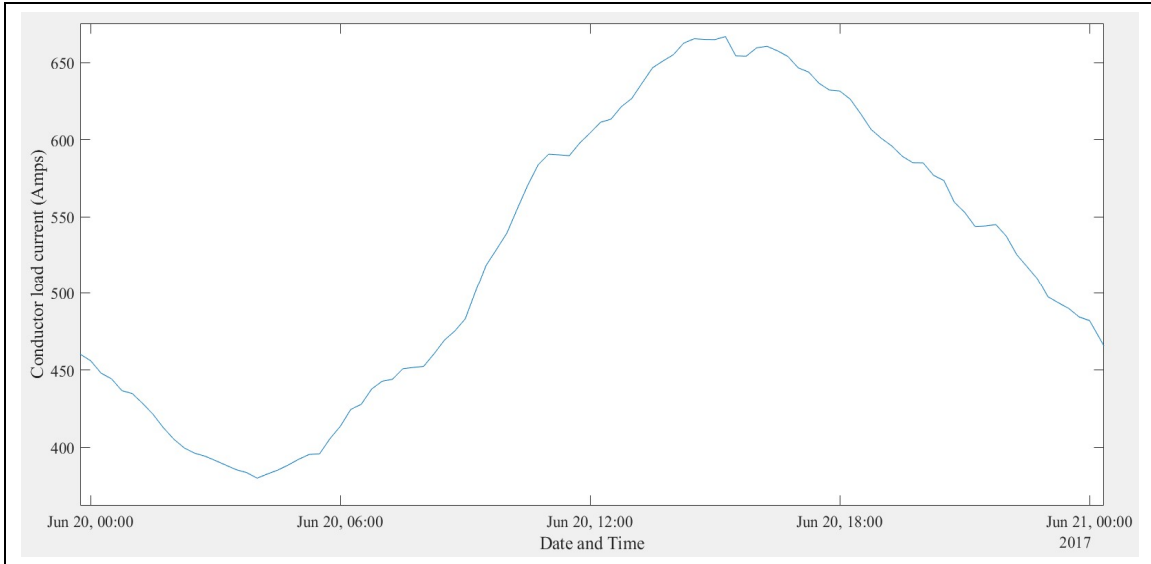


Figure 6-29 Conductor load current on June 20, 2017

The earth's surface temperature data, the I^2R losses in the conductor and the dielectric losses in the cable insulation were used as inputs to the MATLAB models shown in Figure 6-20 and Figure 6-21. The simulation results are discussed in following section.

6.3.1 Simulation results for Case A

Figure 6-30 - Figure 6-33 show four plots of MATLAB simulation results, one each for the days in which the surface temperature was measured. Each plot shows the earth's surface temperature, the power cable temperature and the spare duct temperature, for Case A. The simulation was run for 4×10^7 seconds (463 days) in the MATLAB simulation time. The plot was zoomed in to show the 24-hour interval, after each simulation had reached a steady-state temperature profile. The red curve represents the earth's surface temperature. The green curve represents the spare duct temperature and the blue curve represents the power cable temperature.

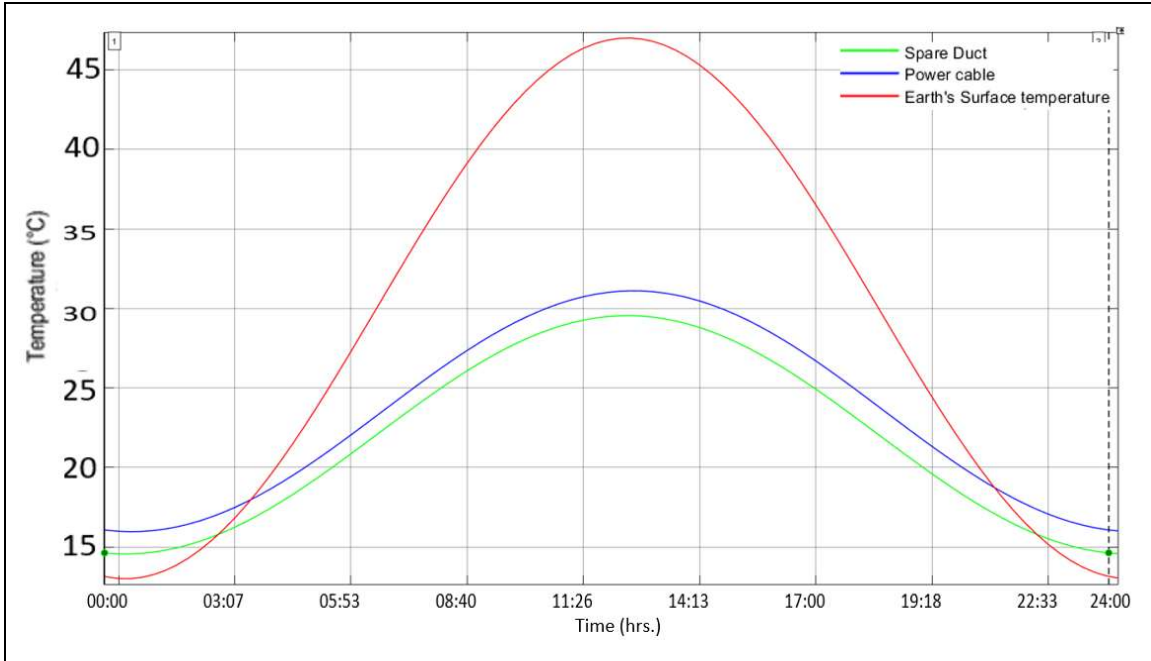


Figure 6-30 Simulation results for the MATLAB model for Case A for March 08, 2017

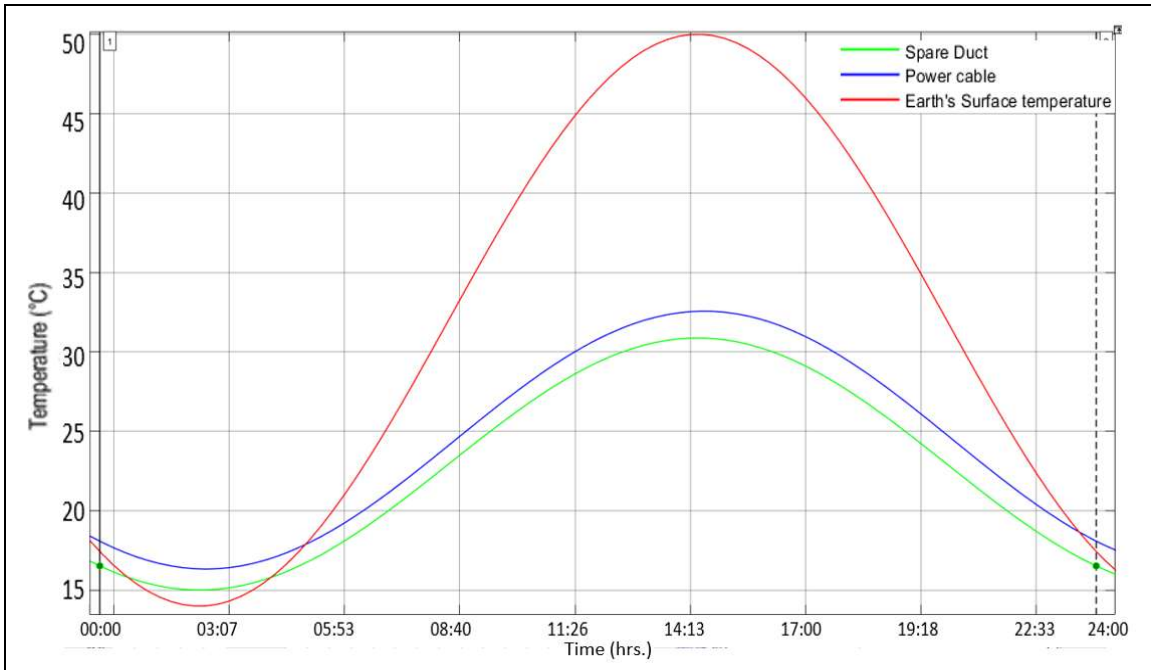


Figure 6-31 Simulation results for the MATLAB model for Case A for March 10, 2017

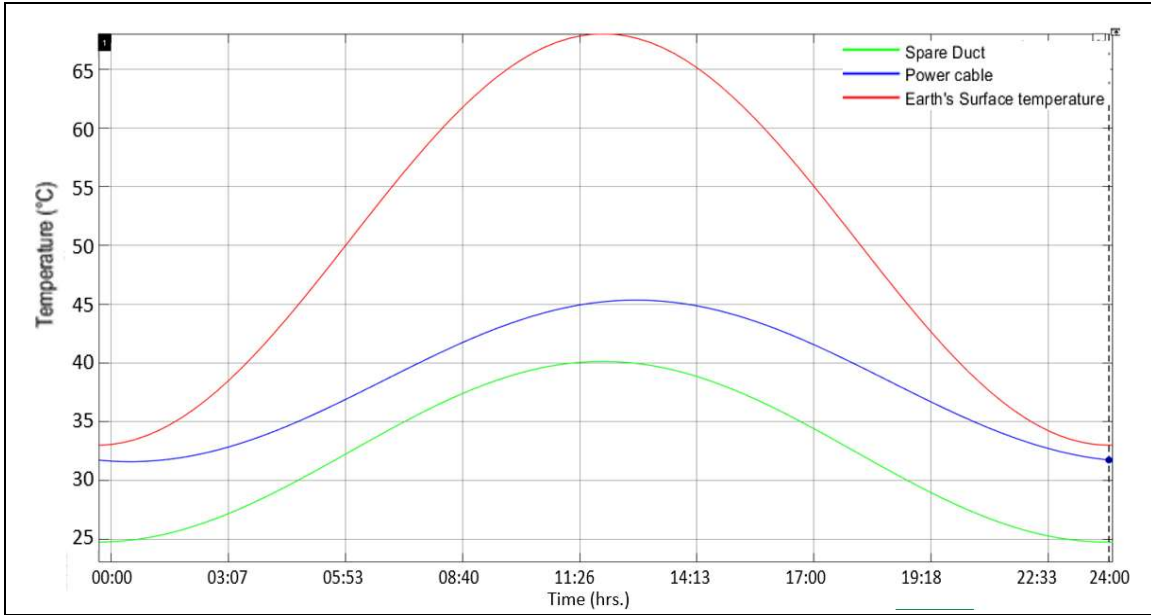


Figure 6-32 Simulation results for the MATLAB model for Case A for June 04, 2017

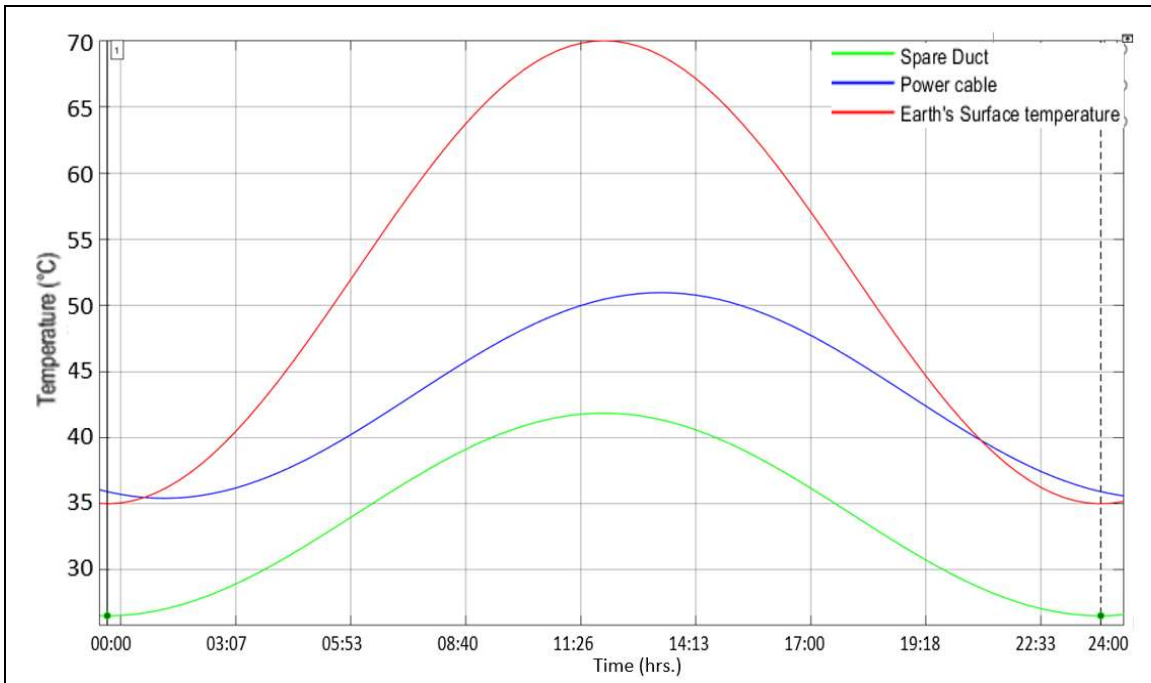
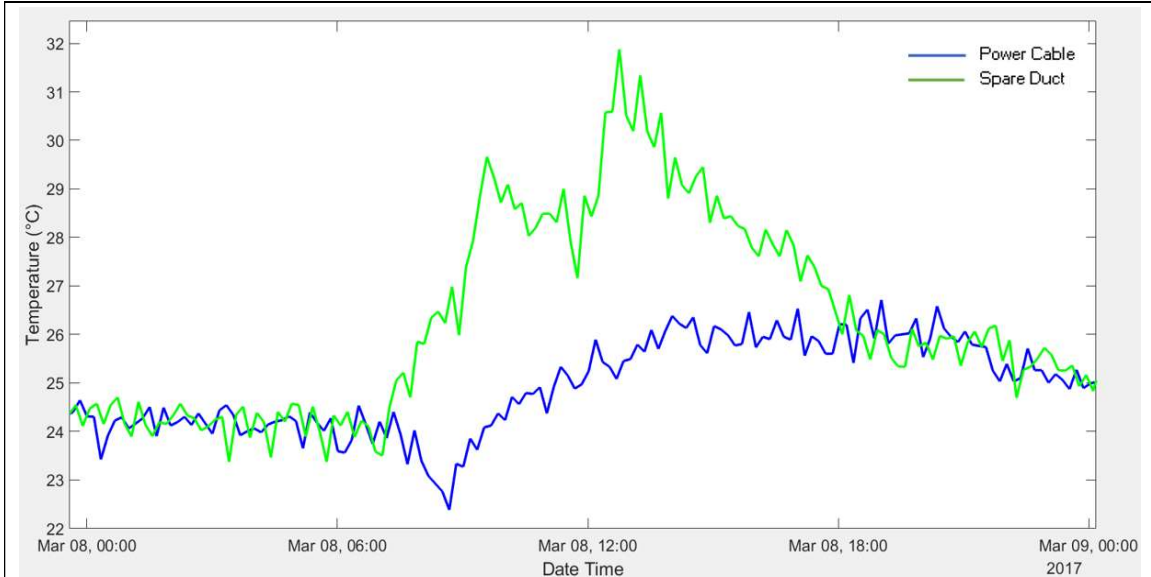


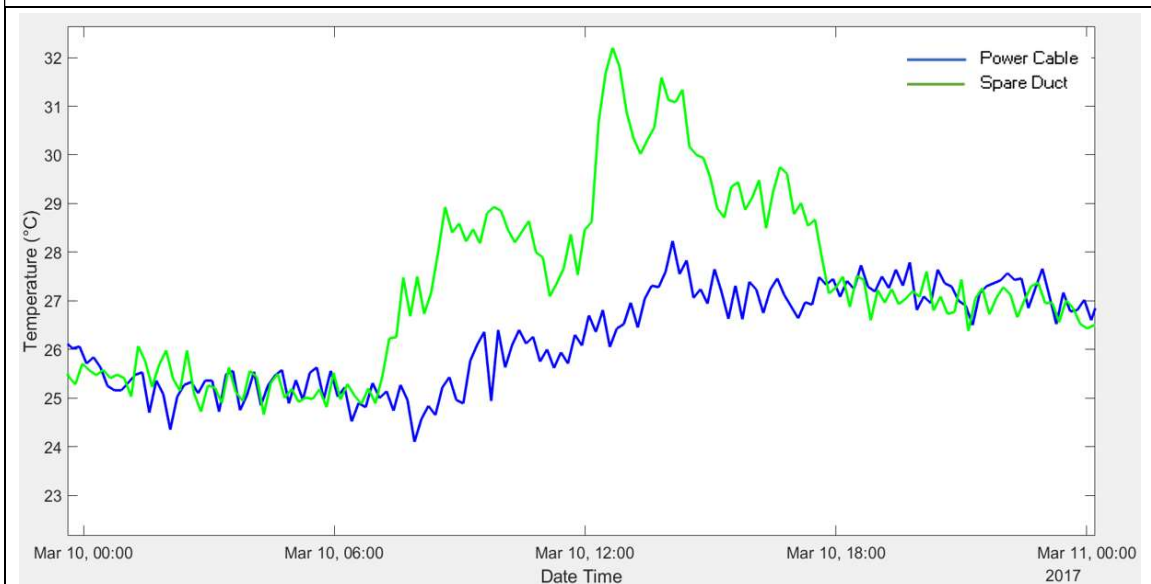
Figure 6-33 Simulation results for the MATLAB model for Case A for June 20, 2017

Figure 6-34 a-b and Figure 6-35 a-b show the plots for the measured temperature data for the reinforced section of the installation, where the spare duct is at the same depth as the

main duct, which houses the power cable. Case A was modeled based on this burial geometry.

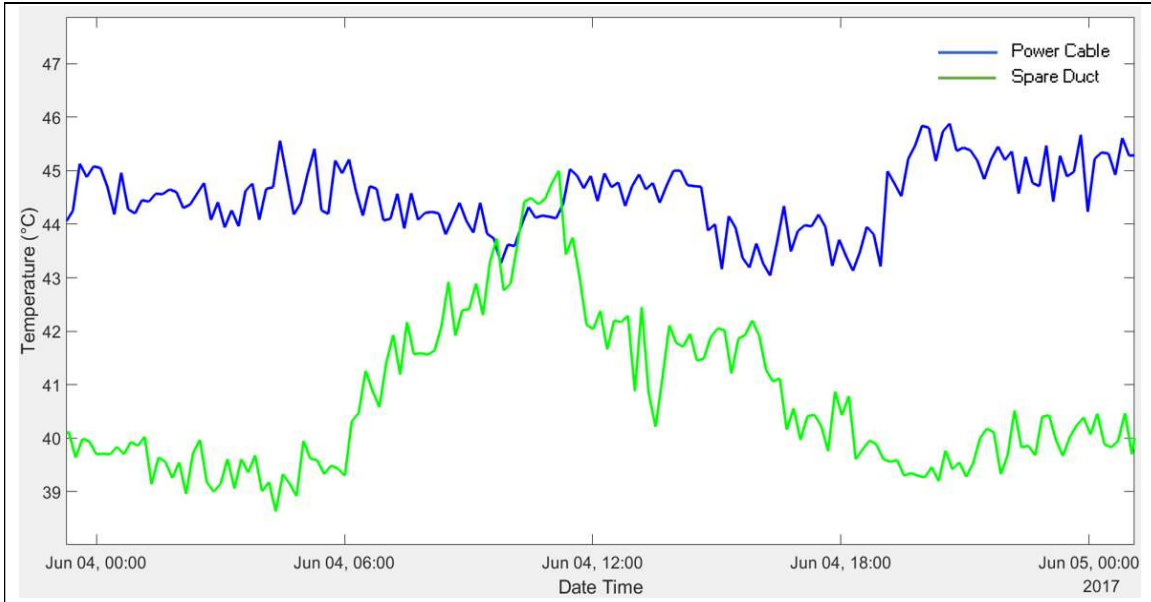


a. Measured temperature for the spare duct and power cable for March 08, 2017

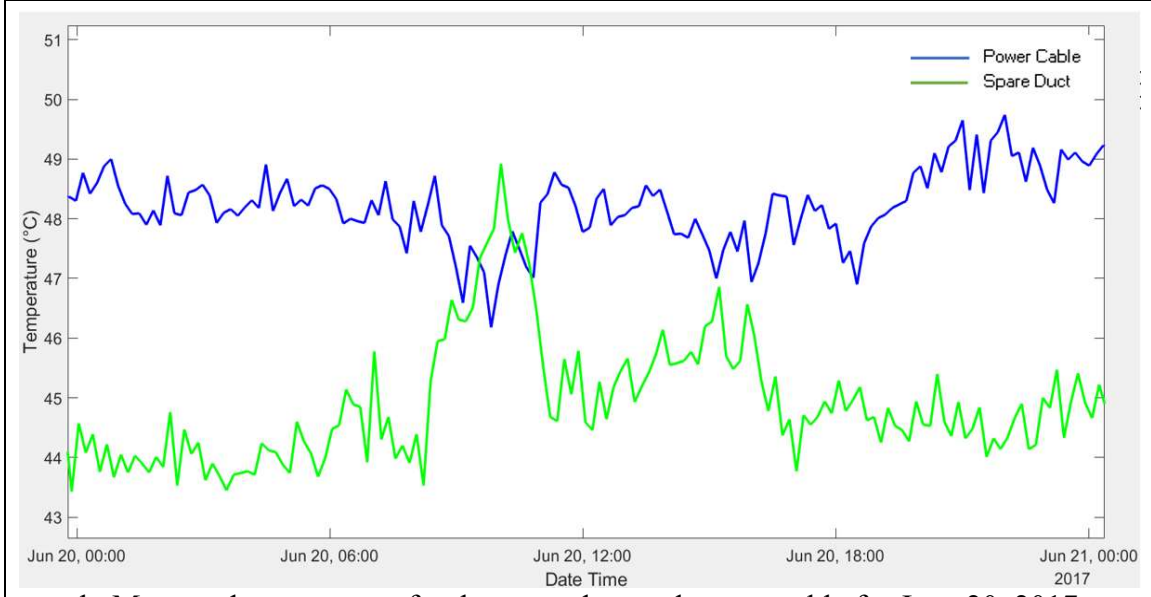


b. Measured temperature for the spare duct and power cable for March 10, 2017

Figure 6-34 Plots for measured temperature in the power cable and the spare duct for March 08, March 10, 2017



a. Measured temperature for the spare duct and power cable for June 04, 2017



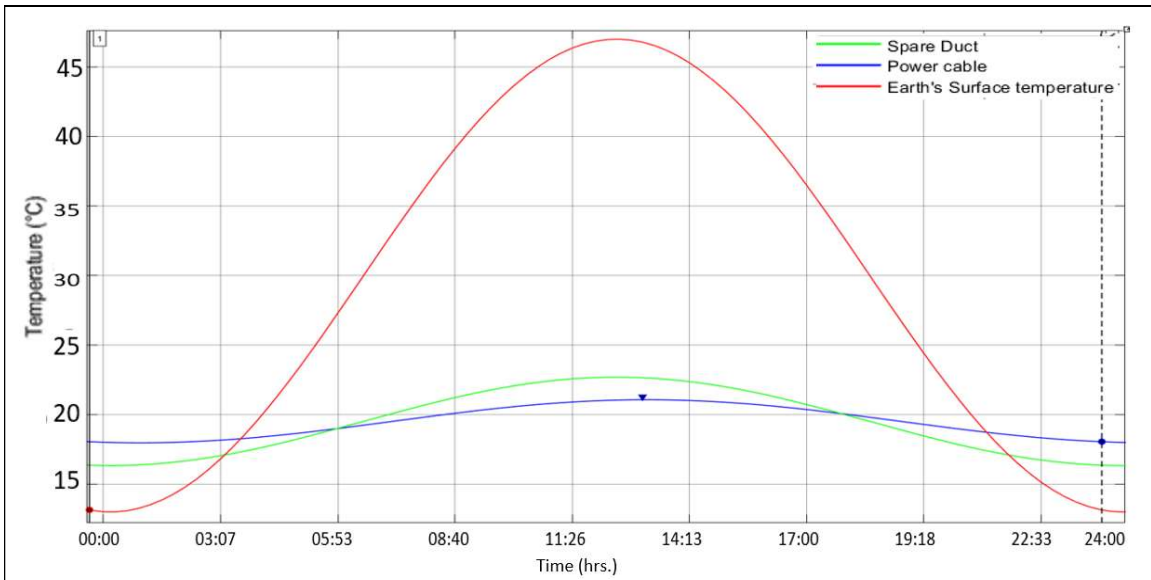
b. Measured temperature for the spare duct and power cable for June 20, 2017

Figure 6-35 Plots for measured temperature in the power cable and the spare duct for June 04 and June 20, 2017

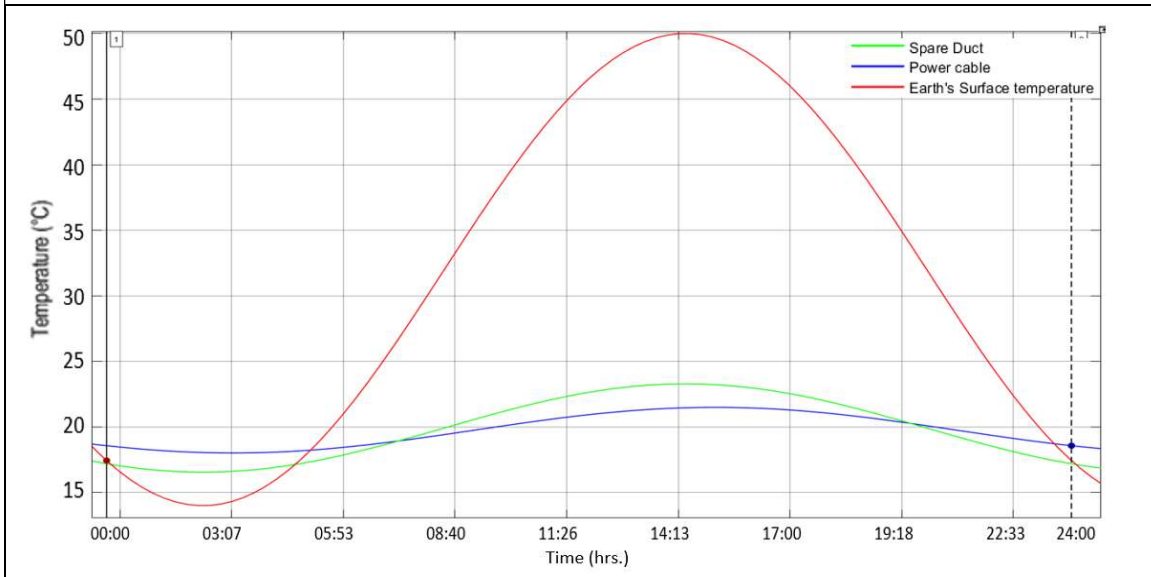
6.3.2 Simulation Results for Case B

For Case B, where the spare duct is at a lower depth than the power cable duct, the earth's surface temperature data from Figure 6-22 - Figure 6-25, the I^2R losses and dielectric losses

calculated from the current load data from Figure 6-26 - Figure 6-29 were used as inputs to the MATLAB model shown in Figure 6-21. The results from the simulation for the four days, i.e. March 08, March 10, June 04 and June 20, 2017 are shown in Figure 6-36 a-b and Figure 6-37 a-b, respectively.

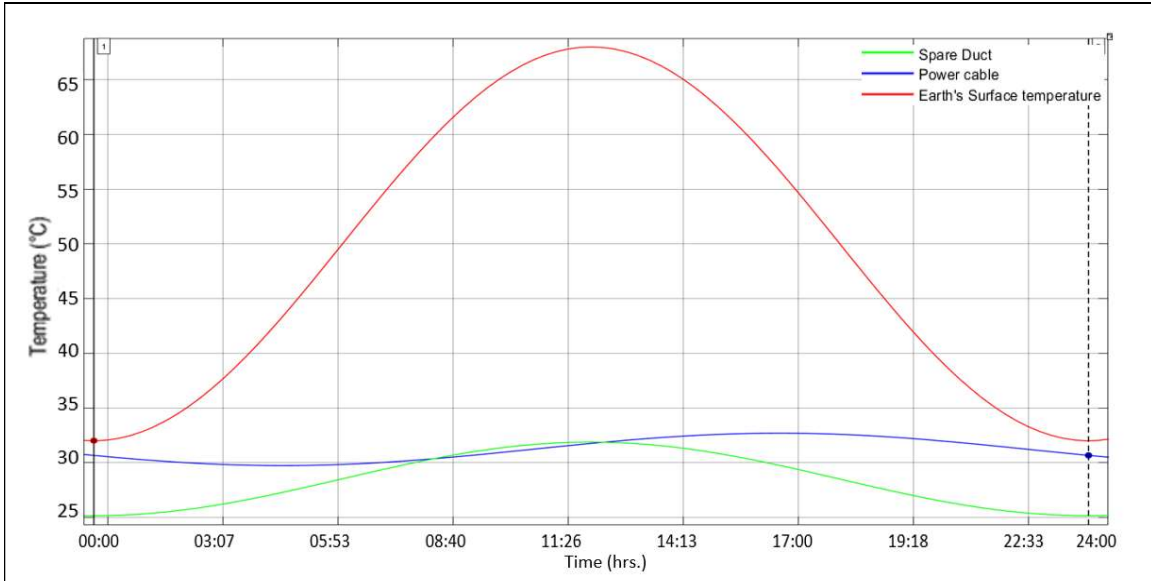


a. Simulation result for spare duct and power cable temperatures for March 08, 2017

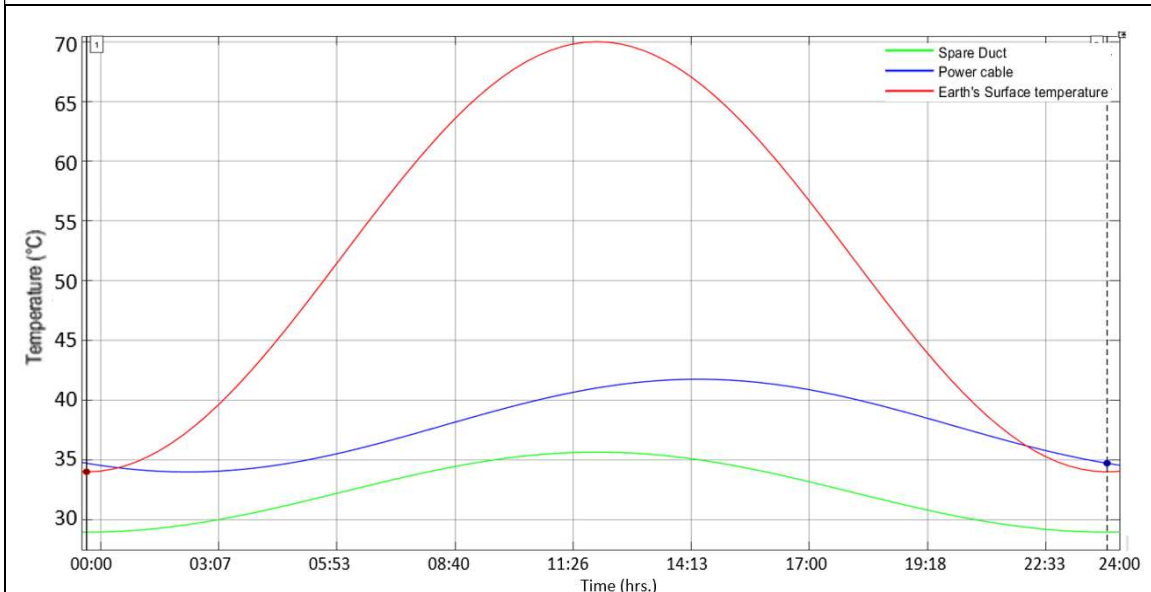


b. Simulation result for spare duct and power cable temperatures for March 10, 2017

Figure 6-36 Simulation results for MATLAB model for Case B for March 08 and March 10, 2017



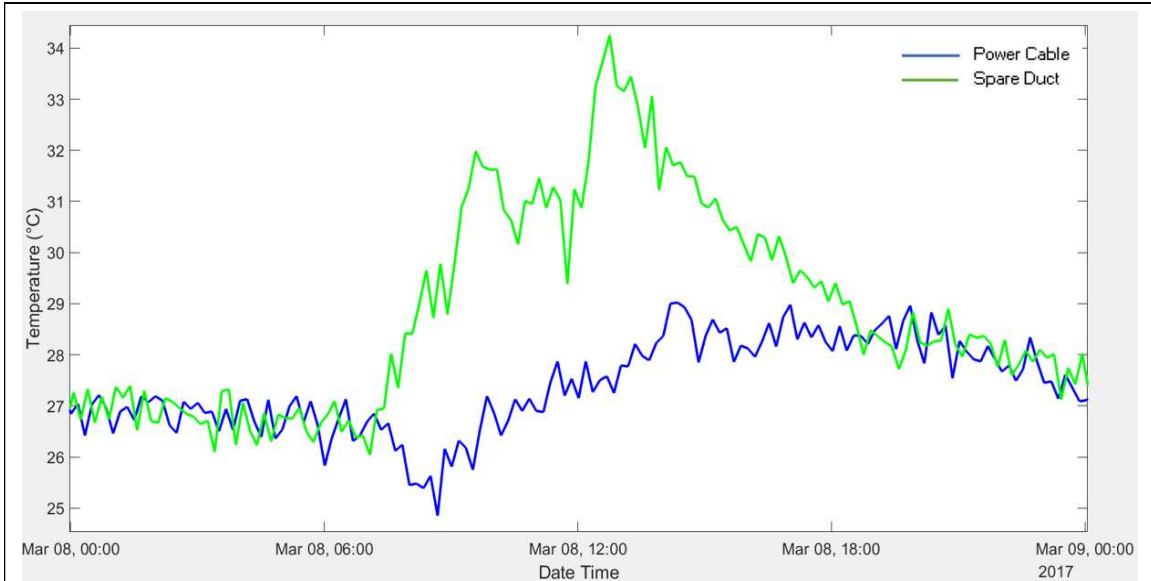
a. Simulation result for spare duct and power cable temperatures for June 04, 2017



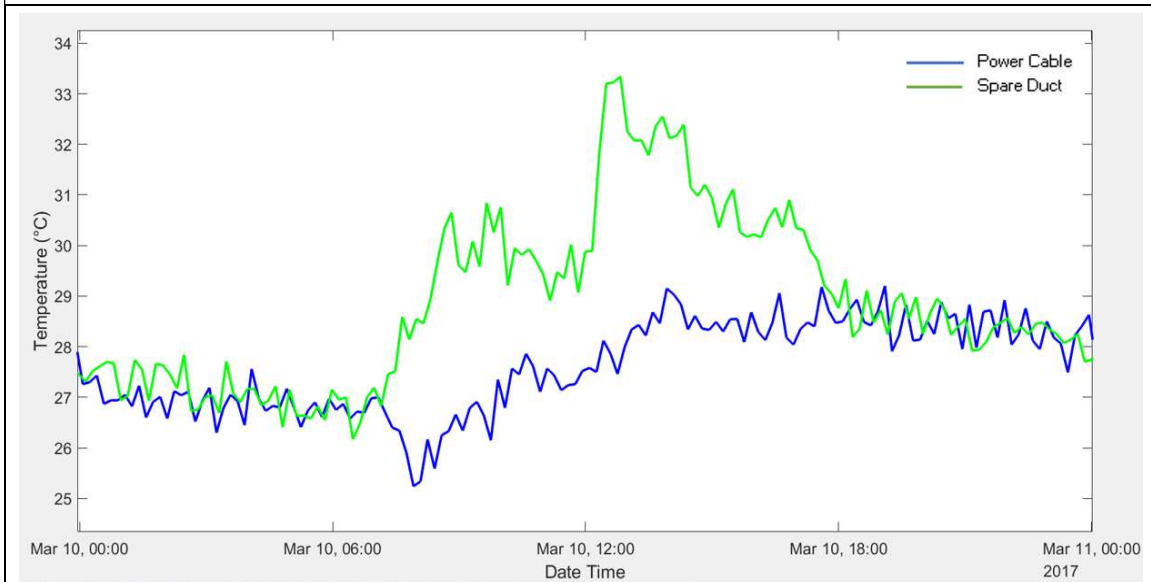
b. Simulation result for spare duct and power cable temperatures for June 20, 2017

Figure 6-37 Simulation results for MATLAB model for Case B for June 04 and June 20, 2017

Figure 6-38 and Figure 6-39 provides the plots of the measured temperatures in the power cable and the spare duct on March 08, March 10, June 04 and June 20, 2017 for that part of the installation where the spare duct is located above the power cable duct.

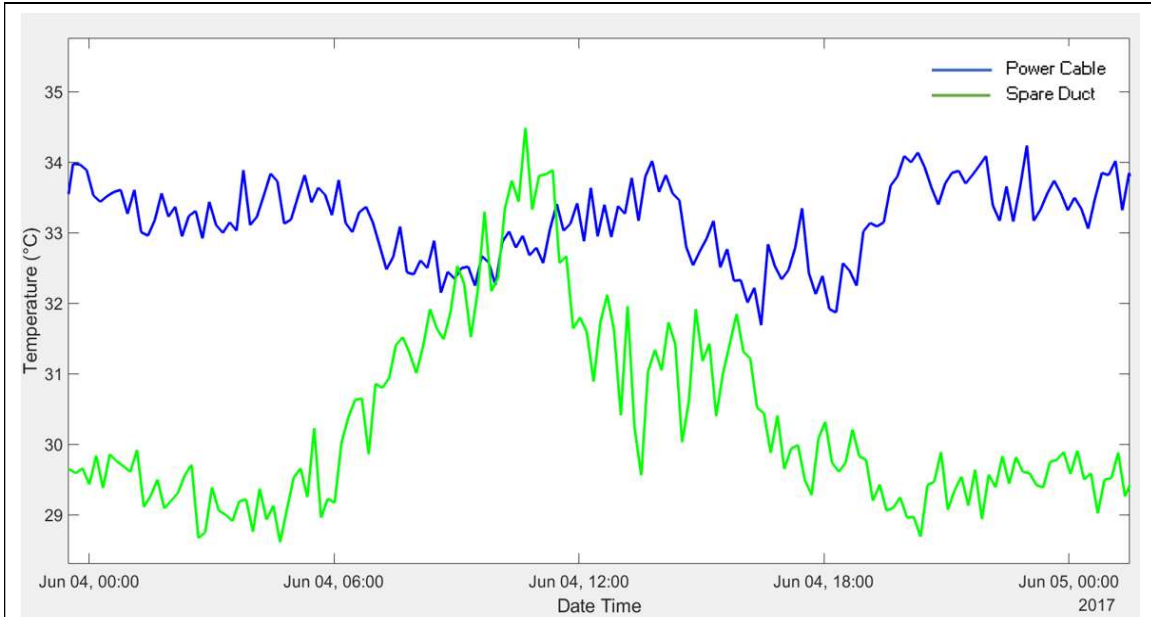


a. Measured temperature for the spare duct and power cable for March 08, 2017

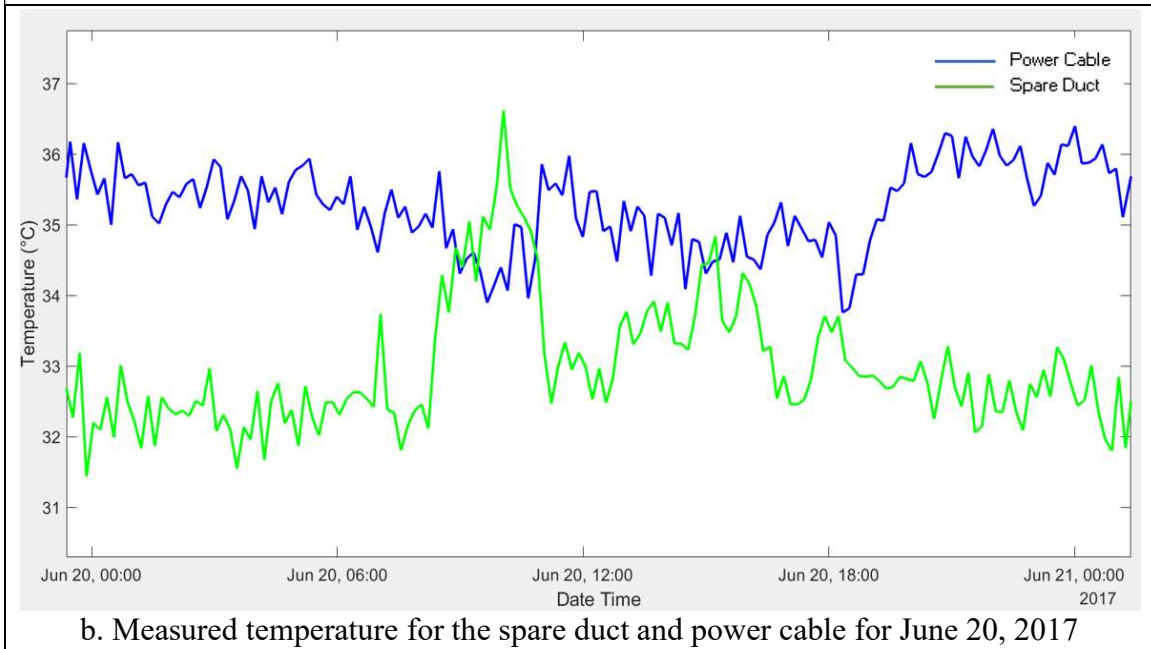


b. Measured temperature for the spare duct and power cable for March 10, 2017

Figure 6-38 Plots for measured temperature in the power cable and the spare duct for March 08 and March 10, 2017



a. Measured temperature for the spare duct and power cable for June 04, 2017



b. Measured temperature for the spare duct and power cable for June 20, 2017

Figure 6-39 Plots for measured temperature in the power cable and the spare duct for June 04 and June 20, 2017

Table 6-7 compares the temperature results obtained from the MATLAB simulation with the measured data for both the power cable and spare duct for both the cases, that is, for Case A and Case B. The values compared include the maximum and minimum temperature

along with the phase shifts of the peaks of the (vaguely sinusoidal) power cable and spare duct temperatures and are shown in Table 6-7 - Table 6-9. These phase shifts are calculated with respect to the peak load in the conductor. Phase shifts were calculated based on (6-1).

Table 6-7 Comparison of temperatures of power cable for measured and simulated data

Date	Maximum temperature in simulation results (°C)	Minimum temperature in simulation results (°C)	Maximum temperature in measured data (°C)	Minimum temperature in measured data (°C)	Error between maximum temperature in simulation result vs. measured data (°C)
<u>Case A</u>					
March 08	31.5	15.4	26.5	22.3	5.0
March 10	32.5	16.8	27.9	24.1	4.6
June 04	44.2	33.7	46.1	43.2	-1.9
June 20	50.9	35.4	49.7	46.2	1.2
<u>Case B</u>					
March 08	21.4	17.8	26.4	24.8	-5.0
March 10	22.3	18.1	27.4	25.2	-5.1
June 04	32.7	29.7	33.9	32.0	-1.2
June 20	40.0	35.8	36.4	33.6	3.6

Table 6-8 Comparison of the spare duct temperatures for measured and simulated data

Date	Maximum temperature in simulation results (°C)	Minimum temperature in simulation results (°C)	Maximum temperature in measured data (°C)	Minimum temperature in measured data (°C)	Error between maximum temperature in simulation result vs. measured data (°C)
Case A					
March 08	25.1	14.1	31.8	23.2	-6.7
March 10	30.8	15.4	32.2	24.6	-1.4
June 04	38.5	28.6	45.0	38.5	-6.5
June 20	41.8	26.5	48.8	43.5	-7.0
Case B					
March 08	22.3	16.5	34.3	26	-12
March 10	23.3	16.7	33.4	26.4	-10.1
June 04	31.9	25.2	34.6	29.0	-2.7
June 20	35.7	29.1	36.4	31.6	-0.7

Table 6-9 Comparison of the phase shifts of the power cable and spare duct for the measured and simulated data

Date		Phase shift in simulation results (°)	Phase shift in measured data (°)
Case A			
March 08, 2017	Power cable	-8.75	75
	Spare Duct	-11.25	-11.25
March 10, 2017	Power cable	-12.5	-7.5
	Spare Duct	-15	-33.75
June 04, 2017	Power cable	-60	No peaks observed
	Spare Duct	-71.25	-75
June 20, 2017	Power cable	-9.5	No peaks observed
	Spare Duct	-9.5	-67.5
Case B			
March 08, 2017	Power cable	-8.5	7.5
	Spare Duct	-11.25	-7.5
March 10, 2017	Power cable	-2.5	-15
	Spare Duct	-15	-33.75
June 04, 2017	Power cable	-3.75	No peaks observed
	Spare Duct	-71.25	-86.25
June 20, 2017	Power cable	10	No peaks observed
	Spare Duct	-45	-67.5

It was observed that the maximum power cable temperatures from the simulation showed a little deviation (5 °C) when compared to the maximum power cable temperatures from the measured data for Case A. However, the minimum power cable temperatures in the simulation were smaller than those in the measured data. This was interesting because, although the increase in the earth's surface temperature was influencing the power cable temperatures, the power cable was not cooling down as fast as the earth's surface or the spare duct after the sunset.

The spare duct for the Case A was at the same depth as the power cable main duct. Therefore, the influence of the earth's surface temperature on the main and spare duct was equal in this case. The other heat source increasing the temperature in the spare duct was the power cable in the main duct itself, therefore it was reasonable to expect that the spare duct temperatures would be lower than those of the power cable for the Case A and that was observed in the simulation results. However, the measured spare duct data showed that the spare duct was hotter than the main duct during the winter months (winter data not shown) and spring months (Figure 6-38) and almost heating up to an equal temperature as the power cable during the summer season (Figure 6-39).

For the Case B, where the spare duct was above the main power cable duct, the spare duct temperatures were expected to be higher than the power cable temperatures for some part of the day as the spare duct is closer to the earth's surface. This was seen in the simulation results in Figure 6-36 - Figure 6-37 and in the measured data in Figure 6-38 - Figure 6-39. However, there is a significant difference in the measured temperature data and the temperature results from the simulation for both the power cable and the spare duct. Recall

that T_{lower} and d , discussed in section 6.2.4 were calculated through iteration based on the summer hotspot location. Since, Case B represents a much deeper duct bank configuration of this installation, the value of T_{lower} and d , were not ideal for this case, which may explain these deviations.

When the phase shifts were compared for the simulation results and measured data, it was observed that the power-cable temperatures generally peaked at a different time of the day during the winter season depending on the peak load current; and during the summer, the power cable temperatures remained almost constant as evidenced by entries in Table 6-9 marked as 'No peak observed'. The spare duct temperatures in the simulation were more influenced by the variation in the earth's surface temperature than by heating from the power cable. However, in the measured data, it was found that the spare duct temperatures peaked before the peak in the conductor load or the peak in the earth's surface temperature, which seems unlikely. It should also be noted that these peaks in the power cable temperatures and the spare cable temperatures are only an estimated value based on the temperature measurements. It is difficult to exactly pinpoint the time for the peak temperatures since the measured data has a low signal to noise ratio. The estimated values of the time for the peak temperature are approximations based on the plots of the measured data. It was also observed (from Figure 6-34), that the spare duct temperatures dropped suddenly sometime close to both 11:30 AM and 2:30 PM. This was odd as there was nothing at the installation to explain this temperature drop in the spare duct.

It was also observed, from Figure 6-34 and Figure 6-38, that the measured power cable temperatures show very little diurnal variation. The measured temperatures in the power

cable were almost constant for any given day. Furthermore, the spare duct temperatures seem to be respond more quickly to the earth's surface temperature when the earth's surface is heating up in the morning than when the earth's surface temperature is cooling down at night.

7 CONCLUSION AND FUTURE WORK

7.1 Hotspot Location

The assumption that the hotspot location occurs at the deepest point of burial in an underground installation is only true when the duct banks are not close to the earth's surface and for an installation with a uniform soil thermal resistivity and uniform duct bank configuration. For installations closer to the earth's surface, the hotspot location is also influenced by the earth's surface temperature. For the Brandow-Pickrell installation, we have two predominant hotspot locations. The hotspot moves from the deeper section of the installation during the winter season to the shallower section of the installation in summer season. Our DTS measurements showed that these hotspot locations can be predicted using the spare duct hotspot location.

These hotspot locations were determined by analyzing the power cable and spare duct measured temperatures for the underground section of the installation. However, if we also include the section of the power cable along the riser poles in our hotspot analysis, we can see that most of the hotspots lie on the riser poles. Figure 7-1 is a histogram of the hotspot locations for the months from February-June 2017. Recall from Table 4-1 that the total scaled length of the Nexans fiber from the splicing joint on P24 to the splicing joint on P30 is 455 m and the sum of the lengths of the Corning cable along the riser poles is 65 m. This makes the total length of the fiber from the DTS to the splicing joint on P30 to be 520 m

(1706 ft.). As can be seen from the Figure 7-1, more than 20% of the hotspots lie close to 515 m (1691 ft.) from the DTS, that is, on the riser pole P30.

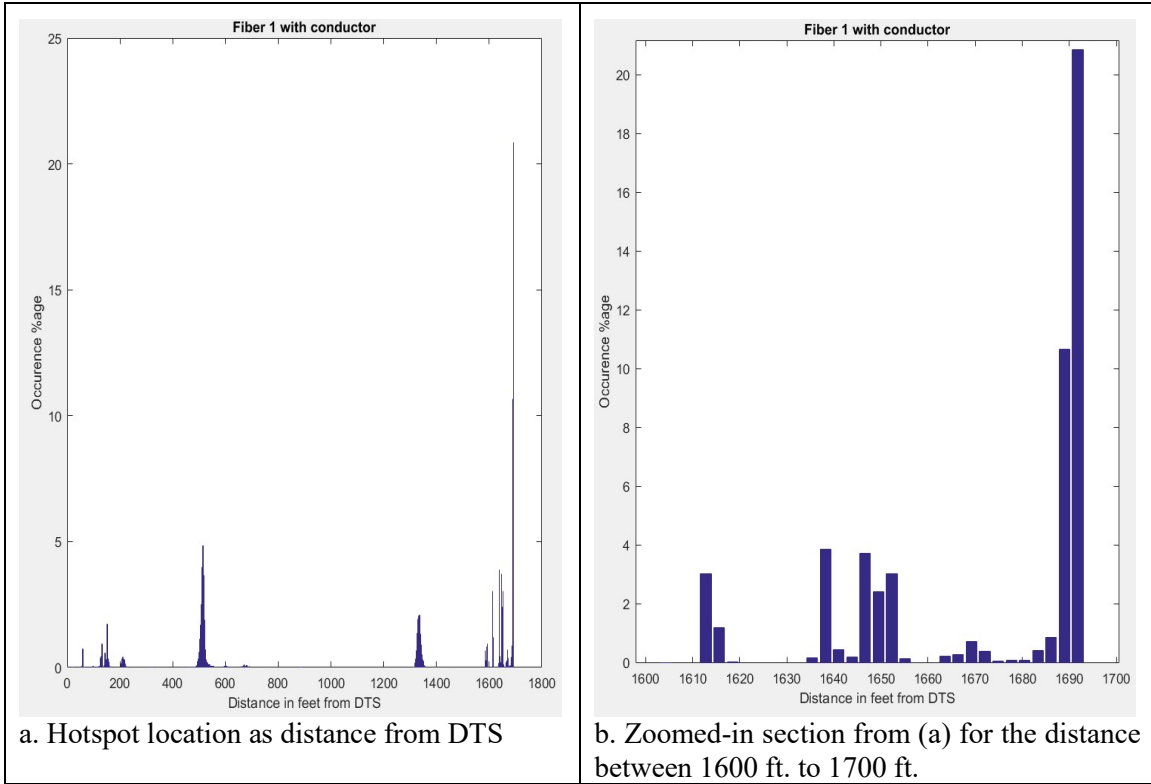


Figure 7-1 Plot for hotspot location in the power cable for the months of Feb - June 2017

The hotspot occurs on the riser poles because the power cable is enclosed in a metallic enclosure on the riser poles which gets very hot during the day in the summer which in turn heats up the power cable. Hotspots on the riser poles can be somewhat mitigated by taking the cable drop on the east side of the riser poles so that it is shaded during the hotter part of the day or by using a perforated encasing to allow better heat dissipation from the power cable.

7.2 Earth's ambient and surface temperatures

The earth's ambient temperature is the temperature of the earth without any underground heat sources. This is one of the most key factors that influence the temperature of the power cable and spare duct. Even software like CYMCAP rely heavily on the earth's ambient temperature to determine the temperature and ampacity of the power cables. Models developed in [7] and [9] also consider the earth's ambient temperature while determining the temperature at any point close to the power cable.

The earth's ambient temperature varies depending on the underground water levels and various other factors. Due to urban development, the underlying drains, water lines, and telecommunication lines make it difficult to model the earth's ambient temperature as one space-independent constant. When using applications with a limited modeling capability, as we had here, the earth's ambient temperature is modeled as uniform and must be estimated.

The earth's surface temperature is the temperature of the earth's surface above the installation. This can influence the power cable and spare duct temperatures if the installation is at a shallow depth. The earth's surface temperature can vary significantly based on the location of an underground installation, for example the installation can lie under a water canal or a bare ground or (as was the case with the installation studied here) under a road section which gets extremely hot during the summer.

The difference between the earth's ambient temperature and the earth's surface temperature affects the rate of heat flow into the earth and can influence the temperature at any point

below the earth's surface and above the depth at which the earth's temperature becomes (approximately) constant year-round.

7.3 Spare duct temperatures

It was assumed at the start of this project that the spare duct temperatures depended solely on the power cable temperatures and therefore a model could be developed to determine the power cable temperatures from the spare duct temperatures. However, it was found that the spare duct temperatures did not solely depend on the power cable temperatures.

Although we were not able to determine the exact causes of the temperature variations in the spare duct. It was observed that the rise and fall of the spare duct temperatures closely followed the sunrise and sunset schedule on bright sunny days and not so much on a cloudy day. This led us to believe that the measured spare duct temperatures were somehow being affected by the solar radiation or the earth's surface heating due to the solar radiation.

The observations led us to believe that there are other external factors which were influencing the temperatures in the spare duct and the power cable. It is important to remember that this installation lies under a road. Therefore, the external factors range from the traffic density above the installation to the underlying drains and water pipes below the installation. Even cloud cover over the installation, for a few hours, can affect the temperature of the spare duct. To model the spare duct and the power cable temperatures more accurately, the external factors should be constantly monitored.

7.4 Future Work

To begin with, to help improve the model accuracy, it will be useful to test the models for the underground installations which are under the bare ground and which do not have any other underlying installations close to the power cables. This can help in determining the effects of many external factors influencing the temperatures in the underground installation.

Further to improve the accuracy of the model developed, the earth's surface temperatures should be constantly monitored for a considerable period of time, as this can help in determining the effect of the earth's surface heating on the temperatures of the underground installations. A study should also be conducted to determine the earth's ambient temperature.

Other techniques, like artificial neural networks and/or machine learning can be used to develop a model to determine the power cable temperatures in an installation only if external factors are continuously monitored for their thermal behavior.

REFERENCES

- [1] Nexans, “60-500 kV High Voltage Underground Power Cables XLPE insulated cables,” New York, Springer, 2003.
- [2] Lios Technology, <http://www.lios-tech.com/Menu/Technology/>
- [3] N.V.D. Giesen, S. C. Steele-Dunne, J. Jansen, O. Hoes, M. B. Hausner, S. Tyler and J. Selker, “Double-Ended Calibration of Fiber-Optic Raman Spectra Distributed Temperature Sensing Data,” *Sensors* 2012, Vol.12, pp. 5471-5485; doi:10.3390/s120505471.
- [4] N.V.D. Giesen, S. C. Steele-Dunne, J. Jansen, O. Hoes, M. B. Hausner, S. Tyler and J. Selker, “Calibrating Single-Ended Fiber-Optic Raman Spectra Distributed Temperature Sensing Data,” *Sensors* 2011, Vol.11(11), pp. 10859-10879; doi: 10.3390/s111110859
- [5] T. Stowers, “Cable Thermal Performance: Assessment of 69kV underground cable thermal rating using distributed temperature sensing”, ASU Digital Repository, 2015.
- [6] Wikipedia, “Thermal Conduction”, https://en.wikipedia.org/wiki/Thermal_conduction.
- [7] J. H. Neher, “The Temperature Rise of Buried Cables and Pipes”, *AIEE Transactions*, Vol. 68, pp. 09-21, 1949.
- [8] G. J. Anders, “Rating of electric power cables: ampacity computations for transmission, distribution, and industrial application”, New York: IEEE Press Power Engineering Series, 1997.
- [9] M. D.Aguilo, F. D. Leon, S. Jazebi and M. Terracciano, “Ladder-type soil model for Dynamic Thermal Rating of Underground Power Cables,” *IEEE Power and Energy Technology Systems Journal*, Vol.1, pp. 21-30, 2014.
- [10] J. H. Neher, and M. H. McGrath, “The calculation of the temperature rise and load capability of cables systems,” *AIEE Transactions*, Vol. 76, part 3, pp. 752-772, 1957.
- [11] L. A. Goldstone and C. Stone, “Temperature-depth profiles with-location information, and tabulated temperatures for Arizona wells measured between May 1979 and March 1982,” *Arizona Geological Survey Open-File Report 82-7*, June 1982.
- [12] National Institute of Standards and technology, “Material Properties,” <http://www.cryogenics.nist.gov/MPropsMAY/material%20properties.htm>.

- [13] R.A. Matula "Electrical resistivity of copper, gold, palladium, and silver". Journal of Physical and Chemical Reference Data, 1979. Vol.8 (4): 1147. doi:10.1063/1.555614